12-10-2010

Flow Control Application on a Submerged Inlet Characterized by Three-Component LDV

Tina H. Reynolds

Flow Control Application in a Submerged Inlet Characterized by Three-Component LDV

DISSERTATION

Tina Reynolds,

AFIT/DS/ENY/10-D03

DEPARTMENT OF THE AIR FORCE
AIR UNIVERSITY

AIR FORCE INSTITUTE OF TECHNOLOGY

Wright-Patterson Air Force Base, Ohio

The views expressed in this thesis are those of the author and do not reflect the official policy or position of the United States Air Force, Department of Defense, or the United States Government.

AFIT/DS/ENY/10-D03

Flow Control Application in a Submerged Inlet Characterized by Three-Component LDV

DISSERTATION

Presented to the Faculty

Graduate School of Engineering and Management

Air Force Institute of Technology

Air University

Air Education and Training Command

In Partial Fulfillment of the Requirements for the

Degree of Doctor of Philosophy in Aeronautical Engineering

Tina Reynolds, B.S.A.E, B.S.M.E, M.S.M.A.E

December 2010

AFIT/DS/ENY/10-D03

Flow Control Application in a Submerged Inlet Characterized by Three-Component LDV

Tina Reynolds, B.S.A.E, B.S.M.E, M.S.M.A.E

Approved:

/signed/	November 22, 2010
Mark F. Reeder (Chairman)	date
/signed/	November 22, 2010
Paul I. King (Member)	date
/signed/	November 22, 2010
Glen P. Perram (Member)	date

Accepted:

M. U. Thomas Date
Dean, Graduate School of Engineering and Management

Abstract

A submerged inlet investigation, using flow control in the form of discrete blowing, examined proximity and jet directionality to improve compressor face uniformity. The flow control locations were at the head of the ramp and part way down the ramp, providing four configurations under examination. Laser Doppler velocimetry (LDV) measurements at the throat determined the effect of the flow control based on the statistical velocity measurements. Blowing at closer proximity to the throat and targeting the largest velocity deficit region provided the best results. The airspeed and inlet velocity simulated takeoff and landing conditions; velocities ranged from Mach 0.1-0.3 at the throat. Secondary components and turbulence measurements proved useful in determining the effect of the flow control configurations. In a complimentary study, two serpentine ducts of rectangular cross-section evaluated the LDV capability before the inlet examination. The s-shaped serpentine ducts had features comparable to those expected in the submerged inlet. The flow through two serpentine ducts, of identical hydraulic diameters but different aspect ratios, demonstrated different behaviors despite all other features being the same. Two strong counter-rotating streamwise vortices formed for the 2:1 aspect ratio while four weaker vortices formed in the 1:2 aspect ratio duct. Computational simulations, performed on the serpentine ducts using a Reynolds shear stress model on a 4 million cell grid, agreed with the results of the experimental examination. The agreement between the exit profiles provided confidence in the LDV system to make the inlet measurements possible.

Acknowledgements

I would like to thank my advisor and committee members for their invaluable feedback and guidance in getting to this point in addition to their patience. They challenged me to think critically of what the results meant and how they could be presented. You brought out the best in my work for expecting it and knowing that I was capable of it. The advice and opportunity provided to learn from my sponsor Angie Scribben on this project was a wonderful experience. Having access to an experienced designer in this field taught me more about the real life concerns relevant to engines. The aid of John Hixenbaugh and Dwight Gehring among others in the laboratory is greatly appreciated. Your patience, aid and concern with the tests was touching and makes you a great asset to the students in accomplishing our studies. Thanks should also be given to AFOSR for support of the project, as well as DAGSI for financial support of the project and my schooling. AFRL/RBAI also provided support to allow me to finish my degree with the opportunity to work with so many intelligent minds. And to my friends and family thank you for your support in seeing me through all of this. Thank you everyone and many blessings to all of you.

Tina Reynolds

Table of Contents

Page

List of Figures

List of Tables

List of Symbols

Symbol		Page
De	Dean's number	13
D_h	hydraulic diameter (mm)	13
R	Radius of Curvature (mm)	13
Re	Reynolds number	13
u'u'	Turbulent Reynolds stresses (m^2/s^2)	26
v'v'	Turbulent Reynolds stresses (m^2/s^2)	26
w'w'	Turbulent Reynolds stresses (m^2/s^2)	26
u'v'	Turbulent Reynolds stresses (m^2/s^2)	26
u'w'	Turbulent Reynolds stresses (m^2/s^2)	26
v'w'	Turbulent Reynolds stresses (m^2/s^2)	26
y^+	Non-dimensional boundary layer thickness	31
U/U_s	Velocity distribution of the jet over the reference velocity	38
U_{av}/u_∞	Inlet to free stream velocity characterization	40
m_r	Mass flow ratio of the jet to the inlet	40
u	Velocity component (m/s)	42
v	Velocity component (m/s)	42
w	Velocity component (m/s)	42
u_{avt}	Volumetric flow rate over the area (m/s)	56
w'	Root mean square of the velocity (m/s)	64
u'	Root mean square of the velocity(m/s)	64
v'	Root mean square of the velocity (m/s)	64
y^+	Viscous sublayer, non-dimensional distance from the wall to the transition of the outer flow region	81
U_{av}	Average throat velocity (m/s)	105

List of Abbreviations

Abbreviation		Page
AIP	Aerodynamic Interface Plane	3
UAV	unmanned aerial vehicle	4
ZMF	Zero Mass Flux	4
ZNMF	Zero-Net Mass Flux	4
RECITE	Reactive Conformal Inlet Technology Enhancement	4
AFRL	Air Force Research Laboratories	5
NACA	National Advisory Committee for Aeronautics	5
LDV	Laser Doppler Velocimetry	5
CFD	Computational Fluid Dynamics	6
RSM	Reynolds Stress Model	14
AGARD	Advisory Group for Aerospace Research and Development	17
SLPM	Standard Liter Per Minute	21
CAD	Computer Aided Design	29
AFIT	Air Force Institute of Technology	44
ISSI	Innovative Scientific Solutions Incorporated	44
RMS	Root Mean Square	77

Flow Control Application in a Submerged Inlet Characterized by Three-Component LDV

I. Introduction

As in many things, how something begins sets the stage for everything to follow. This is true for engine inlets. The pressure recovery of the free stream at the compressor dictates the efficiency and performance of the engine, therefore, the inlet efficiency affects the entire performance of the engine.[4],[5],[6] Poorly conditioned flow to the engine yields decreased performance or leads to catastrophic failure.[4] For these reasons, along with improved efficiency and cost savings, improvements in the engine inlet's performance are sought.

Over thirty years ago, measurements and guidelines for the flow quality into the compressor were standardized for assessment of enhancements or detriments made to inlet performance. After deliberation by a selected panel of experts, a universal standard established in the ARP 1420 and AIR 1419 documents became the pressure uniformity guidelines.[7],[8] These guidelines focus upon the pressure uniformity of the inlet through measuring the distortion of the entering flow and quantifying the pressure recovery. A vital factor in inlet performance is the pressure distortion.[7] A few percent improvement in the uniformity of the pressure face recovery yields improvement in the engine performance. The compressor works less to obtain the desired flow through the engine.[9] Limiting non-uniformity of the total pressure profile at the compressor face prevents fatigue loading of the blades as they rotate.[5] Pressure recovery directly affects the thrust and stability of the compressor.[4] The stability of the compressor is a concern in the wide range of operation the engine experiences throughout its operation since an inlet design impacts the quality of the flow.[4] For curved inlet shapes, longer inlets lead to more uniform flow. Competing with the

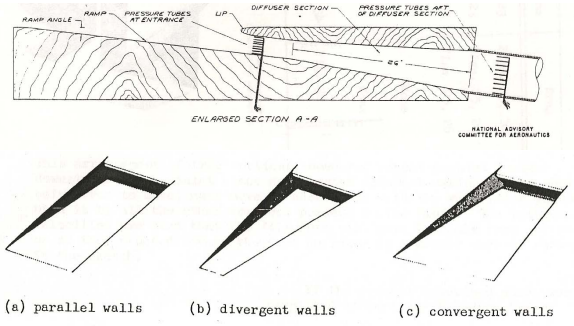

Figure 1. Submerged inlet profile, (top) a side view of the ramp and duct geometry, from Mossman and Randall[1] (bottom) the entrance shape leading into the body, from Sacks and Spreiter[2]

desire to maintain low engine weight provides a complicated balance to achieve an optimal design.

The submerged inlet design investigation began in the 1940's in hopes of providing better efficiency through reduced form drag. The form drag reduction created by streamlining the engine inlet within the fuselage potentially increased the overall efficiency.[6] The pressure losses experienced by the flow curvature into the fuselage diminished the benefits achieved from the form drag reduction.[6] The submerged inlet's integration hides the engine signature while reducing the axial distance to the compressor, as shown in Figure 1. The flow turning occurs multiple times before it enters the compressor in a submerged inlet, similar to s-shaped ducts. Figure 1 excludes the forebody section providing the initial turning of the flow into the fuselage. Clearly shown in Figure 1 is the recessed inlet. There is no clear established path for electromagnetic waves which significantly reduces the compressor signature. This type of inlet potentially reduces structural support weight. The fuselage protects the engine, inhibiting possible foreign object ingestion. The shorter spatial distance to the compressor face, relative to the inlet entrance, allows the engine system to be smaller and lighter. A smaller and lighter frame liberates engine capability for payload or thrust usage. Despite the benefits, submerged inlets face difficulties in practical implementation due to the flow curvature leading into the compressor.

Flow curvature in a submerged inlet creates pressure distortion at the interface to the compressor due to losses.[10],[11],[12],[13],[14],[15] The pressure losses and deficits incur from boundary layer growth and flow separation in the inlet. The curvature plays a role in the losses by shifting the high velocity core flow and generating secondary velocities.[10],[13],[12],[16],[17] This leads to significant variations in velocity and pressure creating fluctuating stresses on the compressor blades. Researchers categorized these pressure variations as the distortion or pressure distortion. The flow is not uniform across the entire engine face nor across the aerodynamic interface plane AIP. Distortion of the pressure face decreases the compressor's stability margin and increases fatigue on the blades.[5] Distortion is a concern for all inlets, but a straight entrance typically experiences less complicated flow features since it lacks the flow turning of submerged and scoop inlets.

The imperative to provide a low observability of the compressor is an additional consideration to the design of the inlet to increase survivability for military aircraft. Aggressive turning of the inlet allows the engine to be completely hidden and further reduces the engine's overall length in the aircraft. The submerged inlet is one of the possible designs to obtain the objective of low observability.

Flow quality improvement through flow control is necessary for submerged inlets to be a practical option. This investigation geared toward improving the pressure recovery and uniformity of a submerged inlet using active flow. Prior examinations of the flow within a submerged inlet lent insight into the problem of pressure losses and how the distortion can be limited. Literature suggests that submerged inlets are only an option without flow control at low Mach, $M<0.6$, due to the high losses in pressure recovery with compressibility effects.[13] Some understanding of the dynamics of the flow within the inlet can be gained by considering curved ducts since part of the flow in submerged inlets behaves as a serpentine duct. Boundary layer growth occurs and separation is possible, particularly during aircraft maneuvers. At higher Mach numbers the curvature over the forebody and into the ramp initiates shock losses. Ideal theory provides an upper limit for the pressure recovery possible after a shock.[18]

Even at subsonic speeds the curvature into the submerged inlet creates losses due to separation.[19],[20]

Unmanned aerial vehicles (UAV) are a case where submerged inlets provide a potential practical solution. The flight regime of UAV's remain within the subsonic range. Losses due to the boundary layer exist, but are minimal in comparison and less detrimental to engine performance. The submerged inlet flew in two functional high speed aircraft. The YF-93 and SB4 Sherpa implemented, designed and manufactured submerged inlets.[21] The YF-93 flew at transonic speeds while the Short Sherpa was a subsonic plane. Neither design proved to be the best solution; the scoop and nacelle designs provided better overall performance.[21] Even in the subsonic flight regime, curvature and boundary layer growth discouraged use of submerged inlets without flow control. The pressure losses created by the boundary layer and flow separation on the ramp produce pressure losses along the ramp of the inlet and in the corner region where the ramp and sidewalls meet.[1]

The elimination of this boundary layer induced pressure deficit through flow control is a primary focus of this study. Previous work in the literature demonstrates improvement in the pressure recovery at the AIP uniformity obtained by attenuating or lessening this sluggish region of flow.[3],[19],[20] Blowing is effective in energizing the boundary layer without some of the inherent costs and difficulties of suction or zero mass flux (ZMF) or zero-net mass flux (ZNMF) devices.[22],[23],[24] The curvature of submerged inlets is typically gradual to prevent separation losses; even so, losses are still greater than those experienced by short straight inlet systems.[9]

Pursuance of this design followed the results of RECITE program.[25] For RECITE, a slot positioned upstream of the throat to counter the effects of the boundary layer losses served as the flow control system for a submerged inlet examination. The percentage of blowing required for pressure uniformity was approximately 7.5% of the flow through the throat.[25] This value exceeded practical limits, the engine has bleed already taken for cooling, and loss of high pressure flow reduces the thrust of the

engine. The reduction in thrust is the reason for high pressure bleed minimization.[4] Reduction of the percentage of mass addition for the flow control required, makes aggressively curved submerged and serpentine inlets viable, rather than remaining an academic possibility. In some serpentine duct studies blowing was effective with only a 2-3% percent mass addition to the inlet flow.[17] Many other studies predominately focus on passive methods of altering the flow into the inlet, investigating an active flow control method expands the available knowledge. The decision to try an active flow control method came from the fact that active flow methods typically receive less examination and the desire to improve on the results of the RECITE project conducted at AFRL. The NACA inlet design obtained from AFRL/RBAI provided the basis for investigation of a generic submerged inlet.

Discrete holes replaced the slot configuration, increasing the exit velocity for a given percent addition. Circular hole profiles are the easiest to manufacture, and the growth and breakdown of circular jets are well documented. The location of the mass injection relative to the throat was examined in addition to adding a spanwise component. Close coordination with AFRL/RBAI ensured that the present study's results had relevance to the RECITE and following program. The multiple port configurations permitted future consideration of operating specific ports for maneuvering effects. In this investigation, all ports operated to determine the effectiveness with the orientation and placement criterion. The information gained, was also beneficial for potential validation of CFD studies of the submerged inlet.

Total pressure probes, commonly used for testing inlet designs, are intrusive and normally yield information on only the streamwise component of the flow. Measurements indicate only the streamwise velocity changes, rather than the secondary flow. The alteration of the flow field's characteristics with the addition of flow control made it desirable to capture a finer grid resolution of the inlet throat than easily obtainable with Pitot probes. The measurement technique that suited these requirements was laser Doppler velocimetry (LDV), which is non-intrusive. Three-component LDV led to measurements of the streamwise velocity, secondary flow field, and turbulence

statistics for each condition. Measurement of the secondary velocities elucidated the differences in the flow control methods. The size of the model made measurements with pressure probes limiting. Probe size prohibited the number of probes and created blockage of the throat. The measurement locations fell short of the desired 40 Pitot probes.

Two serpentine ducts examined prior to experimentation with the LDV in the submerged inlet provided assurance of measurement capabilities. The serpentine ducts were a controlled environment that allowed assessment of the LDV's capability to capture the secondary flows. First hand examination of the velocities from flow curvature in the serpentine duct provided basic expectations for the submerged inlet. Two serpentine duct designs with different aspect ratios demonstrated the geometry changes' effect on the strength of the secondary flows and possible behavior for the submerged inlet. In conjunction with the serpentine duct experiment, numerical simulations were performed. The computational results provided validation of the streamwise velocity distribution and the secondary flow behavior in the experiment. The computational fluid dynamics (CFD) results also permitted further examination of the flow features creating the exit pattern. Validation of the LDV system allowed characterization of the submerged with and without flow control. This investigation included measurements of the secondary flow structures upon the flow evolution into the submerged inlet and how altering the secondary flow related to the uniformity and pressure losses.

II. Background

2.1 Some History of the Submerged Inlet

Submerged inlets first came under consideration in the late 1940's and early 1950's. Examination of the performance of submerged inlets and scoop inlets determined the best inlet from the perspective of engine efficiency and is reviewed in Sobester's work.[6] In the subsonic regime the submerged inlets compared favorably to a scoop inlet; the advantages of the scoop became evident in the transonic region. Scoop inlets experienced less pressure losses from the shocks.[6],[18] Studies on improvement of the submerged inlet's performance were conducted, but only passive methods were used. Altering the shape of the inlet, specifically the ramp angle, gave the predicted solution of improving the pressure uniformity due to the milder turning of the flow, as defined by the ramp angle in Figure 1(a).[1] Ramp divergence was examined by Martin and Holzhauser to ensure results were applicable to the scale and operating conditions of interest.[26]

The inlet shape studies determined the controlling factor in increasing the pressure recovery. At incompressible speeds the boundary layer is the most significant contributor to the pressure losses in the inlet.[1],[19] The other factor that contributed heavily to the losses was the vortex roll up at the sidewalls.[2],[3] This roll up vortex, as illustrated in Figure 2, thickened the boundary layer along the walls, particularly at the corner where the ramp and wall meet. By changing the wall angle and rounding the edge, the vortex decreased the boundary layer thickness using the vortex to introduce momentum to the ramp and corner, as shown in Figure 2.[3] These studies demonstrate the impact of the boundary layer and vortex roll up on the pressure recovery.

In transonic flow, the shock losses created a stumbling block towards increased efficiency and recovery in addition to the boundary layer losses.[19],[20] The turning of the flow to enter the inlet due to the ramp and forebody accelerates and expands some regions of the flow generating a shock.[18],[27] The boundary layer thickens because of the pressure gradient after the shock, contributing to the boundary layer pressure

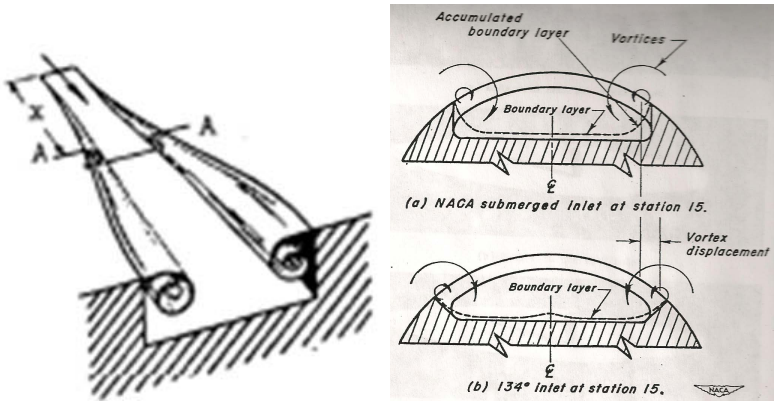

Figure 2. Formation of the vortex over the inlet walls(left).[2] The effect the wall angle has upon the vortex strength (right).[3]

losses.[12],[13],[18],[28] Most flow control applications occur at the shock or shortly after. Any flow control used at subsonic and transonic speeds is still effective on the boundary layer growth along the ramp.

After this initial interest, focus shifted away from submerged inlets as a preferred arrangement for aircraft. Submerged inlets were relegated to engines requiring less high quality flows or became auxiliary intakes.[21] Examples of engines that accept lower quality flow are those of missiles or air-breathing rocket design.[29],[30],[31],[32],[33],[34] Cruise missiles are a common application of a submerged inlet providing propulsion.[29],[34] The flow quality is of lesser concern, but the quantity of air, or more specifically oxygen available for combustion is of importance. Separated flow within the inlet inhibits the mass flow through the engine and greater during maneuvers. The distortion levels for air-breathing rockets are less of a concern; no mechanical parts interact with the flow. These engines used submerged inlets to lower the form drag to maintain high thrust.

Many designs utilizing passive flow control incorporated the flow control near the compressor face to enhance the pressure profile.[6],[3] External shaping of the inlet became deemphasized in comparison to controlling the interior flow, even though the external flow development leading to the entrance flow was important. The entrance flow design prevented significant velocity and pressure deficits that translated into

the duct portion. The previous NACA studies in the 1940's and 1950's examined the shaping of the ramp angle and the inlet. More recently, the focus shifted to consideration of the inlet duct leading to the compressor face. In one example of passive flow control, vortex generators added to auxiliary inlets improved the low speed performance.[35] The vortex generators thinned the corner boundary layer flow.[35] The auxiliary inlets were submerged inlets with the flow undergoing possible separation and poor pressure recovery.

The resurgence of interest in submerged inlets for aircraft was largely due to the necessity of decreasing the compressor face observability and increasing the survivability of the aircraft.[36] The curvature and duct profile for a submerged inlet partially to completely obscures the compressor face profile. The hidden profile prevents reflection of radar from the compressor blades and reduces the aircraft's susceptibility.[36] Computer simulations in recent years aided in ascertaining methods to improve the inlet uniformity and pressure recovery.[37] Experimental examinations ensure that the numerical simulations accurately predict the flow behavior. The two methods of flow examination are linked and necessary for advancing improvements in inlet design. Strongly curved surfaces present some difficulties with the commonly used turbulence model, dealing with assumptions in the isotropy of the Reynolds stresses due to asymmetry in the flow field created by the pressure gradient.[11],[16],[38],[39],[40],[41]

As in the early experiments, many of the more recent studies focus primarily on passive methods of altering the inlet uniformity. Passive flow control methods shape the surface interacting with the flow. Passive flow control methods function within a limited range of flow conditions.[4],[5] Cruise conditions dictate the inlet design optimizations since most civil aircraft spend a majority of their flight within this regime.[42] Military aircraft require more versatility. Due to the complexity of the inlet flow, many computational studies examine the flow dynamics of the submerged inlet with the simplification of uniform flow upstream. The boundary layer and separation concerns as well as the vortex formation from the bends were points of interest in these studies.[31],[43],[29],[44],[45]

Implementation of various modeling methods sought to provide the best representation of the flow field with and without passive flow control. Knight et. al[31],[43] as well as Peifen et. al[29] used computational simulations to examine the basic flow field in the submerged inlet. Knight et. al was able to model the flow development with changing conditions and evaluate the pressure and velocity distortion created with the k-ω model and Peifen et. al with the k-ϵ model with RNG functions. Tsay and Chen[44] compared a code developed from Ni's scheme with experimental data to evaluate the modeling capability. Tsay and Chen found very little difference between the 0.3 and 0.6 freestream inlet behavior. Abbot and Slater[45] used the Spalart-Almaras turbulence model on an open-to-the-freestream serpentine inlet entrance design, but focused on examining the boundary layer separation. The ramp angle alteration repeated computationally observed how the angle directly affected the flow in Lee et. al study.[46] The boundary layer and its effect on the inlet profile was the focus of each of these studies mentioned. In the subsonic regime, the boundary layer is the most significant contributor of pressure losses. By necessity this active flow control design directs its effort toward boundary layer control.

Recent studies at Rutgers University utilize both experimental and computational techniques in submerged inlet design. Knight, Taskinoglu, Elliott and Jovanovic performed tests in the subsonic regime. Both computational and experimental methods studied inlet design enhancements. The primary measure of inlet performance is a combination of pressure recovery and uniformity of the pressure profile just before the compressor as evidenced in Knight et. al[31] and in Berrier et. al.[47] Knight et. al[33] and Keller et. al [48] focused on an optimization scheme in numerical simulations for designing inlets of prescribed geometric parameters. A set of criterion established the program guidelines; the program iteratively reshaped the duct according to the restrictions for determining the next modification improving the inlet pressure profile.[30],[33],[32],[49] The shape evolved computationally until an optimal pressure recovery and low pressure distortion level configuration developed from the criterion. Knight and Taskinoglu along with Jovanovic and Elliott added bumps to the duct as

a passive flow control method to affect the boundary layer as well as a fin to create mixing from the tip vortex.[32],[43] The k-ω modeled the inlet flow behavior with a third order MUSCL and Roe's condition applied to help with the near wall region. Computational models are only as good as the turbulence model.[50] Isotropic turbulence models encounter difficulties in modeling for highly curved flows.[40],[51],[41] The difficulty with modeling curved flows is the reason for performing experimental validation. The main flow features normally develop in the isotropic numerical models, though not with great accuracy. Pitot probes and hotfilm techniques validated the experimental correlations at the subsonic speeds against the CFD in Knight et. al studies.[30],[33],[32],[49] The measurements were intrusive and could only yield information about the streamwise direction. The hotfilm and pressure ports yielded good correlation in measurements so that the hotfilm data could be compared to the computational data. The computational model displayed the same types of flow features found with the hotfilm measurements for the fin and duct indentation flow control methods. The relative magnitudes of the velocity in the experiment were similar to the computational results. The criterion for passively improving the inlet performance computationally was deemed a success.

In contrast to the passive flow control methods described above, the number of active flow control studies performed upon the submerged inlet is less pervasive. Active flow control is more commonly implemented on separation with wing surfaces. Both active and passive flow control techniques are more effective at the most receptive region in the flow, typically located just before separation. [52],[23],[24] Some examples of active flow control methods are bleed[6] of the boundary layer flow or blowing to energize the boundary layer.[25] The engine has compressor bleed already used for cooling; removing high pressure flow reduces engine thrust. Bleed reduces engine thrust so low levels of bleed are desirable, a few percent of the core flow at most.[4] If the performance benefit from the flow control improves pressure recovery, the increased engine efficiency could outweigh the loss created by the compressor bleed. The usage of high pressure compressor bleed might become acceptable in al-

tering the pressure profile of the submerged inlet.[25] The compressor bleed flow used for the boundary layer control becomes reintroduced into the core flow. The thermal effects are neglected in this study, the same ambient temperature flows throughout the experiment. Thermal distortion from the bleed is small relative to the size of the compressor entrance and the greater affect of thermal wake ingestion.[8]

Mechanical actuation added to the compressor bleed flow affects the boundary layer in a different manner; the actuation transforms the flow control into pulsed blowing.[53] Mechanical actuation reduced by half, at the least, the amount of mass flow addition required to energize the boundary layer.[52],[22],[54],[55] The mechanical actuation can be as simple as pulsed blowing, as was performed in Hall, Chokani and Heinzen's[52] study; or zero-net mass flux devices as in Cater, Gordon, and Soria's[55] study. The study of these devices for actuating the jet flow is an examination of its own, more commonly found in airfoils.[54],[22] In some cases the actuation requires a third of the mass flow ratio of steady blowing to achieve the same results.[22],[52] Anderson and Keller altered the secondary flow through micro-scale flow effectors in a compact diffuser. This is one instance of active flow control utilization.[48] The micro-effectors produced noticeable attenuation to the flow of interest.[48] The addition of steady blowing into the boundary layer alters the growth behavior, making the flow field more difficult to model.[56]

2.2 Serpentine Ducts

A similar venue of investigation to the submerged inlet is the serpentine duct geometry. Serpentine duct flow fields experienced more implementation of active flow control than submerged inlets. Flow turning in aircraft is a common occurrence in dual intakes.[6] Exposed, rather than submerged, curved inlets are classified as scoop designs. Scoop inlets integrate the engines into the plane and reduce observability more effectively. This is in conjunction with reducing weight for engine supports on the wings. Curved or serpentine ducts also appear in other applications so the flow behavior for some specific geometries have extensive documentation.[11],[57],[10]

The duct geometry and Reynolds number strongly influence the flow development.[11],[14],[39] In order to study curved ducts, many of the earliest curved duct flows were rectangular to accommodate the viewing planes of interest.[58],[59] Curved flow behavior examinations investigated whether the flow generalized with something like a Reynolds number.[16],[60] A parameter defining the flow development in curved ducts was the Dean number. The Deans number, De, relates to the hydraulic diameter, D_h, the radius of curvature at the centerline of the duct, R and the Reynolds number of the flow, Re. One definition of the Dean number is $De = [D_h/(2R))]^{0.5}Re$.[16],[61] The value of the Dean number reflects the momentum exchange and mixing brought about by the strong curvature. A numeric indicator for curved flow is less effective in defining the flow. After a certain point, the behavior becomes undefined and not relatable by the Dean number. Secondary flows categorized by the Dean number were not definitive from the non-dimensionalization. Complexity introduced by a simple geometry change yield different results even with the same value of the Dean number.

Serpentine ducts validate computational models, since curvature effects create complex flow patterns.[40] The modeling of the turbulence affects the numerical solution due to the modeling of the anisotropy of the flow, particularly with high turning angles.[62] The anisotropy of the flow mandates that turbulence models include non-linear effects for better representation.[63],[64],[65],[50] These non-linear effects modified the equations for k-ω and Spalart-Almaras models. The lower computational costs made it desirable to add the modifications in predicting anisotropic effects.[64],[50] The effects of the third order differencing scheme leads towards instabilities generated by the flow turning.[66] The instabilities add complexity to the flow and interact with the boundary layer preferentially.[66]

The introduction of flow control jets further alters the dynamics of the flow, particularly the turbulence statistics.[56] The turbulence within the flow plays a large part in reorganizing the flow behavior. The turbulence redistributes the energy and equalizes imbalances.[14],[38],[39],[67],[68] At one point, the AIR panel of experts questioned whether secondary flows were of relevance towards engine stability.[15],[69],[8]

The guidelines outlined by the committee in the AIR determined the relevance of those secondary flow effects.[8] A phenomena that adds to the complexity of the curved flow analysis with implementation of active flow control is the formation of vortices from the Gortler instability.[70],[71],[72] The instability aids in the persistence of the jets, but prevents mixing of the boundary layer flow. Both turbulent and laminar flows received consideration. The more relevant condition is the turbulent flow, since most aircraft operation exists in this flow regime. The curvature rapidly transitioned the flow towards a turbulent boundary layer.[59] Laminar solutions cannot be entirely discounted as laminar flow could persist for a portion of the duct even in the most dynamic flows.[58]

The application of two bend entrance flows exists in some unmanned aerial vehicles. Flow separation contributes heavily towards a pressure deficits at the compressor interface and presents a problem with the uniformity.[73] Whitelaw and Yu obtained velocity measurements for a specific diffusing serpentine duct. The diffusing nature of the duct contributed to flow separation, besides that produced by the curvature.[59] The separation appeared in the velocity measurements, obtained in the duct, at various locations throughout the curvature. The single component velocity measurements showed that separation occurred after the second bend in the studies by Whitelaw and Yu; Wellborn, Reichert, and Okiishi; and Rabe, Ng and Burdisso.[59],[74],[17] The flow normally developed only a small separation bubble after the first bend. The immediate turning of the flow and the changing pressure dynamics created by the second flow turning prevented full separation.[10],[74] As mentioned previously, separation of the flow made it difficult to predict the flow in a curved duct.[75],[63] The RSM model generally is currently the most reliable, if the most numerically costly option in commercial solvers.[41] Directly calculating the Reynolds stresses requires additional equations.[50],[38] Quick estimates of overall effects are beneficial for some studies using other solvers. Anderson, Reddy and Kapoor determined that forced mixing and viscous dissipation decreased the distortion based on their computational study using the k-ϵ model.[76] Vortex generators created forced mixing on the bound-

ary layer flow in a passive flow control method leading to an increase in the pressure recovery.[76]

2.3 Active Flow Control Examination

Flow control in serpentine ducts generally requires relatively small amounts of flow addition, less than three percent of the mass flow through the system. Both the method of application and placement dictate the effectiveness. Slots, while capable of providing uniform coverage over an expanse, require an undesirably higher mass flow rate than jets to maintain the same exit velocity.[10] Carefully designed multiple jet configurations theoretically achieve the same results at a reduced mass flow rate. The jet growth becomes into play in providing uniform coverage based on the overlap regions. Looking at the behavior of an individual jet assists in determining the growth behavior, while examination of jet interaction is more enlightening.

In order to decrease the boundary layer thickness, the boundary layer in a serpentine duct can either be removed or energized with an outside flow. Florea, Haas, Hardin, Lents and Stucky applied a bleed system to the inlet flow to siphon the boundary layer region from the incoming flow to the engine.[53] Rabe, Ng and Burdisso applied blowing to the boundary layer flow to generate mixing and reduced the momentum deficit in that region.[17] Both studies claimed success in obtaining more uniform pressure profiles with reduced distortion. Bleed of the boundary layer led to a reduction in the distortion intensity by 40% at the AIP.[53] This reduction is significant, as less distortion means a more uniform pressure face. In the study by Rabe, Ng, and Burdisso injected one percent of the core flow into the stagnation region after the second bend. This quantity of active blowing flow control overcomes the separation losses after the second bend. The second bend was the main contributor to the pressure losses at the engine interface.[17] A marked decrease in the circumferential distortion and improvement in the pressure recovery occurred from the addition of two percent mass flow.[17] This is particularly important since the circumferential distortion leads to compressor blade fatigue.[8]

The growth characteristics of shaped jets permit several options in flow control design pertaining to the jet orifice exit. The most extensively studied shape is the circular jet. The jet core's persistence and eventual breakdown received much attention and documentation on its characteristics in stagnant air towards the self-preserving state.[77],[78] These studies gave an indication of the type of behavior expected for individual jets in ideal conditions.

Some other jet nozzle shapes examined were the elliptical shape by Ferdman, Otugen, and Kim[78]; Singh, Sundararajan, and Bhaskaran[77]; Ho and Gutmark [79]; and Wilson, Schadow, Lee and Gutmark [42]. All research groups noted the enhanced core breakdown experienced by this shape compared to the circular nozzle exit. The presence of axis switching redistributed the velocity profile enhancing the jet spreading rate. Singh, Sundararajan, and Bhaskaran [77]; and Quinn[57] investigated rectangular jets. Compared to circular jets, rectangular shapes also increased core breakdown. The core redistribution was dependent on the aspect ratio. Quinn[80] and the diamond shape by Tomiaka, Jacobsen and Schetz [81] documented triangular jet growth. The corners of these shapes created vortices that changed the turbulence levels to generate increased mixing. The mixing of the flow between the core and shear layer was an important factor of this submerged inlet study. Tabbed circular jets received consideration. Tabs in a circular jet enhance the jet core breakdown through creating more mixing of the flow.[82],[83] Tabbed jet configurations detailed in the studies by Bradbury and Khadem[82] as well as the study conducted by Zaman, Reeder, and Samimy[83] displayed increase mixing. The angle of inclination and number of tabs changed the mixing behavior of the jet core with its surroundings.

Single jet mixing theory cannot provide an accurate prediction for the jet interactions for a better indication of the spanwise uniformity in the submerged inlet. This is particularly true with the angled jet flows. The decay of the mean velocity by half for a single jet indicated the mixing behavior and the distance required to span the ramp in theory. Circular jet theory for laminar and turbulent flow provided a calculated estimate of the distance required for the half velocities to overlap.[14]

Situations focused on jet mixing were the basis for deciding the hole design. In our studies, the use of rapid prototyping material made almost any hole configuration possible. One relevant study examined jet shapes in a co-flow with shearing on both sides, performed by Glawe, Samimy, Nejad and Chen[84]. This situation is similar to the jet flow behavior for injection into the boundary layer flow of the submerged inlet. The shearing co-flow led to the jet growth being along the span of the plate's wake.[84] The core breakdown for the various shapes examined for the multiple jets found the dispersion greatest for an elliptical jet oriented with the major axis in the vertical direction.[84] The two tabbed circular jet with the tabs oriented along the vertical axis also performed well in the jet core breakdown, directing the growth of the jet.[84] Consideration for actual manufacturing in this project for future implementation of the jet configuration made circular jets practical. The jets situated in the step configuration implemented in the RECITE project that contained a slot for the flow control.[25] In general the duct leading to the exit shape is circular before the shaped exit.

The breakdown of a jet in a cross-flow is far different due to the shearing of the flow being greater than a co-flow, as documented by Peterson and Plesniak.[85] Jets entering a cross-flow represents the second type of active flow control implemented with the flow control configurations. The angled flow potentially presents problems with lift-off of the jets. Jet lift off inhibits the desired effect on the boundary layer. Film cooling on turbine blades occurs at higher angles than performed in this experiment, normally 35°.[86],[87] Film cooling requires that the cooler injectant remain in the boundary layer to reduce blade heating. An early AGARD review indicates that anything below a 30 degree angle will remain attached to the surface.[88] These studies support the belief that the low entrance angles of the flow control will remain attached to the surface despite the high blowing ratios.

Some other relevant studies of increased mixing added angles to the jet entrance into the main flow. A ramp with a backward facing step for mixing enhancement of the flow used vortices generated from the corners of the discrete ramps in the study

by Hartfield, Hollo, and McDaniel.[89] Most of the flows directed at high inclusion angles into the flow, 20-40°, with the jets angled towards each other, impingement of the jets lent to the deterioration of the cores.[90],[91],[81] The high inclusion angles direct the fuel away from the wall in these studies. The impinging jets were performed for both elliptical[90],[91] and diamond[81] shaped injectors angled anywhere from 3-9° relative to the streamwise direction in the spanwise direction. The elongation of the exit plane formed slightly as a consequence of the exit angle of the duct relative to the surface. The elongated shapes purposefully chosen and enhanced the core breakdown compared to other jet shapes. The single jet studies determined that jets with corners experienced greater mixing as did jets from an elliptical exit.[79],[77] For non-interacting multiple jets, elliptical and non-circular exit shapes performed better. The corners jets at the nozzle exit created vortices enhancing mixing.[42],[92]

Due to the similarity in geometry, the serpentine duct shared some flow dynamics with the submerged inlet.[17],[59] The NACA based model had a diffusing section where the rectangular throat transitioned to a round cross section. Examination of the curved duct aided in understanding the flow behavior in this section of the inlet. The serpentine ducts added familiarization of the growth contributors of the secondary velocity and the capabilities of a five-beam single head probe to capture all three velocity components. The numerical simulation performed on the serpentine duct aided in the evaluation of the abilities of both the LDV and commercial computational code. The computational studies, using the serpentine ducts for code validation, made it clear that the Reynolds stress model would be the best of the available choices. The serpentine duct provided a basis for understanding the secondary flow structure present in the submerged inlet. The prior studies on submerged inlets indicate that the use of blowing for pressure recovery would be enlightening. The choice and number of holes for re-energizing the boundary layer flow came from the growth behavior observed with the angling of the flow control. Angling of the flow to direct mixing towards a desired location and the extent of the angle came from the works stated above.[90],[91]

III. Experimental Setup

The submerged inlet examinations by means intrusive probe techniques were incapable of obtaining a fine resolution of the secondary flow behavior and turbulence quantities. Non-intrusive techniques were unavailable in the previous assessment of the submerged inlet in the 1940's and 1950's.[19],[1] Laser Doppler velocimetry is a more recent data analysis tool and it requires seeding of the flow. Optical access can limit the regions accessible in some inlet configurations. In this inlet design, straight wall sections allowed optical access into the rectangular portion of the inlet before the flow transitioned to the diffusing duct and circular compressor entrance interface. One key parameter for this type of inlet configuration is the uniformity of the streamwise velocity.

LDV sensitivity pertaining to the secondary flows capability was examined prior to the detailed analysis of the submerged inlet using s-shaped serpentine ducts. The serpentine ducts created streamwise vortical structures which provided a good flow field to analyze with three component LDV. Working with the serpentine ducts allowed for an assessment of the measurement capability of the secondary flow components. In particular, the model assessed the accuracy of the w-component with a single probe head.[93] A numerical simulation provided a baseline for comparison. The details of the experimental setup follow in chronological order.

3.1 Serpentine Duct Experiments

Laser Doppler velocimetry and computational fluid dynamics were the main tools used to examine the serpentine ducts. Schlieren and hotwire analysis offered a rudimentary verification of basic flow features in the serpentine duct. The serpentine duct models and submerged inlet were constructed in SolidWorks and generated through the EDEN 333 Objet/Polyjet Stata system. The three-dimensional printer used FullCure M-720 model material to create the form. The resolution of the material was 16 microns in the x and z-direction and 84 microns in the y-direction. The resolution of the material is direction dependent in the three-dimensional printer.

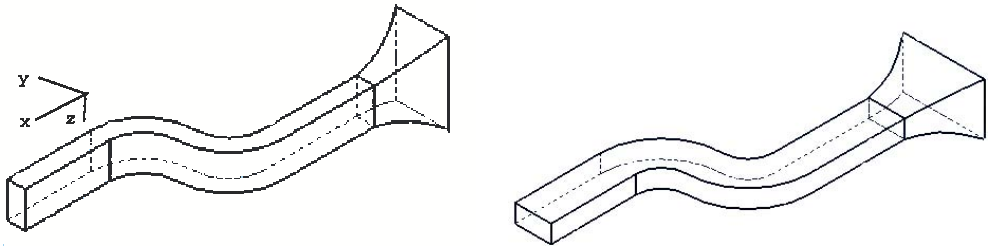

(a) horizontal (b) vertical

Figure 3. The flow path for the two aspect ratios of the serpentine ducts and the coordinate system applied to the data.

The serpentine duct utilized 6.35 mm thick sidewalls for optical visibility and the submerged inlet used 6.35 mm optical grade Plexiglas. The flow paths for the serpentine inlets are shown in Figure 3. Distortion and reflection of the beams passing through different mediums accounts for loss of information near the sidewalls of the models. It was important to understand the losses, since similar clear surfaces were mounted on the submerged inlet.

Each duct had a smooth bell-mouth contraction at the inlet and tapered to a 15.8 mm by 7.9 mm cross-section. The cross-section of the serpentine ducts was 15.8 mm by 7.9 mm from the contraction to the exit. The overall length of the duct was 110 mm from the bell-mouth. The flipped aspect ratio provides the difference in the models. The curvature of each bend was constant with a radius of curvature of 15.8 mm at the centerline. The aspect ratio in the direction of the bend served as the designation for the serpentine inlets. The term horizontal refers to the y_{exit}:z_{exit} being a 1:2 ratio, while the vertical has the y_{exit}:z_{exit} as a 2:1 ratio. The straight portion of the duct before the bends was four centimeters ensuring adequate boundary layer growth and uniform characteristics. This four centimeter distance was also utilized after the second bend. According to flow theory outlined in Wilcox[14] and Berger et al.[16], the distance is sufficient to develop the flow behavior and secondary flow created by the bends without redistributing the velocity profile to create the flow profile expected in a straight duct. The nozzles attached to a 0.0115 m^3 stagnation tank. The stagnation tank allowed the flow to settle eliminating pressure line effects.

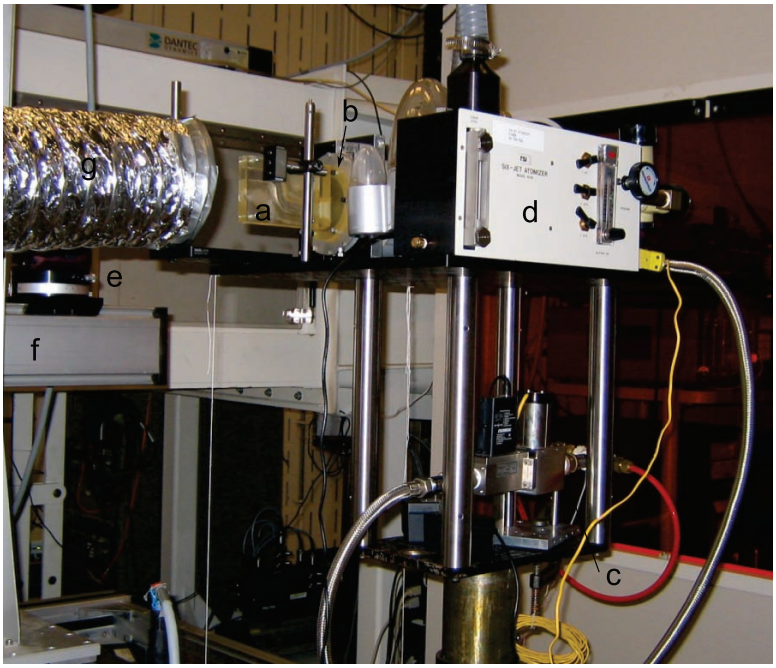

Figure 4. Serpentine duct setup used for the analysis with the LDV system.

Flow straighteners and a screen mitigated velocity variations from the tank. The setup for the serpentine ducts is shown in Figure 4. The features in Figure 4 are the (a) serpentine duct, (b) stagnation tank, (c) flow regulator (Omega FMA-2600A/FVL-2600A series), (d) atomizer (TSI Six-Jet atomizer Model 9306), (e) LDV probe head, and (f) Dantec lightweight traverse. The ducting after the nozzle,(g) in Figure 4, initiated a slight draw to capture the seed material (smoke) exiting the ducts for ventilation purposes.

The stagnation tank provided a means to seed the flow for the LDV studies. The flow rate is consistent with a mass flow rate of 0.00226 kg/s. The mass flow regulator fluctuated rapidly within ±5 SLPM of the set value. The stated readout accuracy is ±0.8% of the readout.[94] The accuracy for this experiment was 1.04 standard liters per minute (SLPM) of the reading. The mass flow controller's functional range allows up to 1500 SLPM depending on the supply flow. The 130 SLPM was within the Omega flow meter's capabilities. The mass flow added by the seeding particles calculated as two orders of magnitude smaller than that of the air flow. This small

addition of seeding particles was not accounted for in the velocities. The traversing systems were accurate to within ±0.05 mm in its positioning capabilities according to the specifications.[95]

Hotwire and Schlieren photography served as a preliminary means to examine the jet issuing from the serpentine ducts. These techniques allowed observation of some of the gross features of the exit velocity and flow pattern. The probe type obtaining the streamwise velocity measurements was a Dantec model 55p11. The hotwire has a 2.5 μm platinum plated tungsten wire with a 0.5 mm sensing length. The sensing length is large relative to the serpentine ducts' exit dimensions. The hotwire resolution sufficed in capturing gross features of the jet flow. The same stagnation tank and flow regulator maintained consistent conditions between the tests. The Schlieren and hotwire data were each taken at a mass flow rate of 300 SLPM, which was higher than the flow rate used for LDV data acquisition. The accuracy of the measurements of the mass flow rate were within 2.4 SLPM of the display value.[94] The ducts used for the Schlieren photography and hotwire measurements lacked the Plexiglas windows, the construction was fully the FullCure M-720 modeling material.

The Schlieren photography setup was the standard Z-shaped configuration, as shown in Figure 5. This technique captured the flow visualization of the jets as it exited the nozzle. The air temperature of the stagnation tank was 318°K (113°F), while the room was nominally 294°K (70°F). The temperature difference produced the density gradient necessary to visualize the serpentine duct's jet flow. A 100 Watt Osram mercury short-arc photo optic bulb served as the light source in the visualization, with two 0.3048 m spherical lenses focusing the light across the test section. The ducts oriented such that the initial bend was upwards in the y-direction. The knife edge, oriented horizontally, captured the density gradients in the y-direction for the serpentine ducts. The light focused into a Photron FastCam camera, with video captured at 4000 or 8000 frames per second. The viewing area prescribed the rate necessary to visualize the jet. The frame rate captured individual vertical structure movements and allowed tracking through the jet.

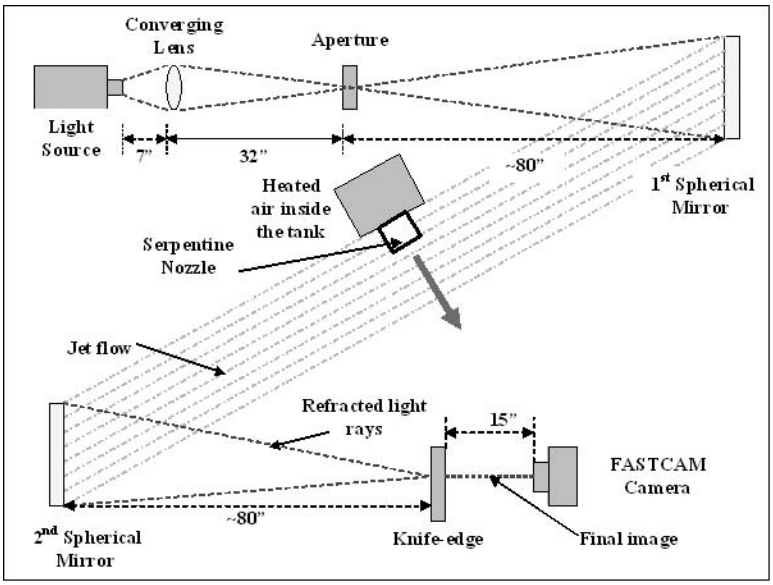

Figure 5. Standard Z-configuration for Schlieren photography.

The hotwire analysis performed by a single-component Dantec hotwire obtained preliminary measurements in two planes of the jet from the serpentine ducts. The first plane was five millimeters downstream of the exit, corresponding to 0.5 hydraulic diameters. The second measurement taken fifteen millimeters downstream corresponded to $2.0D_h$. A Dantec lightweight traverse and its software aid in the repeatability of the hotwire positioning in the jets for the desired grid pattern. The location from the jet visually confirmed by measurement ensured proper orientation and distance from the duct exit. Dantec's Flowform software implemented raw data processing on the measurements. Tecplot served to post processing the data. The grid spacing of the measurements for the hotwire in the jets was 1.0 x 1.0 mm in the y-z plane.

3.2 LDV

The backward scattering LDV system allowed resolution of all three components inside and outside the serpentine duct and the submerged inlet. A Dantec FiberFlow Probe, with a 112 mm diameter head and 5-beams, measured the three velocity components. A 5 Watt Argon-ion laser from Coherent (Innova 70c) provided the light source for the LDV. The Dantec FlowMap software processed the raw data for

Table 1. The dimensions of the probe volume for the FiberFlow three-component LDV probe.

	violet	blue	green
dx(mm)	0.046	0.047	0.050
dy(mm)	0.046	0.047	0.050
dz(mm)	0.388	0.792	0.835

export of the data for visualization. The conversion matrix, given in Equation 1, performed the component breakdown.

The power of each of the beams was maximized and balanced to provide the best quality signal for the measurements. Velocity measurements employed beam wavelengths of 476.5(violet), 488(blue), and 514.5(green) nm. The colors correspond to the measurements of u_2, u_1 and u_3, respectively, in this setup. The beam pattern (5-beams) was a cross with the center consisting of an overlapping green and blue beam. The two violet beams aligned parallel to the y-axis for the serpentine duct. The green and blue beams were nearly coplanar in the x-z plane, with the green beam in the downstream position and the blue in the upstream. A large screen placed three meters from the laser head led to the detection of a small out-of-plane y-component which was taken into account. The specific angles of the beam intersection were set by the 310 mm lens. Measuring the distance between the beams and the distance from the focal point to the screen subsequently verified the angles.

The beam spacing was nominally 37 mm for the 514.5 nm and 488 nm beams and 74mm for the lower power 476.6nm beam. The green and blue beam had a half angle of 3.40° and the violet had an angle of 6.78°. This provided the probe volumes given in Table 1. During the beam alignment, observation of the blue and green beams proved them to not be collinear. The small out-of-plane angle was measured using the projection on the screen. The v-component measurement was independent with the 476.5 nm beams. The w-component correction for this bias in the transformation is reflected in Equation 1. The transformation matrix substituted 0.1 for 0 in the second column of the third row to account for the observed beams positioning. This

value is equivalent to a correction for an approximately eight degree offset. The angle is consistent with the displacement of the beams on the screen projection. The magnitude of the w-component was the least accurate of the three components, consistent with the observations of Byrne[93]. The small angle made with the flow (3.402°) posed difficulty in accurate measurements. The resolution did, however, suffice elucidate the general trend and provide proof of the streamwise vortices.[16] This flow angle (3.402°) provided the conversion factors for the velocity, given in Equation 1, based upon the beam angle with the flow. The small offset angle for the blue and green beams has minor effects in the calculation of the u and v-component but is significant effects on the w-component. The correction factor derived from $1/(2\sin(\phi/2))$, accounting for the beam contribution to the w-component. The small angle did not change the velocity significantly for the u-component.

$$\begin{pmatrix} u \\ v \\ w \end{pmatrix} = \begin{bmatrix} -0.5009 & 0 & 0.5009 \\ 0 & 1.0 & 0 \\ 8.425 & 0.10 & 8.425 \end{bmatrix} \begin{pmatrix} u_1 \\ u_2 \\ u_3 \end{pmatrix} \begin{pmatrix} blue \\ violet \\ green \end{pmatrix} \quad (1)$$

The 40MHz Doppler shift, applied to the signal, made determination of flow directionality possible. The number or fringes detected determined the direction of the velocity components. The specifics of the LDV for the serpentine duct are presented separately from those of the submerged inlet. Both measurements used coincident mode with the same laser system. The signal filter applied the coincident mode to ensure the best accuracy of the information. Particles passing through all three beam volumes registered as actual data. The size of the burst window was limited to $10^{-}5$ to help maintain signal clarity. The size maintained high signal quality and prevented noise from biasing the data. The LDV settings remained consistent throughout the data acquisition unless stated otherwise.

3.2.1 Explanation of Fluctuating components. The mean velocity components do not define the flow behavior completely. Velocity fluctuations created by

the mixing region as observed in the hotwire results for the u'-component account for a small portion of the flow characteristics. The Reynolds stresses provide further information on mixing, the components associate with the energy content of the flow and define the flow evolution. This energy content increases in the mixing regions of the flow. The Reynolds stresses form from the combination and normalization of the momentum and energy equations. The classic definition of the Reynolds stresses, based upon the time averaged velocity and spatially varying flow, is given in Equation 2. The unknown component of the equation is the $\overline{u_i u_j}$, the components of the Reynolds stress measured by the LDV. The components of the Reynolds stress delineated further into the turbulent kinetic energy and the shear stresses. The $\overline{u_i u_j}$ components dictate the mean velocity profile.[13]

$$\overline{U_i U_j} = \bar{U}_i \bar{U}_j + \overline{u_i u_j} \tag{2}$$

The LDV software calculates the Reynolds stresses from the fluctuations of the mean velocity components. The software provides the values of u', v' and w' as well as the u'v', u'w' and the v'w'. The u'u' calculates from the u', v' and w'. The u'u', v'v', w'w', u'v', u'w', v'w' Reynolds stresses normalized by the square of the mean theoretical velocity. The Reynolds stresses evolved from the formulation in Equation 3.

$$\overline{u'v'} = \overline{uv} - \bar{u}\bar{v} = \sum \eta_i (u_i - \bar{u})(v_i - \bar{v})/N \tag{3}$$

A weighting factor η_i, employed in the LDV software, removes the velocity bias towards the faster particles measured through the validation mode, coincident measurement and overlap filter method.[98] The bias correction in η is a non-uniform weighting factor that uses statistical averages on individual particle or flow realizations. The factor is a transient time weighting that deals with the residence time of the particles in the measurement field.[98] The weighting factor is given in Equation .

$$\eta = \frac{t_i}{\sum t_j} \tag{4}$$

The bias generates from more high speed particles crossing the measurement region than low velocity particles. The weighting factor skewed the data averaging towards the slower particles to represent the flow. According to the data in a vortex core the values of η can range from 0.1-1.0 approximately for most of the data points, as shown in the paper by Martin, Pugliese and Gordon Leishman.(?) The software averaged the difference for each ith component away from the mean to obtain the fluctuations. Equation 3 is a specific representation, but the equation holds for all Reynolds Stresses. When components differ, as shown in Equation 3, they are shear stresses; when they are the same they are turbulent kinetic energy components.

$$k = \frac{1}{2}[(u')^2 + (v')^2 + (w')^2] = \frac{1}{2}\delta_{ij}S_{ij} \tag{5}$$

The turbulent kinetic energy is given in Equation 5. S_{ij} is a shorthand representation of the Reynolds stress tensor, while the fluctuating components comprise the kinetic energy components of the matrix. δ is the Kronecker delta, this matrix function selects the data where i=j. The fluctuating components, also known as the standard deviation (σ) of the mean velocity, is another representation of the Reynolds stresses. The fluctuating components comprise the turbulent kinetic energy components, as observed in Equation 6. All components are simplified for reference purposes by the elimination of the averaging sign, the operation implied. The standard deviation or fluctuating velocities have the same weighting factor, as given in Equation 3. The u' and u'u'-components are interchangeable, based upon the representation of the Reynolds stresses given in Equation 3 and the derivation of the fluctuating components given in Equation 6. The u'-component is the square root of the u'u' turbulent kinetic energy component. The correlation holds for the other fluctuating and turbulent energy components.

$$u' = \sigma = \sqrt{\sum \eta_i (u_i - \bar{u})^2} \tag{6}$$

3.3 Serpentine Duct LDV

Data acquisition occurred in both the jet issuing from the ducts and within the duct. In the latter instance, the beams passed through the acrylic side walls. The voltage of the photomultiplier was 900 V for measurements in the jet and 1000 V for the measurements within the serpentine duct. The higher setting of the photomultiplier ensured greater return of the back scattered signal to the probe. The change to the photomultiplier enhanced the signal to noise ratio observed in the burst windows for each beam. The overall power of the laser was ~1.5 W to maximize the particle count and rate for the LDV. Selection of the bandwidth for the velocity measurements facilitated maximization of the data acquisition rate and particle count. Care was taken to choose a proper center velocity and bandwidth while obtaining the measurements. The center velocity for the u-component was around 23 m/s with the v and w-components centered around zero. A bandwidth of 10 m/s accounted for the variation in particle velocity in the flow. Coincident mode in the LDV system ensured that only data only came from particles coming through all three volumes to maintain the highest data accuracy. The fluctuation of the mass flow controller accounted for a variation of 5 SLPM at 130 SLPM. A humidifier containing water outside the duct for the seeded the outer portion of the free shear layer to limit intermittency during the measurements. Particle seeding for the jet flow was introduced into the stagnation chamber by a TSI atomizer (model 9306). The atomizer, depending on the liquid, generated particles from less than 0.6 microns to 2 microns, depending on the seed material.[99] The seed material for the main flow was either water or Rosco smoke fluid. Examination of both particle types determined which provided the best particle rates for the duct while maintaining clear sidewalls for beam access. The small particle seeding addition had a flow rate that was two orders of magnitude smaller than the air flow rate. The small quantity of seeding affects the fluid properties minimally.

The grids for the y-z plane velocity measurements were 1 x 0.5 mm for the LDV system to ensure good coverage. The only exception was made at the x=15 mm location for the horizontal duct. A 1 x 1 mm grid served in the jet at this location

instead due to the expected increase in the grid size. The grid resolution resulted in 275 measurements locations at the jet planes, less for the interior of the serpentine duct. The transformation matrix, given in Equation 1, converted the measurements to the standard coordinates for the serpentine duct. Additional corrections were unnecessary for the flow field. The limitation of the w-component due to the small probe volume of a single laser head created some concern. A large sampling of 10,000 counts ensured the veracity of the velocity measurements. The sampling rate during these measurements was 100-1000 samples per second. Three repetitions of the data for the vertical duct verified the LDV grid sufficiently resolved the secondary components.

3.4 Numerical Simulations

The three-dimensional flow path within the duct geometry was constructed in the CAD program, SolidWorks. Gridgen (version 15.08) utilized the geometry file to create a grid of finite volumes. Fluent (version 6.2.16) imported the two different grids utilized for flow modeling. The initial coarse grid consisted of 70 nodes in the long direction of the inlet and outlet planes in the y-z plane and 40 in the short direction. For the entire length of the duct 175 grid points accounted for the last dimension in the preliminary simulations. The grid points were the nodal locations (490,000) generating the faces of the finite volumes for the calculations. Only the interior of the duct was modeled, no jet features were simulated in this study. The interior development sufficed in providing insight into the development of the flow features. The Reynolds number of the flow, based on the hydraulic diameter, was approximately 14,000.

The refined grid composed of four million nodal locations built off the coarse grid. The number of nodes for each dimension of the serpentine duct doubled, making the surface areas of the grid faces approximately a fourth of their previous area. In both the coarse and refined grids, the number of nodes were weighted towards the boundary layer for the greater resolution in predicting the small structures and its effect upon the flow field.[96] Smaller scale turbulence and the rapidly changing

velocities complicate predictions of the flow behavior if the grid spacing is large in this region. The solver makes small changes to the solution based upon the values at the centroid which represent the entire discretized volume.

The coarse grid examination compared the experimental results to two popular methods available in Fluent. The k-epsilon model sees widespread usage as an eddy viscosity model and RSM for directly calculates the Reynolds stresses. The k-epsilon model was an investigative tool for the coarsest grid. The accuracy of the k-epsilon model in this type of flow does not lead to highly accurate results due to the complex flow pattern involving separated flow and anisotropic turbulence. The results for the k-epsilon method were generally poor and not representative of the flow features seen in the experiment.[50] The convergence criteria for these solutions were a five order magnitude reduction of the residual. A turbulent model was necessary to capture the flow properties around the bends. Even though the flow was not fully developed, a laminar model was insufficient to predict the flow behavior.[50] Given the Reynolds numbers, the laminar model was unable to capture the vortices and pressure changes caused by the centrifugal forces around the bends and the subsequent flow field.[66] Default Fluent model constants apply unless otherwise stated.

A segregated steady implicit solver maintained continuity and prevented over-constraint of the solution. The inlet conditions were the conditions in the experiment, a flow rate of 0.00266 kg/s (130 SLPM) at 300 °K. The working fluid was air. The gage pressure for the outlet boundary condition value was zero, the serpentine duct entered into ambient conditions. For both boundaries the turbulent kinetic energy and the turbulent dissipation rate was 0.1 m^2/s^2 and 0.1 m^2/s^3 respectively. These values provided a starting point for the program and helped the solution development.

The discretization used for the half a million nodal points in the coarse grid was standard for the pressure and the first order upwind for the momentum, turbulent kinetic energy and the turbulent dissipation. The fluid in the duct for all cases initialized with a gage pressure of 500 Pa, an x-velocity of 5 m/s, y-velocity of 5 m/s,

and a z-velocity of 20 m/s at a temperature of 300°K according to the grid orientation in Fluent. The maximum value of the non-dimensional viscous sublayer parameter y^+ for the horizontal and vertical ducts is, respectively, 12.39 and 1.20 for the coarse grid. The y^+ being less than twenty guarantees that wall functions during the simulation were not applied, leading to more accurate results.(96) This parameter fully initialized the flow and enabled the program to solve for a steady state conditions.

The refined grid of four million nodes applied a higher order discretization scheme. First order discretizations are highly dissipative, preventing capture of the finer flow features that might be present, losing features of interest.(96) The third order differencing schemes for the pressure momentum, turbulent kinetic energy, turbulent dissipation and Reynolds stresses could not be initiated without prior development of some of the flow features. Time steps were too small for resolving the flow field. The lowest order discretization, first order results provided an approximation of the flow field for all of the differencing selections of the solver. The initialization allowed the solution to converge to the prescribed criteria. After the solution converged at the lower order discretization, the discretization scheme increased to the next higher order for one of the parameters and ran to convergence. This process repeated for the pressure, momentum and turbulent kinetic energy and dissipation as well as the Reynolds stresses to the highest discretization. The highest order discretizations in the program for these components are second order for pressure and third order for all of the previously mentioned parameters. The relaxation factors permitting convergence for the RSM model were 0.3 for the pressure; 0.8 for the density, turbulent kinetic energy and dissipation; 1.0 for the body forces and turbulent viscosity; and 0.5 for the Reynolds stresses. The y^+ calculated for the higher grid resolution is slightly lower than the coarse grid horizontal duct value of 9.36. The y^+ increased slightly for the vertical duct to 1.36.

3.5 Submerged Inlet Experimental Setup

The submerged inlet used the design from the RECITE project.[25] The Solidworks geometry scaled down to form to a manageable size for the low speed wind tunnel at AFIT. The submerged inlet is a standard NACA submerged inlet design with a seven degree ramp angle and straight 90° sidewalls that meet the ramp and the top surface of the model. Changes made to the model allowed access for the laser beams and the new flow control configurations. The modifications included the addition of a plenum for the flow control. The model partitioned into three sections, the nose, the ramp and transitionary section. The nose section leads to a boundary layer representative of a plane body ahead of the submerged inlet entrance. The model test section consisted of the ramp and transitionary section changing the rectangular entrance into a circular shape for a compressor. The rectangular section at the throat had an area of 7.14 cm^2. The overall length of the ramp and transitionary section is 36.0 centimeters. The ramp is 5.5 centimeters at the ramp section, in the spanwise direction, with a seven degree incline. The ramp begins after the forebody, just as the model straightens to form a flat surface.

The ramp and transitionary section are the only pieces altered from the original design, the ramp section contained the flow control. The location of the flow control jets were 5.6 cm for the step location, 9.2 cm for the flared ramp, and 9.5 cm for the straight ramp downstream from the beginning of the ramp section. The flow control holes have a bore diameter of 1.3 mm. A hollow cavity was made within the model, by means of SolidWorks and served as a stagnation chamber for the flow control. A hole made within the bottom of the hollow cavity facilitated the removal of support material and a duct through the ramp and transitionary duct sections used to feed air into the hollow cavity. The sidewalls of the ramp and transitionary section of the submerged inlet were removed up to the location where the geometry changes from rectangular to circular. This material removal allowed the ramp sidewalls replacement with 6.5mm optical grade Plexiglas providing access for the LDV into the region of interest. The measurement location was near the throat region of the inlet, with a

few millimeters of the actual throat. Black bracketing aluminum plates attached to the sides of the model simulated the fuselage to improve the modeling of realistic flow patterns. The assembled model is shown in Figure 6. The submerged inlet is given by (a)-(d) in the figure, with the letters corresponding as follows: (a) signifies the fore body section, (b) signifies the ramp section, (c) signifies the transition to round, and (d) signifies the black plates, as detailed previously. The black arrow delineates the two model sections, the ramp and transition to round proportions. Clay filled any gap between the model pieces, limiting the disruption of the boundary layer.

The other components shown in Figure 6 are (e) the exit line to the blower and the vacuum pump, for the few tests performed with the vacuum pump. The exit line was a 5.08 cm outer diameter pipe which was 0.63 cm larger than the exit area of the model. The feed line (f), for the flow control jets uses the same mass flow regulator applied to the serpentine ducts, the Omega FVL 2600A. The steel plate (g) attached to the model and was the base support throughout the test. The plate was a quarter inch thick steel and manufactured with the holes necessary to support the inlet models with the appropriate spacers. The plate was twenty inches long. The legs and plate (h) were used to situate the model at the required height for the LDV and secure the model to the tunnel floor. The bellows, denoted as (i) in Figure 6, allowed movement of the LDV probe while preventing air leakage into the test section. The holes were used to facilitate LDV access to prevent additional distortion of the beams in passage through a second section of Plexiglas. The Plexiglas sidewall of the wind tunnel had a second, smaller hole to allow exit line to pass out of the wind tunnel and alternatively, a vacuum line or the inlet of a blower.

The model design for the ramp and transition to round sections with the flow control chambers and flow control configurations are shown in Figures 7 and 8. The transition section remained unchanged throughout the series of tests. The change in the flow control cavity position from the ramp and step locations appears in the drawing of the second ramp configuration in the bottom of Figure 7. Figure 8 depicts the four flow control configurations studied more closely. The *straight step* configura-

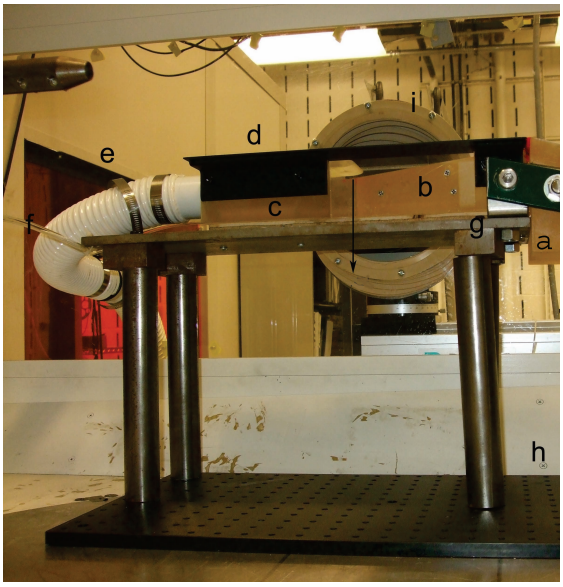

Figure 6. The submerged inlet assembly in the wind tunnel with the LDV system and connections to simulate the compressor and flow control addition.

tion was the initial design and the most extensively tested for jet effectiveness on the flow profile of the inlet. The term *straight* denotes that the channels used for the flow control run parallel to the sidewalls of the inlet. The term *step* refers to the geometry of the inlets with a backward-facing step at the initiation of the ramp.

Based on the literature, and some preliminary findings a second, *fanned step* inlet was built with the intent of energizing the flow along the ramp-wall corner. In this configuration, the channels used for the flow control are parallel in the center of the ramp and gradually change toward the sidewall. For both the *straight step* and *fanned step* inlet configurations, the flow control channels were angled downward by seven degrees to match the ramp angle.

Literature additionally suggested that the flow control proximity to the throat or AIP alters the effectiveness of the flow control. The second location evolved from this precept. The *ramp* configurations denote the flow control emerging from the ramp surface. The flow control at this location experienced cross-flow shearing since the flow was not inclined to follow the streamwise direction of the surface. The last two configuration designations are formed with this information. The *straight ramp*

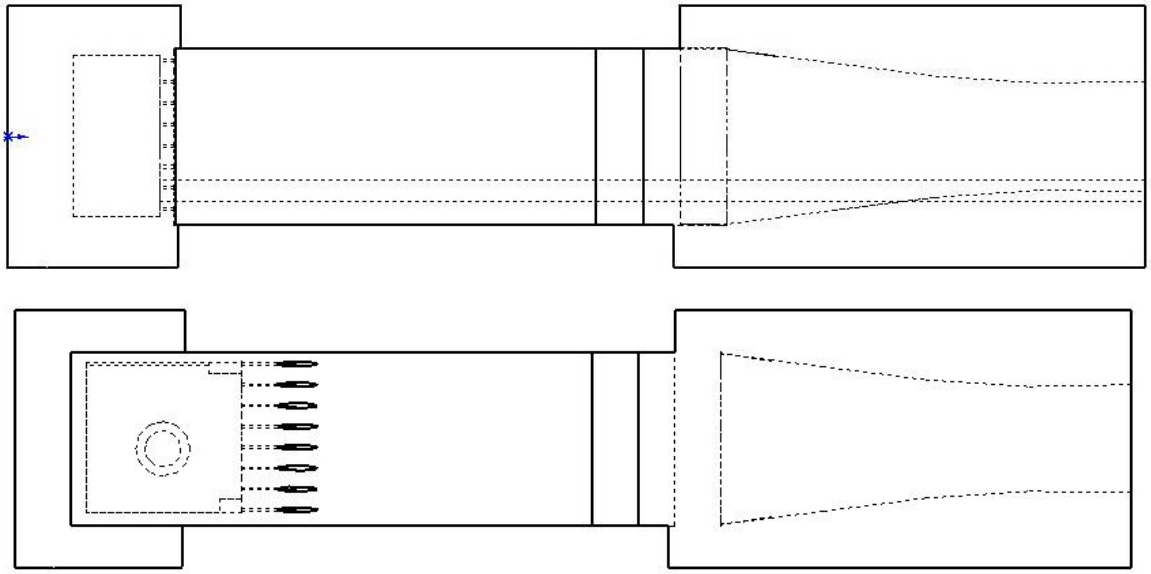

Figure 7. Top view (from the positive y axis) of the hole locations for a ramp and step configuration with the addition of the transitionary duct section to round. The length is 43.7 cm.

follows from the channels running parallel to the sidewalls and emerging downstream from the head of the ramp without the backward facing step. The *fanned ramp* is the downstream location emerging from the ramp with the intent of energizing the ramp-wall corner.

The full model and how the step locations relate to the ramp and transitionary section is shown in Figure 7. The ramp flow control enters further downstream than the step configuration. The flow control hole designs developed from the considerations presented from literature. The holes in the step configurations inclined to follow the ramp to reduce the jet separation on the ramp surface. The holes fanning at fixed angles and positioned further down the ramp became a consideration after observation of the straight step configuration. The angles of the flow control holes are -9, -6,- 3, 0, 0, 3, 6, 9 degrees for both fanned step and fanned ramp flow control hole configurations. These angles derived from previous jet mixing studies in co-flow and cross-flow jet injections.[92],[90],[91]

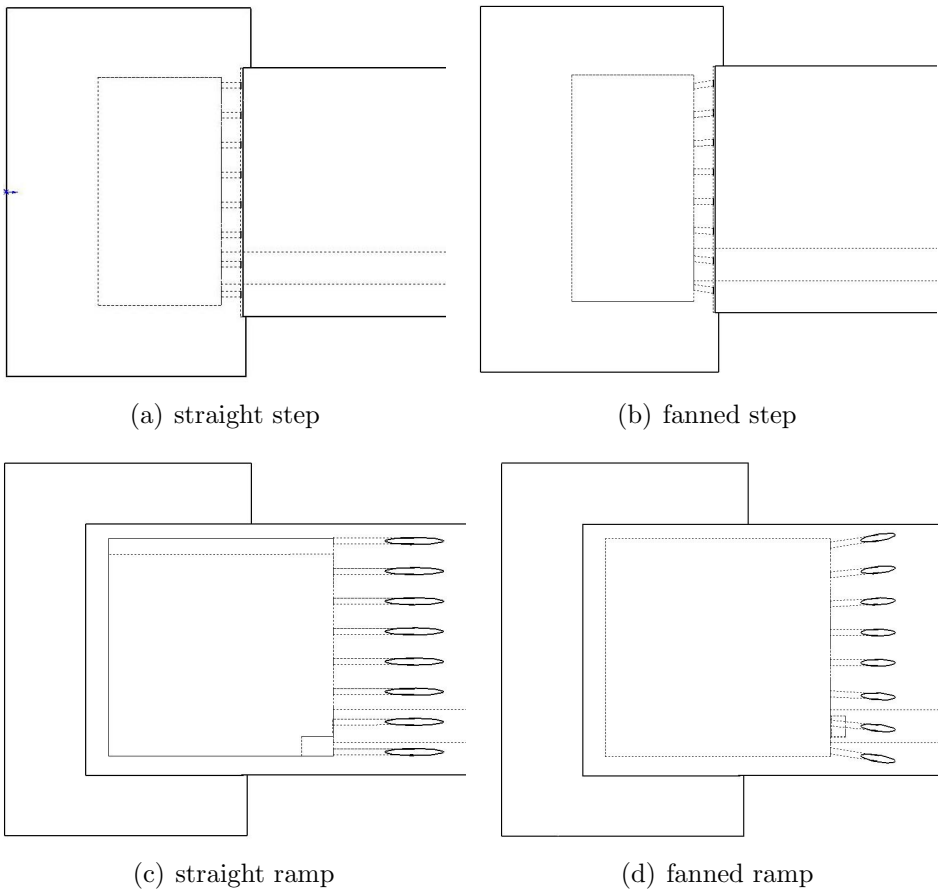

(a) straight step (b) fanned step

(c) straight ramp (d) fanned ramp

Figure 8. Flow control configurations viewed from the top for the four configurations examined.

The jets closer to the throat integrated into the ramp itself, as shown in Figures 8(c) and (d). Integration into the ramp surface prevented tripping of the flow from the wake of the backward facing step. Removal of the step prevented enlargement of the boundary layer due to the physical presence of the step. The small cross flow angles of 7 and 12 degrees relative to the ramp reattached after a small separation region.[88] The fanned ramp jet configuration has the same spanwise angles as given for the fanned step configuration, only inclined relative the streamwise flow. A positive five degree incline to the horizontal was required, due to material strength concerns, to allow the channels to reach the surface of the ramp, creating a 12° inclination to the flow. The channel inclination also aided in the prevention of the chamber being too close to the ramp surface. In an earlier configuration, the structural integrity of the

Table 2. Flow control configurations and location from the beginning of the ramp section as a percentage downstream. Distances were normalized by the ramp length to the lip of the inlet model (17.9 cm) and by the overall length of the ramp and diffuser sections (43.7 cm).

configuration	% lip normalized	% model normalized
straight step	31.2	12.8
fanned step	31.2	12.8
straight ramp	53.0	21.8
fanned ramp	51.3	21.1

model material was compromised during pressurization. The straight ramp configuration lacked this angle since the chamber was close to the ramp surface without risking failure. The inlet flow was incompressible and subsonic, and the slight angle used in the fanned configuration was not expected to lead to separation.[87],[88],[68] Minimal affects from the jets' exit trajectory in this instance incurred due to the low velocities. Applying the flow control jets directly at the ramp eliminated the need for a step. Relative to the beginning of the ramp section, the ramp configurations are 51.3% of the ramp length and 53.0% of the distance to the lip location. The decision to angle the flow toward the walls was an effort to eliminate the low pressure region formed at the wall and ramp juncture. This low velocity region typically translates into a lobe of pressure loss at the AIP.[25] Moving the flow control jets down the ramp determined whether decreasing the percentage of flow control related to the proximity to the throat. Calculations, based upon the mixing length, indicated that the jets at this downstream location were unlikely to yield velocity variations between the jets. Most of the data was obtained in the region near the throat of the submerged inlet.

The straight step configuration received more examination than the other flow control configurations. The goal of these tests was to prove whether the discrete holes were as effective as the slotted flow control case tested by AFRL.[25] Discrete line traverses and planar grids over half of the throat defined the effects for selected flow control percentages. The flows percentages examined for the configurations were the 0, 2 and 7 percent cases for the step configurations and 0, 2, 5, and 7 percent for the ramp configurations. These cases served in characterizing the effect of mass flow

control addition. The percentages held for all inlet flow speeds obtained by the blow and the vacuum line. The grids were performed for the slowest speed examined with the blower. The centerline examinations of the inlet throat were only performed at 1% mass flow additions for all tunnel and inlet speeds. The same grid cases determine if the added secondary component provided a benefit for the fanned ramp and fanned step.

Eight jets spanning the ramp width injected the flow control into the system. The flow entrances from the jet plenum were spaced equally across the ramp. The holes were four millimeter apart, with a jet diameter of 1.3 millimeters. Free jet theory suggested adequate downstream allotment for development by overlapping of the velocities.[14],[75] Two different methods determined that the jets overlapped and were continuous over the ramp width before reaching the submerged inlet's throat. One estimation method was the analysis of the turbulent development and spread of the jet being equal to the tangent of a thirteen degree angle, as given by White.[75] The other jet spreading method determined the overlap distance by solving for the z distance spread for the streamwise distance traversed. This laminar spreading rate is shown in Equation 7, where u/U_s is 50%, and in Figure 9. The value δ is parameter containing the streamwise distance with a factor built in to deal with particular conditions. In Equation 7 either a known value of x or z, depending on whether the distance required to meet, was of interest or the downstream position for the meeting of the jets. The U/U_s velocity distribution ratio of the centerline exit to the downstream location velocity was preset to make the distribution indistinguishable to within ± 0.01 over the 4 mm spanning the center of the jet. The distance calculated by the turbulent spreading rate methods determined that the jets would begin interacting 4.38 mm downstream for the turbulent tangent spreading angle of thirteen degrees. The jet interaction region according to the laminar method[12],[14] occurred 16.13 mm downstream of the exit plane. Both methods predict that mixing occurred quickly compared to the length from the flow control to the throat, which was 165 mm. The jets had sufficient mixing length, the eight jets adequately covered

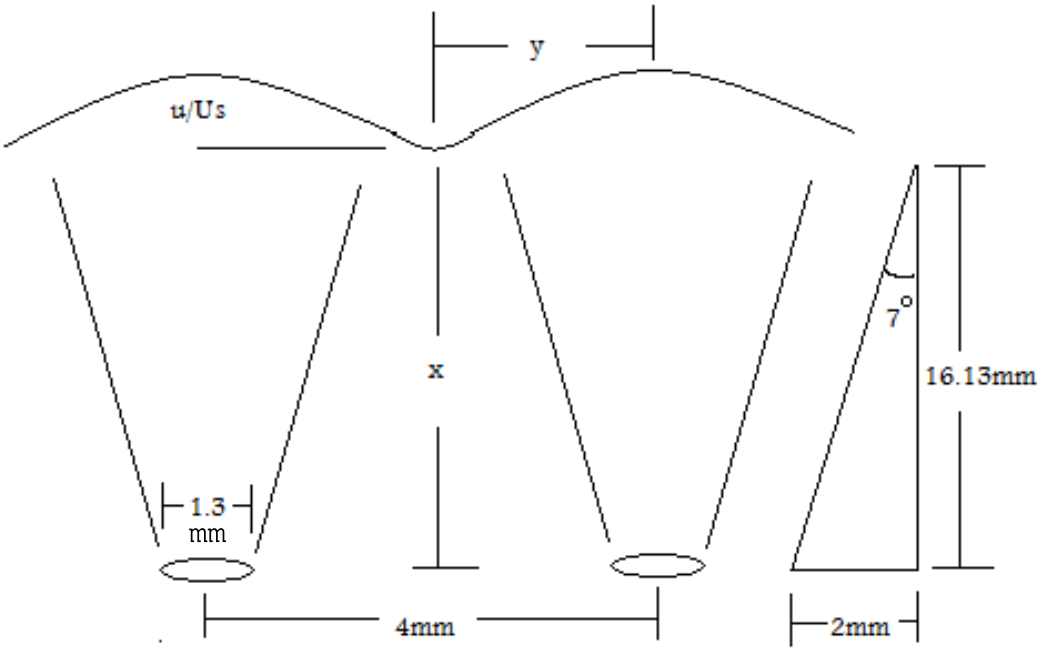

Figure 9. The jet spreading rate precepts associated with the laminar spreading rate and the calculation of velocity overlap region.

the ramp surface. Based upon the distance calculated downstream of the jet exit for the laminar method, the spreading rate for the jet was a seven degree angle. The laminar method was more conservative than the thirteen degrees predicted by the turbulent spreading rate.

$$\frac{U}{U_s} = \frac{U}{2.7U_0(\frac{d}{x})^{-0.5}} sech^2 \frac{z}{\delta} \tag{7}$$

The laminar analysis of the jet spreading is visually depicted in Figure 9. The application of the turbulent model follows with the triangular representation at the right of Figure 9, the seven degree angle replaced by the thirteen degree angle. The downstream distance calculates from the known information. The dimensions for the jet and the associated variables from the laminar jet spreading equation are shown in Figure 9. The core was the peak velocity region, so using the distance between jet centerlines provided a margin of error.

The discrete jets were proposed to increase the jet exit velocity along the ramp while decreasing the quantity of mass flow required. Personal communication of the

Table 3. The jet to inlet speed velocity ratio for a given mass flow percentage for the jets, based upon an average 49 m/s throat velocity for all four flow control configurations.

m_r	v_j/U_{av}
0	0
0.005	0.30
0.01	0.60
0.015	0.90
0.02	1.20
0.05	3.02
0.07	4.23

RECITE project's results formed part of the basis of this decision.[25] The RECITE model provided the form and a direct link to the submerged inlet study as it relates to the AFRL/RBAI study. AFRL/RB personnel actively engaged with this project. Capabilities at AFIT led to the decision to perform LDV and to apply viable methods of achieving flow uniformity based on literature. The hole dimensions and the measured averaged inlet speed used to calculate the velocity ratios are given in Table 3. The jet to inlet velocity ratio based upon the mass flow addition provided one method of characterizing the flow. Another relation is the inlet velocity to the freestream velocity U_{av}/u_∞. The freestream to inlet average velocity characterization is in all of the submerged inlet figures. The ratio demonstrated the inlet velocity compared to the freestream was large compared to most inlet studies.[97] The jet to inlet velocity ratio is given as m_r. The jet mass flow rate calculations used the measured flow through the inlet by a Rosemount 285 annubar flow meter. The accuracy of the annubar was 1 scfm. The meter calibrated to the flow based upon the expectation for the inlet and sized to the two inch diameter line from the inlet. Recalibration of the meter occurred for both of the expected flow speeds from the vacuum pump and the blower. The regenerative blower was an A-07047-65 from Cole-Palmer, delivering 215 cfm at optimal conditions, and equipped with a variable frequency drive to adjust to the flow rate.

The vacuum pump initially provided the inlet velocity for the submerged inlet with a freestream velocity of 60 mph. The vacuum pump experienced difficulties with sustained runs requiring constant draw on the vacuum pump. The pump design was for maintenance of a consistent pressurization state and therefore was limited to just a few cases. The vacuum pump provided benchmark trends for higher inlet velocities than those of the regenerative blower. LDV system found no issues with measuring the higher speed flows. The LDV is capable of measuring velocities into the supersonic regime. The only adjustment necessary was rotation of the probe head to accommodate the flow field velocities in the submerged inlet. The information obtained for these higher flow speeds were horizontal and vertical centerline traverses.

The majority of the tests used the regenerative blower. A lower freestream velocity for the wind tunnel compensated for the lower inlet velocity. No difficulties arose in sustaining a constant inlet speed for the study with the blower. With known flow rates for the inlet and jet velocity controlled by the mass flow controllers and flow meters, the runs performed consistently without difficulty.

3.6 Submerged Inlet LDV

Alignment and balancing of the beams before the tests for the submerged inlet enabled the best results. The probe head required rotation by ninety degrees to accommodate the bandwidth limitation for the u-component, as defined by the combination of the blue and green beams. Use of the violet beams avoided this limitation. The velocity was either positive or negative component for the violet beam and not tied to the characteristics of another pair of beams. The green and blue beams were opposite and balanced to each other in the program. As with the serpentine duct, the angle differentiated the flow velocity between the two directions from these beams, since they occupied the same orientation. The transformation matrix defined how the information translated from the beam configuration to the velocity measurements. Rotating the probe head to have the violet beams measuring the streamwise velocity posed no difficulty, so long as the matrix reflected the adjustment. The values are the

same as those shown in Equation 1. The only difference is that the positions represent the new orientation of the probe head towards the defined u,v and w components of the velocity. The first and second rows switched to provide the necessary calculations for the u and v-components. A reversal in sign for the u_1 and u_3 components account for the velocity direction in Equation 8. The u_1 component corresponded to the blue beam, the u_2 component to the violet beam and the u_3 component to the green beam.

$$\begin{pmatrix} u \\ v \\ w \end{pmatrix} = \begin{bmatrix} 0 & 1.0 & 0 \\ 0.5009 & 0 & -0.5009 \\ 8.425 & 0.10 & 8.425 \end{bmatrix} \begin{pmatrix} u_1 \\ u_2 \\ u_3 \end{pmatrix} \tag{8}$$

For the submerged inlet the photomultiplier was 1000 V for the green and blue beams and 1100 V for the violet beam to boost the gain and ensure signal quality. A weak burst monitor signal component compared to the others required an increase for clear examination in the same manner as the other beams. The power of the laser itself increased to maximize the particle detection rate. The value for the beam power was a stable maintainable value. Beam fluctuations, which might be misinterpreted as incorrect velocity readings, were avoided. The Coherent 70c produced up to five Watts of beam power. The total power outputs ranged from one and half to three and a half Watts based upon the acquisition rate. Low acquisition rates, under one hundred counts per second, required a power increase to accommodate for the low backscattered signal. More particles detection occurred with the higher power with an increased data rate and reliability of the measurements. The controller maintained the beam power with the amperage adjustments keeping the power at the desired setting. The sampling size for each position in the submerged inlet was 5000 data samples or a maximum residence time of 5 minutes. The submerged inlet at all positions obtained 5000 data samples. The data rate was 500-10,000 samples per second. The half plane grids collected at the throat consisted of 375 measurement locations while the linear traverse investigations consisted of 68-105 measurement locations.

The linear traverse studies examined the correct alignment of the beams with the Plexiglas sidewalls. The observation of a bias in the w-component at the centerline led to a slight adjustment in transformation matrix so that the quantitative flow field could be obtained. With the bias removed by the examination of the line studies, the w-component behavior became clearer for the grid studies. This bias of the w-component formed from the slight rotation of the laser head created by the bellows and the distortion of the beams from the Plexiglas. Corresponding adjustments compensated for the bias in the transformation matrix upon completion of the measurements, during reprocessing of the velocity data. The w-component provided a basis for the vorticity and secondary flow behavior with less emphasis on the value of the w-component velocities.

3.7 Submerged Inlet Particle Seeding for LDV

Prior experiments relied on intrusive probe techniques of total pressure probes and hotwire measurements of the streamwise velocity at the throat or the aerodynamic interface plane (AIP). These intrusive flow measurements required flow accessibility but not optical access to the measurement plane.[59],[17] Visibility in the serpentine duct was necessary for one interior location since measurements in the jet did not require optical access. The interior measurements of the serpentine duct demonstrated the importance of sidewall clarity for seeding and LDV access. Maintaining clean sidewalls for the submerged inlet was a high priority for this test, particularly in obtaining the secondary velocity components. Pressure probes and hotwires interact with the flow while the LDV technique relies on light reflected off the particles. Laser Doppler velocimetry (LDV) is non-intrusive, apart from the particle seeding requirement, and application closer to surfaces is possible. Particles must provide sufficient backscattering of the signal to enable flow measurements. Optical grade Plexiglas, 0.635 cm (0.25 in) thick, formed the sidewalls of the submerged inlet.

From some trials with the serpentine duct, the use of conventional seed particles posed a problem. Both the Rosco smoke juice and water atomization accumulated

on the Plexiglas sidewalls over time during the test. The accumulation hindered or blocked beam access to the flow field. Acquiring the desired measurements within the submerged inlet required no accumulation over a long period of time. Run time acquisitions were long for the grids in particular. Avoiding of seeding Localizing the seeding to only the area necessary for the inlet flow was an additional consideration for an alternative seeding method.

In a joint study between AFIT and Innovative Scientific Solutions Incorporated ISSI, a novel seeding arrangement developed. Steam and liquid nitrogen combined to form stable seed particle of a submicron size. This combination provided formed a localized region of fog which provided the required particle density level without surface accumulation. The liquid nitrogen rapidly condensed the steam particles to give them greater visibility to the laser allowing the particles to persist to the measurement region. Fogging rates were often increased to aid adjustment of the particle stream into the path of the inlet, but most data was collected with the fog region barely visible. While the LDV can be collected for a range of particles sizes, submicron particles perform best in terms of the flow.[98] A consistent particle size reflecting the light back to the receiver is desirable. According to Dantec Dynamics, "All flows have natural aerosol or particle content. Density and unknown size distribution makes it essential that seeding particles be added to flows and should be chosen for high signal quality."[98] This motivated the use of a stable consistently sized particle stream.[98],[95]

The steam and liquid nitrogen particles fell within the range that the LDV system detects. Another representation is combustion particles for the size. Combustion particles range from 0.01-0.1 micrometers.[100] The particle sizing for the liquid nitrogen and steam, based upon these two particle examinations from combustion and atomization, show that the particles are of the size capable of representing the flow features. Based on observation, the particles are likely in the submicron range, though actual measurements are needed for verification. Usage of the steam and liquid ni-

trogen particle mixture was required that the equipment producing the particles and introducing the particle stream be positioned upstream of the wind tunnel.

A few iterations brought the seeding system to its final functional state. The first trial of the seeding utilized steam injected from the relief of a simple pressure cooker into a line held at the end of a PVC pipe introducing the liquid nitrogen to the steam. This initial effort verified that the LDV system detected the particles and captured tunnel velocities. The seeding bursts provided by this preliminary steam and liquid nitrogen mixture provided accurate flow information, when compared to tunnel instrumentation.

In a second iteration, a stable method to support the PVC injector and mix the steam and nitrogen allowed self-support of the seeding system. A nozzle affixed to the end of the PVC pipe for liquid nitrogen injection and a steam generator supplied a stable continuous source of steam. The steam generator had a primary reservoir where the heating occurred. This primary reservoir drew from a pressurized secondary reservoir that moved the water from this reservoir to the steam generator. The mixing length pipe for the steam and nitrogen attached to an adjustable tripod, which ensured stability while providing a means to position the seeded region within the wind tunnel. This setup allowed consistent particle generation. There remained a slight problem with the spatial stability of the particle stream entering the wind tunnel. The drift of the particle stream was very pronounced and required constant adjustment to keep it within the measurement region. A second tripod with a large outer pipe to help straighten and stabilize the flow corrected this problem. Ambient air currents were damped and the entrance location of the particle stream was stationary. The outer pipe acted as a cowl to ensure the flow entered in straight around the seeding. Air currents changing the entrance of the particles into wind tunnel inlet and thus the location in the test section affected the seeding far less. Varying flow speeds in an empty tunnel confirmed that the particles provided accurate results over a range of speeds based on the tunnel's capabilities.

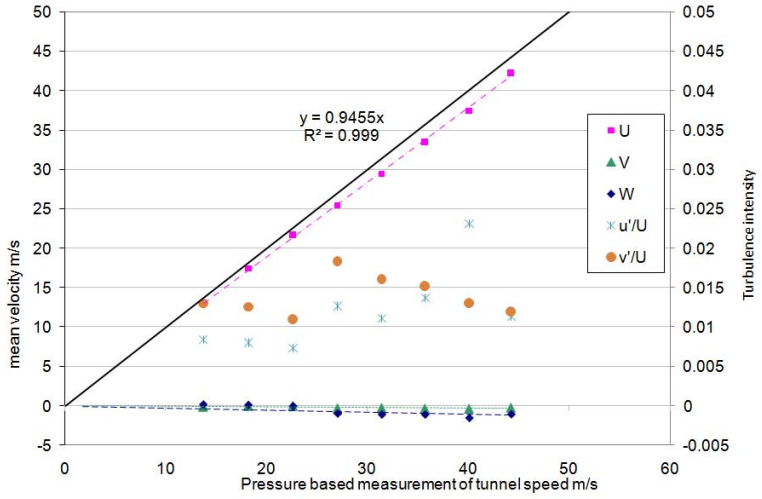

Figure 10. Tunnel verification to check match between the LDV system and the expected tunnel speed while providing some turbulence analysis.

As expected, the particle stream's cross-sectional area became more compact with increased flow speed, requiring more adjustments to position the seeding system in the wind tunnel inlet. The reduction of the particle stream area was consistent with basic flow theory. The length of time for particles dispersion had a small effect on the seeding area for the range of conditions used in the experiments. The particle density proved no issue for the LDV system, provided the beams crossed within the particle stream. The signal collection and data processing by the Dantec Flowform software resulted in tunnel velocities and turbulence data. A variety of tunnel speeds in the freestream verified the seeding. The velocities examined were flow speeds from 13.41-49.17 m/s (30-110 mph), as shown in Figure 10. The w-component and w'-components verified that the single five-beam probe had resolution difficulties with the small beam angles created by the green and blue beams. The w'-components were five times higher than the corresponding u' and v'-components.

While the particle stream was more stable with the addition of a cowl, adjusting two stands was slightly unwieldy. The cowl (a) was oversized, as can be seen in Figure 11, as was the mixing length of the tube (b). The mixing tube was a meter long. The steam entered through a y-fitting (c) to the PVC pipe and the liquid

Figure 11. Second seeder configuration that used a large outer cowl to stabilize the flow.

nitrogen though a nozzle (d) a few centimeters upstream of the steam. The secondary pressurized reservoir (e) and the steam generator (f) are also shown in Figure 11. These components were essential for a stabilized seeding flow and carried over into the next more compact design configuration. The secondary reservoir required refilling after approximately two and a half hours. The primary reservoir had a manufacturer designed level of water in order to guarantee the steam generator's consistent output of particles. When the secondary reservoir was nearly emptied, the particle stream became intermittent. The primary reservoir was unable to maintain its operational level. Under this condition particles released irregularly instead of the consistent output. The 2.5 hour time period sufficed for data acquisition.

Based upon these recommendations from the field tests performed in the low speed wind tunnel, the third and final configuration evolved in coordination with ISSI. The outer cowling and the mixing length tube combined to make a more stable and compact system, easily maneuvered on one stand, as shown in Figure 12. The steam and liquid nitrogen both entered from the upstream side of the mixing length tube through fixed nozzles, shown in Figure 13. The tank of liquid nitrogen is visible behind the seeding system in both figures. Figure 12(a) provides a closer view of the seeder attachment to the tripod. The flow direction is indicated, and the seeding

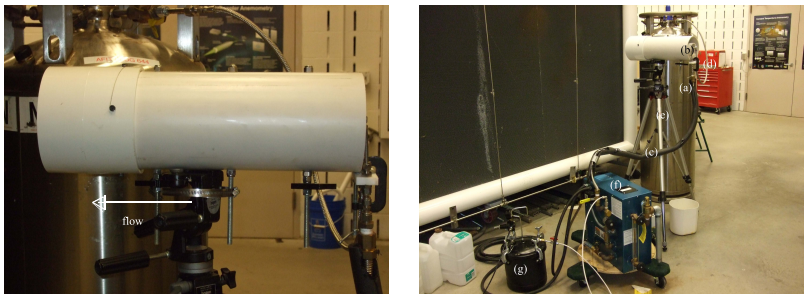

(a) side (b) entire seeder

Figure 12. Seeder configuration used for acquisition of the velocity measurements in the submerged inlet.

nozzles are at the back of the seeding injector (PVC tubes acting as the mixing length and cowl that introduced the seeding particle stream to the entrance of the wind tunnel). The components displayed in Figure 12(b) are (a) the liquid nitrogen tank, (b) the seeding injector, (c) the steam line feed, (d) the liquid nitrogen line feed, (e) the tripod, (f) the steam generator and (g) the secondary pressurized reservoir. In Figure 13 a view of the injection system reveals that it consists of two concentric PVC pipes. The two pipes bolted together to prevent relative movement to each other. A honeycomb structure, like that used in the wind tunnel entrance, is positioned at the exit of the pipes to straighten the flow through the cowl of the injector. Referring to Figure 13, the parts of the seeder are (a) the steam injector, (b) the liquid nitrogen injector, (c) the mixing length tube, (d) the cowling and (e) the holder for the injection nozzle and its attachment to the entrance of the seeding injector. The liquid nitrogen enters upstream of the steam due to the higher pressure. The line from the liquid nitrogen tank was a cryogenic line preventing breakage and leakage due to the extreme temperatures imposed. When the steam and liquid nitrogen mixed at proper ratios, based upon physical observation, a stable particle stream formed. The particle stream only drifted a few centimeters in any direction around its central location unless conditions altered.

The particle stream in this final configuration required minor adjustments during the entire test run. The operational procedure required some time and experience to

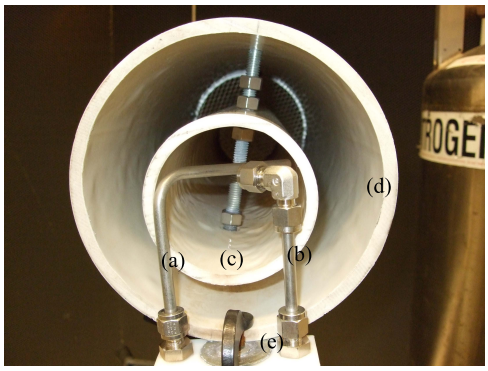

Figure 13. Nozzle configuration that produced the best performance for particle generation.

attain this finalized functioning system. Slight adjustments to the valves controlling the steam flow and liquid nitrogen were often applied when the seeder was initially set up for an experimental run. The correct ratio of steam and liquid nitrogen provided the longest lasting seeding capabilities with a stable, effective particle stream. The steam nozzle was directed into the sidewall of the mixing length tube to dissipate the forward momentum of the steam particles, while the liquid nitrogen nozzle was pointed directly at the tube delivering the steam. Directing the nitrogen at the steam nozzle initiated the cooling process, disrupting the liquid nitrogen's momentum. Only a small amount of liquid nitrogen was needed to bring the particles to a temperature that prevented excessive drift in the wind tunnel. The 180 liter liquid nitrogen tanks pressurized at 100-230 psi lasted from 18-30 run hours. The estimate neglects the loss of nitrogen from the bleed valve. The value prevented over-pressurization. The nozzle cross configuration as worked the best, opposed to parallel streams mixing within the length of the pipe. The nozzle cross configuration is where the steam was directed into the side wall with the liquid nitrogen being directed at the nozzle of the steam. Crossing the streams nullified the inherent momentum imparted by the pressurized systems and initiated the cooling more quickly for particle formation.

The exit temperature played a significant role in the particle stream due to buoyancy. More than a few degrees difference in temperature from the seeding stream to the entrained air, as discerned by touch, was sufficient to shift the particle stream

Figure 14. Particle seeding interaction with the LDV beams above the submerged inlet for freestream measurements.

from the measurement region. Particle temperatures that were too hot or cold relative to ambient conditions created a tendency to drift up or down, respectively, based on seeding buoyancy. Ideally the particles exited at close to ambient temperature, essentially neutrally buoyant. The conditions for a neutrally buoyant mixture meant valve settings for the steam and liquid nitrogen varied on a daily basis with the humidity and ambient temperature within the lab. The 689 kPa (100 psi) pressured tank appeared to last longer than the 1.586 MPa (230 psi) pressurized liquid nitrogen tanks and therefore the lower value for pressurization is preferred. The temperatures experienced in the lab ranged from 18.33-35°C (65-95°F). The ratio of liquid nitrogen and steam changed accordingly to compensate for the temperature variations. De-ionized water eliminated the buildup of particles within the steam generator. The tap water led to accumulation of sediments in the reservoir during residency. The accumulation of particles in the system carried into the steam and was generally undesirable.

The seeding particles generated from the combination of liquid nitrogen and steam is shown passing over the top of the model in Figure 14. The particle density in Figure 14 is greater than required for measurements in the submerged inlet. The laser beam can be seen in this figure, and the measurement volume location is 7.0 cm above the submerged inlet to obtain freestream information. Each of the three different beam colors are visible as is the beams' measurement region, the focal point of the four individual beams, and the combined center. The seeding particles show the focal point at the centerline of the submerged inlet in Figure 14. The seeding particles

are localized to the proximity of the submerged inlet, as indicated by the absence of the beams' presence to either side of the submerged inlet. The absence confirmed limited particle persistence since no reintroduction occurred in the wind tunnel. Beams would have been visible for the entire width of the wind tunnel for theater smoke, not contained in the manner shown in Figure 14. To conduct measurements within the inlet, the exit of the steam and liquid nitrogen was positioned slightly lower near the tunnel inlet.

IV. Serpentine Duct Results and Analysis

The two serpentine duct geometries served as a preliminary evaluation of the three-component laser Doppler velocimetry system for use in the submerged inlet. The same LDV system obtained measurements in both the serpentine ducts and submerged inlet. The detailed examination of the velocity profiles evidenced the expected secondary structures and turbulence values for computational validation. The presence of the anisotropy of the flow created by the curvature, in general, made it difficult for some models to accurately capture the flow dynamics.[101],[63],[65] Validation of the LDV system using serpentine ducts allowed confidence in measurements for the submerged inlet. Measurements of the turbulence statistics indicated the accuracy of the LDV system and provided information for comparison to the computational studies. The results offer insight into proper turbulence modeling in the presence of anisotropy. The theoretical average velocity based upon the set flow rate from the mass flow controller provided the value for the serpentine ducts. As done in literature the averaged form is implied, the overbar was dropped for simplicity.[13]

The complicated nature of the submerged inlet made a simplified preliminary geometry investigation desirable. The serpentine duct served this purpose. The flow development shared similarities in having two flow turnings and expected vortex formation. The settling chamber and bell mouth allowed the flow to enter uniformly. Two full ninety degree bends were chosen produce the secondary flow. The accentuated flow turning determined the velocity sensitivity of the LDV system to the secondary flow. If the dominant vortex structures created by this duct system were not resolved by the LDV, the system would not likely capture the secondary flow created by the sidewalls of the submerged inlet.[2],[3] The flow path for the serpentine duct with its orientations and axis system oriented from the flow perspective are given in Figure 15. The primary flow is right to left in the figure in the positive x-direction.

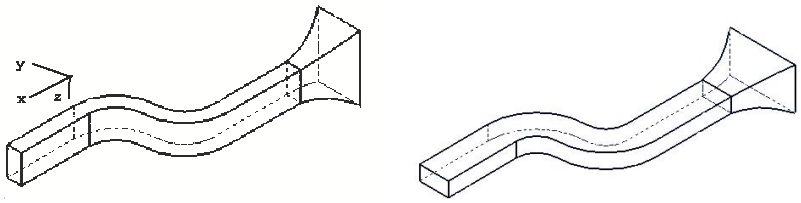

(a) horizontal (b) vertical

Figure 15. The flow path of the serpentine ducts examined by the LDV system and the designation based upon the aspect ratio in the y-z plane.

4.1 Schlieren and Hotwire Examination

Schlieren photography and one-component hotwire anemometry obtained some general characteristics of the jet profile of the serpentine ducts. Higher temperatures than the LDV and hotwire experiments permitted flow field resolution through density gradients. Both the Schlieren and hotwire cases performed at over twice the flow rate of the LDV measurements. The flow rates were 300 SLPM for the hotwire and Schlieren studies compared to the 130 SLPM flow rate for the LDV system. These flow rates corresponded to a theoretical average velocity of 35.56 m/s and 15.41 m/s, respectively. The Schlieren study allowed a very general analysis of the jet exit structure in its development and growth. The growth of the jet indicates asymmetry in the flow and that the secondary components creating a preferential direction in the growth. Likewise, the lack of a preferential direction stems from a more symmetric flow within the jet. The jet issuing from the horizontal duct is shown in Figure 16(a). Greater mixing appears in the lower half of the jet, the negative y-direction, with large strong coherent structures. The jet emanating from the vertical serpentine duct is shown in Figure 16(b). Examination of the moving images indicated the upper portion of the jet from the horizontal duct moved faster than the lower portion. While less evidence of the velocity differential appeared in the vertical duct, slightly higher speeds emerged in the upper shear layer. This is consistent with both serpentine ducts experiencing a core shift towards the outside of the second bend.[10],[11] Further examination through the hotwire and LDV analysis shed more light on the mixing occurring within the serpentine duct's jet.

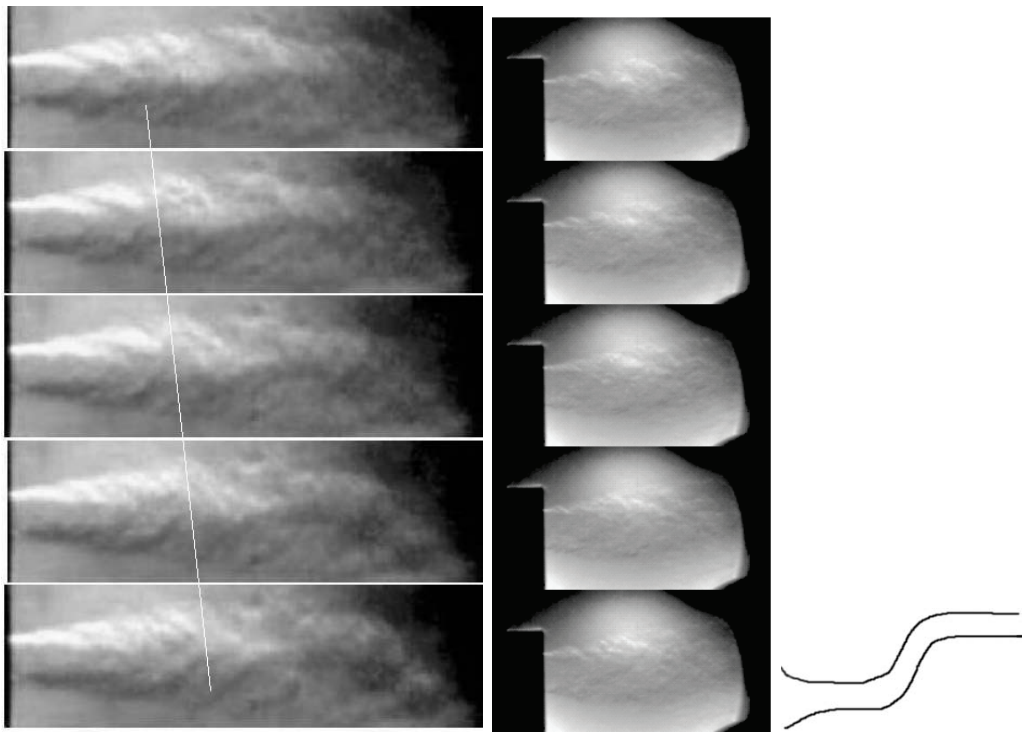

(a) horizontal duct at a frame rate of 8000 frames per second (Δt=0.000125)

(b) vertical duct at a frame rate of 4000 frames per second(Δt=0.000250)

(c) flow path

Figure 16. Consecutive snapshots of the ducts jets at the 12 o'clock orientation. The observation point of the jet is from the side. The line indicates the motion of a vortical structures on the lower portion of the jet.

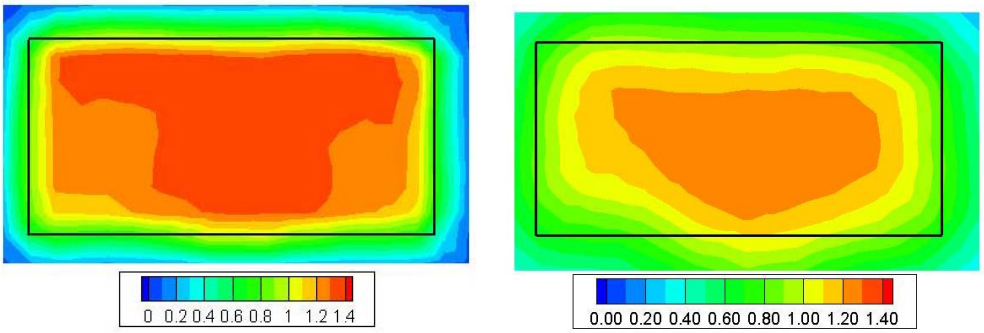

(a) x=0.5D_h u/u_{avt} (b) x=2D_h u/u_{avt}

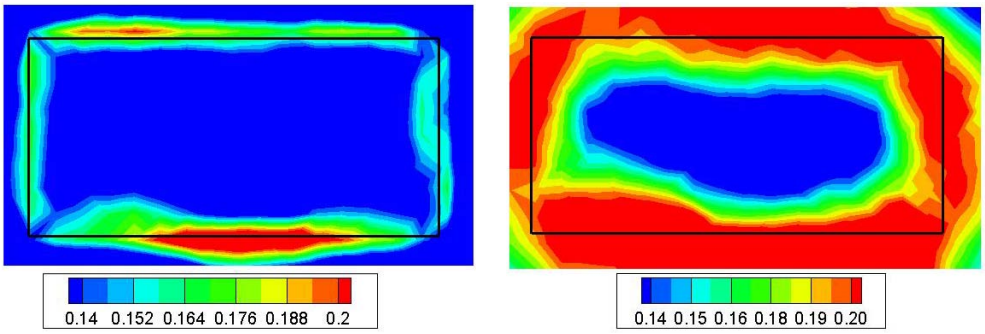

(c) x=0.5D_h u'/u_{avt} (d) x=2D_h u'/u_{avt}

Figure 17. Single component hotwire results for the streamwise direction, mean u-component of the velocity and the variation for x/D_h =0.5 and 2.0 for the horizontal duct.

The hotwire system yielded the mean velocity and its u'-component of the turbulence for the two jet configurations. The hotwire results for the horizontal jet are shown in Figure 17. The mean component of the velocity at x/D_h=0.5 and x/D_h=2.0 is given in Figure 17(a) and (b), respectively. The standard deviation of u (u') is given in Figure 17(c) and (d) for two jet locations. The horizontal duct exhibits a well-defined core region that has a higher streamwise velocity near the top portion of the jet. The velocity shift was consistent with the higher velocity along the outside radius of the duct.[11] The flow has a natural tendency to become more uniform with downstream development after the second bend due to the exchange of momentum.[79],[12] After any significant curvature the skewed velocity profile emerges, milder curvature is less pronounced. Whitelaw and Murthy[102] as well as Ferdman, Otugen and Kim[78]

Table 4. Normalized velocities for both of the serpentine ducts u_{avt}. The 130L/min flow corresponds to the 0.00226 kg/s used for the numerical results.

Test	flow rate(L/min)	Average(m/s)	Re_{D_h}	De_{D_h}
Schlieren	300	35.56	20,700	11,800
hotwire	300	35.56	20,700	11,800
LDV	130	15.41	14,000	8,000
numerical	130	15.41	14,000	8,000

saw this clearly in their simple 90° bend cases. In each case the core flow, or high streamwise velocity region, migrated towards the outer curve of the duct.

The turbulent kinetic energy component, u', increases along the edges of the jet where mixing with the ambient air occurs in Figures 17(c) and (d). All velocities normalized by the theoretical exit velocity, determined from the volumetric flow rate and exit area of the serpentine ducts. The theoretical average velocities u_{avt} are given in Table 4. A distinctive region in the lower portion of the jet experiences more velocity fluctuation than at any other peripheral location. This high fluctuation region corresponds to the location of the low streamwise velocity. The higher fluctuations are indication of the secondary motions redistribution of the core velocity. The regions of fluctuations denote the evolution and change created by the velocity deficit from the core shift and the secondary structure interaction.[16],[17] With only one component of the velocity, results are inconclusive in proving the existence of the secondary flow and vorticity.

The vertical duct received the same hotwire analysis. The results of this study are given in Figure 18. Figures 18(a) and (b) display the shift of the streamwise velocity and the jet spreading over the streamwise distance traversed. The vertical duct confirms that the aspect ratio change does not alter the velocity shift toward the outer portion of the curved duct, reported in other experiments.[16] The core shift becomes more pronounced in the vertical duct, greater height in the y-direction. The aspect ratio contributes heavily to the extent of the velocity shift and the size of the velocity deficit region. Regions of lower velocity and velocity interaction experience higher turbulence, which is an indicator of mixing. The turbulent kinetic energy, u',

for these two jet locations are shown in Figure 18(c) and (d). A more substantial region of larger Reynolds stresses forms at the bottom of the duct, as indicated where the streamwise velocity is lower. The velocity fluctuation region again increases in size with downstream distance, as expected for growth of the jet. The growth of the velocity fluctuations appears consistent over the entire jet boundary. This agrees with the Schlieren photography for the vertical duct. The horizontal jet shows a larger growth of the mixing layer towards the lower half of the duct in comparison to the top and sides.

Although the evolution of the jet proved interesting, data downstream of the duct exit provided limited insight into the flow within the duct itself. The region of large fluctuating velocities is more substantial in the vertical duct. The LDV profile facilitates measurements of the secondary velocities and Reynolds stresses. The secondary velocities elucidate the higher turbulence regions.

4.2 LDV Examination of the Horizontal Duct

The majority of the data collection occurred by LDV at three locations: 5 mm upstream of the duct exit, and at the locations of the hotwire measurements. The jet locations were the half and two hydraulic diameters downstream of the duct exit. The computational study resolved the interior of the duct, only the exit profile compared to the LDV data. This approach confirmed the LDV system captured the flow features.

The progression of the measurements for the horizontal duct for the mean velocity components are given in Figure 19 for the u-component, Figure 20 for the v-component and Figure 21 for the w-component. The measurements normalized by the theoretical average velocity, as given in Table 4. The secondary velocity vectors superimposed upon the streamwise velocity profiles to visualize the secondary flow's contribution to the flow development. The secondary flows originated from the turning in the serpentine duct and the differences in the velocity created by the core shift. This made it useful to observe the correspondence to the literature.[17] Either two

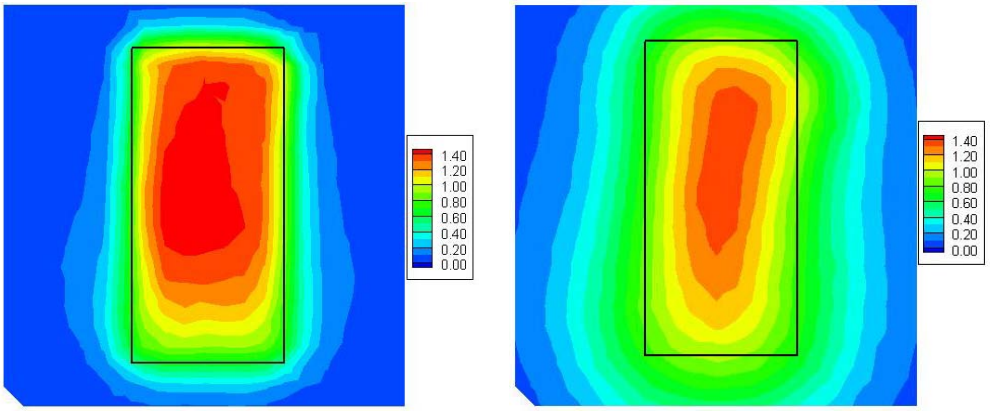

(a) x=0.5D_h u/u_{avt} (b) x=2D_h u/u_{avt}

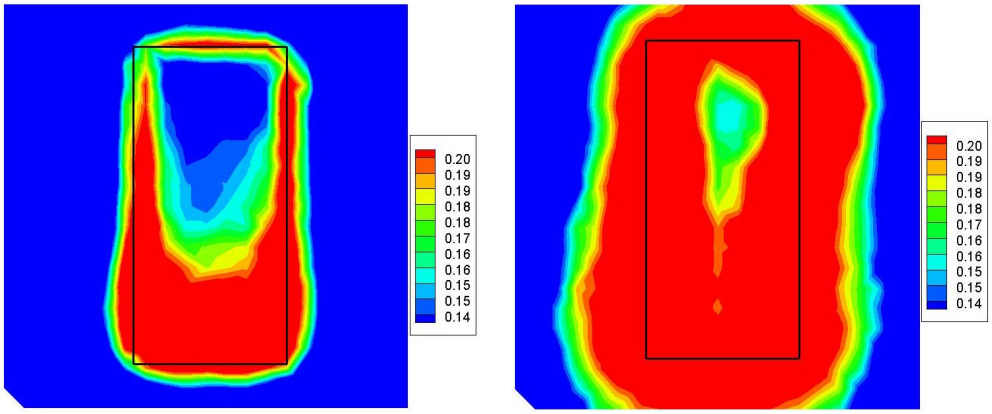

(c) x=0.5D_h u'/u_{avt} (d) x=2D_h u'/u_{avt}

Figure 18. Single component hotwire results for the streamwise direction yielding the mean u-component of the velocity and deviation for one half and two hydraulic diameters from the exit plane for the vertical duct.

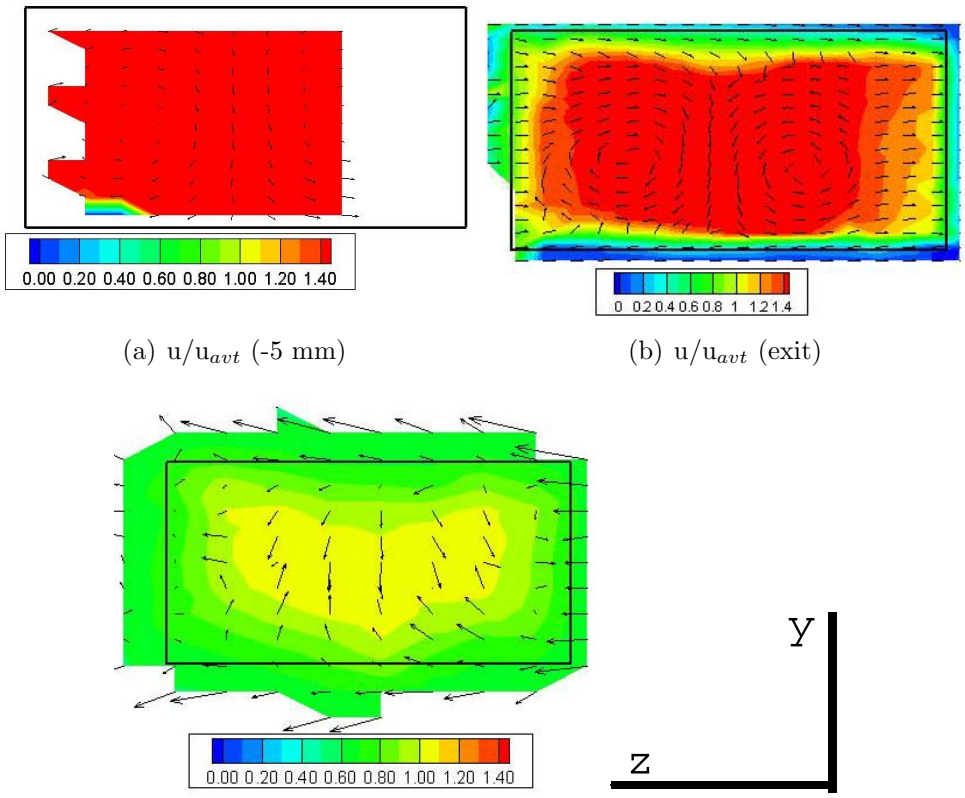

(a) u/u_{avt} (-5 mm)

(b) u/u_{avt} (exit)

(c) u/u_{avt} (2 D_h)

(d) coordinate system

Figure 19. Mean normalized streamwise velocity component for the horizontal duct and the progression from x/D_h = -0.5, 0.5 and 2.0

or four vortices typically correspond to the flow curvature for serpentine ducts for a Dean number of 8000.[16]

The LDV measurements of the streamwise velocity, u-component, exhibit the expected shift towards the outside of the second turn of the horizontal duct as can be seen in Figures 19(a)-(c). The shift in velocity is the same behavior found in the hotwire measurements. This concurs with the measurements of Ferdman, Otugen and Kim taken at a Re=2.4e^4 for the jet.[78] The higher streamwise velocity with a u/u_{avt}=1.4 along the top and center of the duct is similar to that observed in the hotwire measurements at the x/D_h=0.5. The hotwire measured a slightly higher velocity in the center, u/u_{avt}=1.3 rather than the 1.1 found with the LDV. The velocity profile holds through the progression, becoming more distorted with spreading, jet

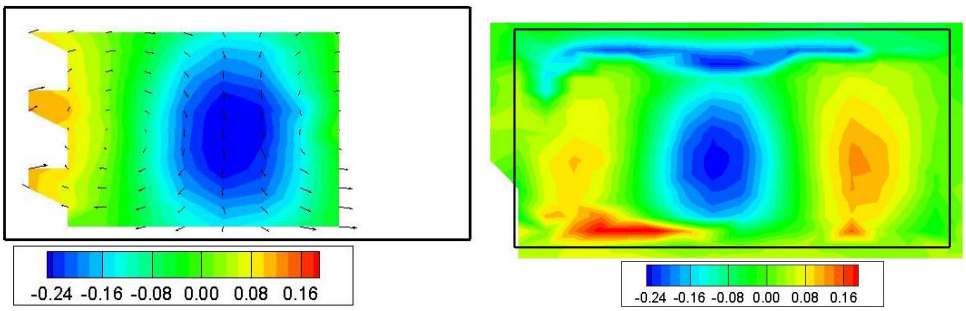

(a) v/u_{avt} (-5 mm) (b) v/u_{avt} (exit)

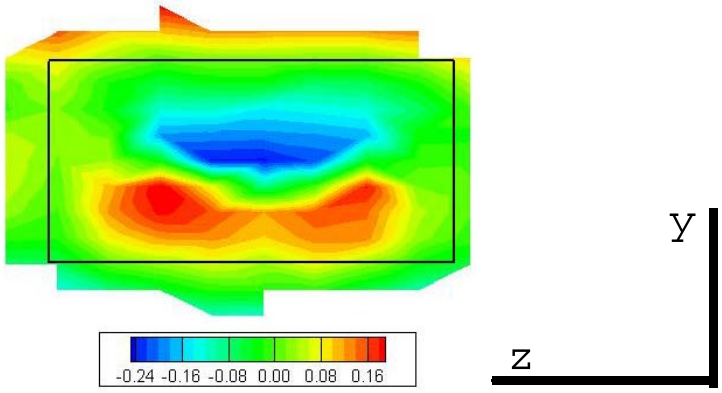

(c) v/u_{avt} (2 D_h) (d) coordinate system

Figure 20. Mean normalized vertical velocity component for the horizontal duct and the progression from x/D_h=-0.5, 0.5, 2.0.

shearing and mixing. As noticeable from the secondary flow vectors, shown in Figure 19(b), a single strong pair of counter-rotating vortices formed for this geometry. The existence of the vortex pair generates the downward trend in the mean core behavior. The upstream position, just inside of the duct exit x/D_h=-0.5, exhibits the same strong secondary flow seen at the exit location. Even with the limited data due to beam access, the velocity profile resembles the measurements at the exit. This secondary flow motion was weakened by the two hydraulic diameters downstream position. By x/D_h=2.0, shown in Figure 19(c), the flow structure's breakdown follows with jet theory in the dispersion of the streamwise velocity due to mixing.[80],[42] The outer jet region has a velocity difference of 0.2u/u_{avt} compared to the 0.6u/u_{avt} seen at the exit.

The values for the v and w-components, which led to the vector overlay in Figure 19, is explored in greater detail in Figure 20 and Figure 21. The v-component, given in Figure 20, displayed the flow in the interior and exit location descending in the center region and rising near the wall to form the circulation for the two vortices. In both the x/D_h=-0.5 and 0.5 the downward velocity is at the maximum of -0.24u_{avt}. The upward velocity is slightly weaker in comparison at 0.13u_{avt}. The magnitudes match at x/D_h=2, the shear layer influence the flow and no longer has clear counter-rotating vortices. The vertical component (v) collapsed into one region. The w-component of the velocity, shown in Figure 21, has four distinct regions delineating the actions of the flow. The direction of the flow for the w-component coincides with the directions required for the vortex pattern in Figure 19. The w-component has similar magnitudes for the minima and maxima, -0.25u_{avt} and 0.13u_{avt}. The w-component deteriorated by the x/D_h=2 location. The spanwise (w) component continues to show the jet evolution from the mixing. The location and direction of the local velocities for the v and w-components support the vector representation of the secondary flow.

The fluctuating components for the streamwise velocity is shown in Figure 22 for the u'-component. The same progression of x/D_h=-0.5, 0.5 and 2.0 is shown in these figures. The fluctuations demonstrate the concentration of the energy and where changes occur. The streamwise fluctuation (u') in Figure 22 agree with that seen in the hotwire results. The maximum fluctuation appears at the bottom center of the duct in both measurements at a value of 0.20u_{avt}. More features emerge in the interior of the LDV in the minimum velocity shown at the exit location. The shearing is more intense over the entire boundary of the LDV jet measurements. The x/D_h location for the LDV in Figure 22(c) grew since the exit location. The growth of the boundary layer fluctuations also occurred in the hotwire results for the u'-component. The fluctuations appear consistent with the values in the core region and minimum observed at the exit. Both results display that the interior core of the jet has less streamwise turbulent energy content, the mixing with the shear layer gradually affected this at the 2 D_h point downstream.

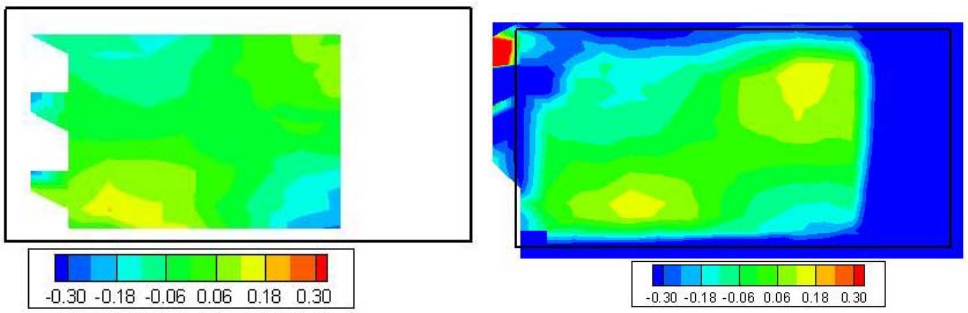

(a) w/u_{avt} (-5 mm) (b) w/u_{avt} (exit)

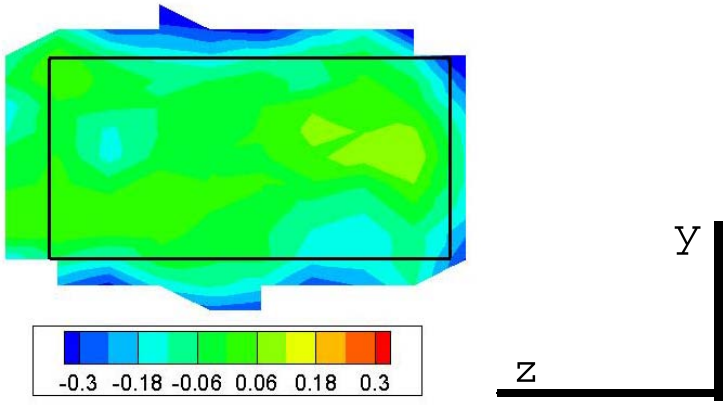

(c) w/u_{avt} (2 D_h) (d) coordinate system

Figure 21. Mean spanwise velocity component for the horizontal duct and the progression from x/D_h=-0.5, 0.5, 2.0.

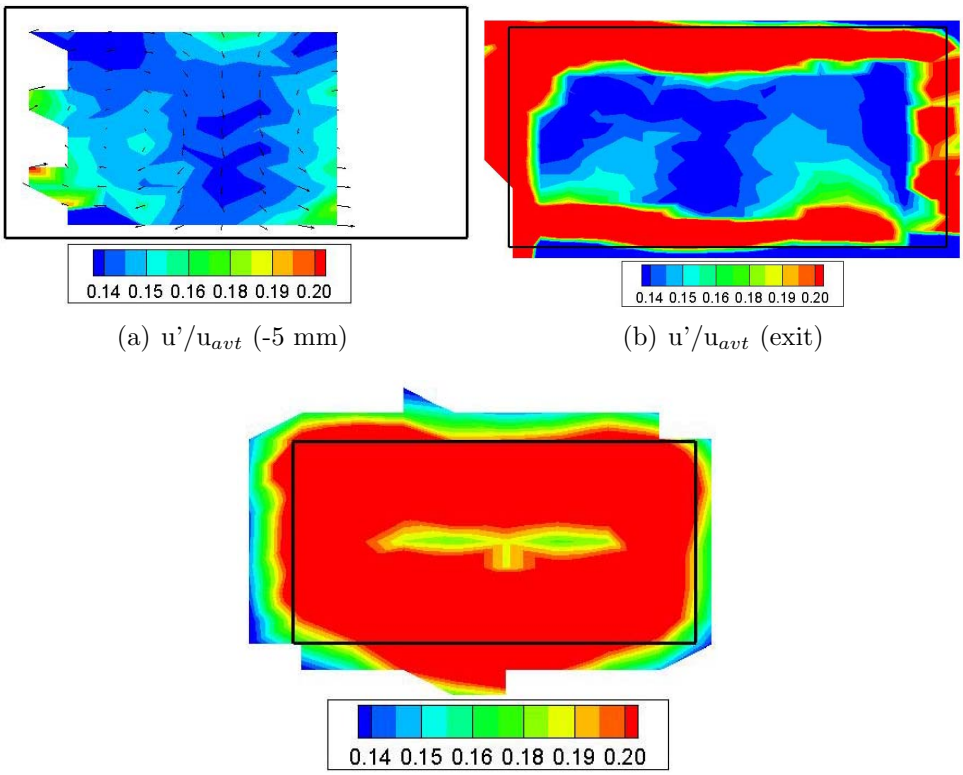

(a) u'/u_{avt} (-5 mm)

(b) u'/u_{avt} (exit)

(c) u'/u_{avt} (2 D_h)

Figure 22. Variation of the normalized streamwise velocity component for the horizontal duct and the progression from x/D_h=-0.5, 0.5, 2.0 for u'.

The LDV system resolved the v-component fluctuations occurring in the horizontal duct. The interior and exit plane in Figure 23(a) and (b) has two distinct high fluctuation cores in the center of the jet. This behavior is different from the u'-component results. The v'-component at x=2D_h displays this growth of the turbulent fluctuations in the shear layer as well. The core fluctuations are stronger than the shearing layer with a value of 0.180u_{avt} compared to around 0.13u_{avt} at the exit. The interior fluctuations at the cores were higher with a value of 0.19u_{avt}. These distinctive cores vanished or migrated outside the jet measurement region by x/D_h=2.0. The center of the measurement region has single maximum and minimum replacing the two localized higher fluctuation regions.

The results for the w'-component of the turbulent fluctuations is shown in Figure 24(a) for the interior location, (b) for the exit, and (c) for the x/D_h=2 location. The range of the measured value of the w'-component is approximately twice as large as the u' and v' fluctuations. The w' measurement provided an indication of the LDV limitation in obtaining the w-component of the velocity. The magnitudes should be closer in range.[83] The w'-component displays, predominantly, a preference in energy in the shear layer. That is the conclusive data for the horizontal duct. The w-component, due to probe volume limitation, is not quantitative, when combined with the v-component suffices to determine the secondary flow behavior. Greater variation at the edges of the measurement region should be present. The free shear layer affects the velocity at the edge of the jet. The interior of the duct remains uniform, nothing increases the fluctuating components.

For completeness the u'u' for the horizontal duct is shown in Figure 25, the v'v' in Figure 26 and the w'w' in Figure 27. The same higher energy regions evident in the u', v' and w' occur in the u'u', v'v', and w'w' Reynolds stresses. The u'u'-component, shown in Figure 25(a) and (b), has a lower fluctuating region within the core for the interior of the duct and exit location. The same resemblance to the v'-component holds true for the v'v'-component given in Figure 26. The two localized higher fluctuating regions are evident in the interior and exit location, shown in

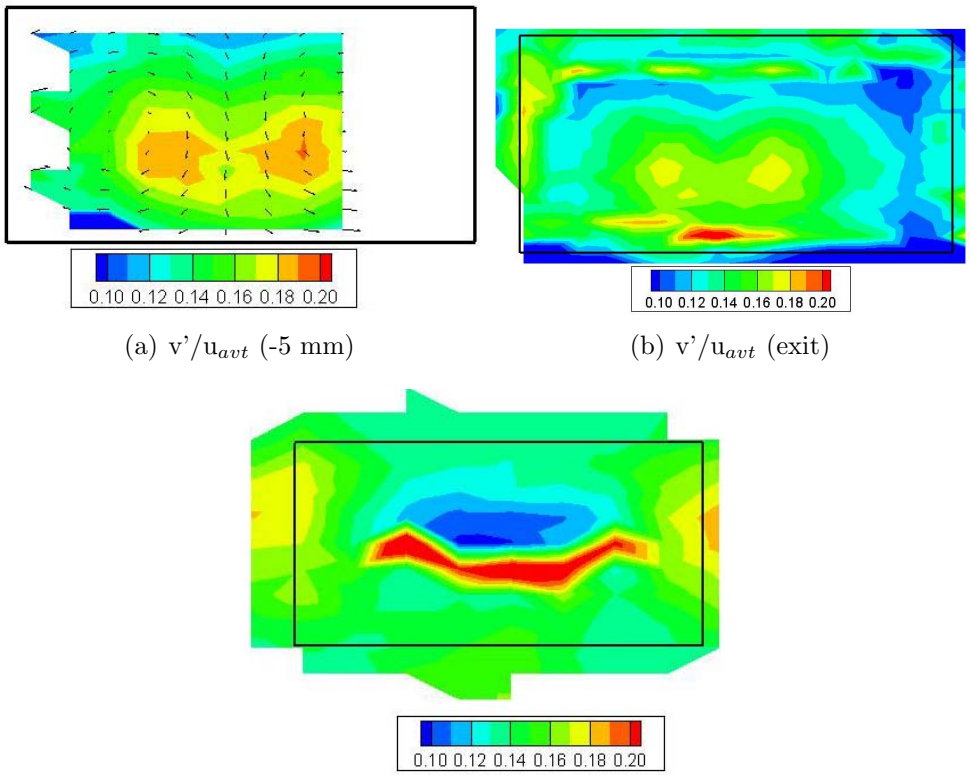

(a) v'/u_{avt} (-5 mm)

(b) v'/u_{avt} (exit)

(c) v'/u_{avt} (2 D_h)

Figure 23. Variation of the vertical velocity components for the horizontal duct and the progression from x/D_h= -0.5, 0.5, 2.0 for v'.

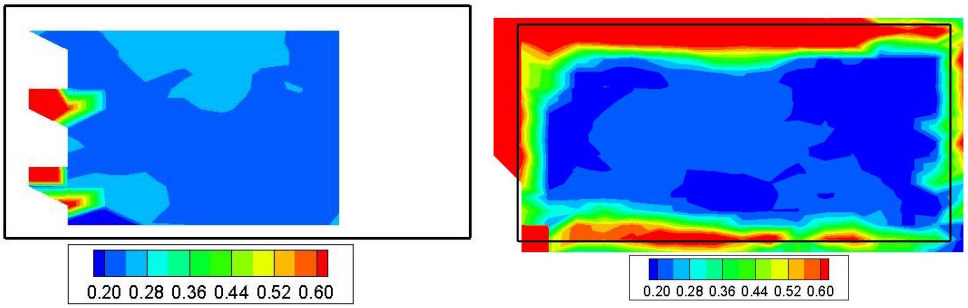

(a) w'/u_{avt} (-5 mm) (b) w'/u_{avt} (exit)

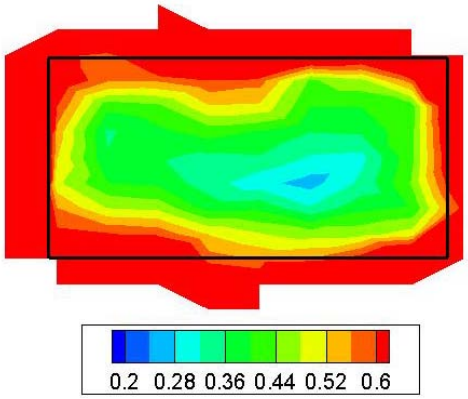

(c) w'/u_{avt} (2 D_h)

Figure 24. Variation of the spanwise velocity components for the horizontal duct and the progression from x/D_h=-0.5, 0.5, 2.0 for the fluctuating turbulent w'-component.

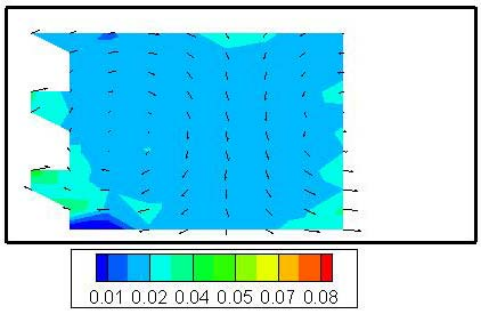

(a) u'u'/u^2_{avt} (-5 mm)

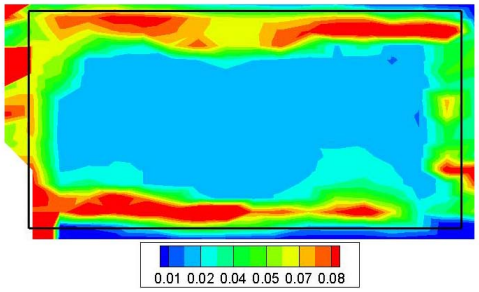

(b) u'u'/u^2_{avt} (exit)

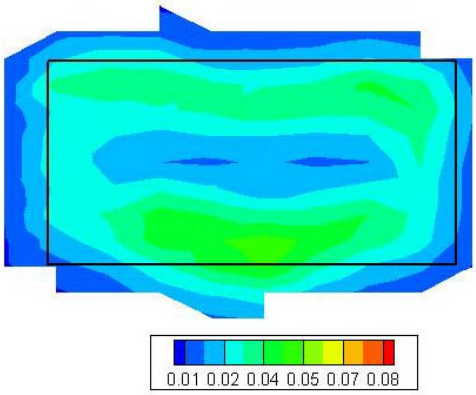

(c) u'u'/u^2_{avt} (2 D_h)

Figure 25. The Reynolds stress for the horizontal duct and the progression of the components from x/D_h for u'u'.

Figure 26(a) and (b). The w'w'-component, shown in Figure 27, has the same types of features visible in the w'-component. The w'w'-component is an order of magnitude larger than the u'u' and v'v'-components. The higher velocity fluctuations remain in the shear layer of the jet for all three components in agreement with the results for the fluctuating components.

The flow features between the fluctuating and turbulent kinetic energy relate, as given in Equation 3 and 6, therefore only one is necessary. The cross components of the Reynolds stresses or the shear stresses are a different matter. The interactions of the flow between the two fluctuating components lend insight into the flow dynamics and the transfer of energy. Some of the features loose distinctive characteristics due to the

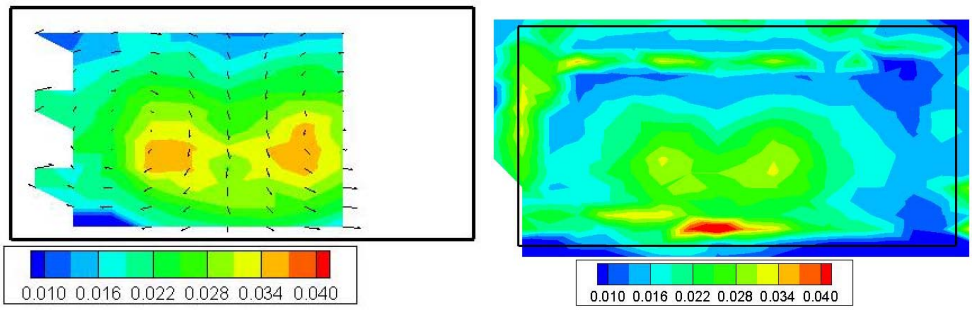

(a) v'v'/u^2_{avt} (-5 mm) (b) v'v'/u^2_{avt} (exit)

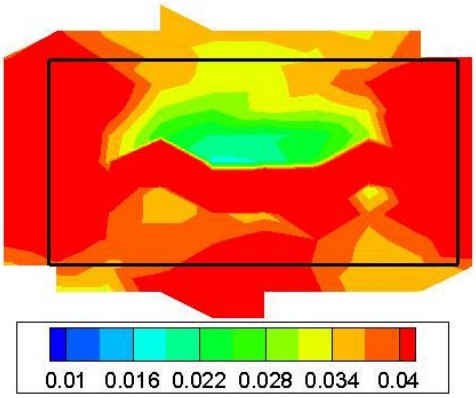

(c) v'v'/u^2_{avt} (2 D_h)

Figure 26. The Reynolds stress component for the horizontal duct in the progression of the components from x/D_h=-0.5, 0.5, 2.0 for v'v'.

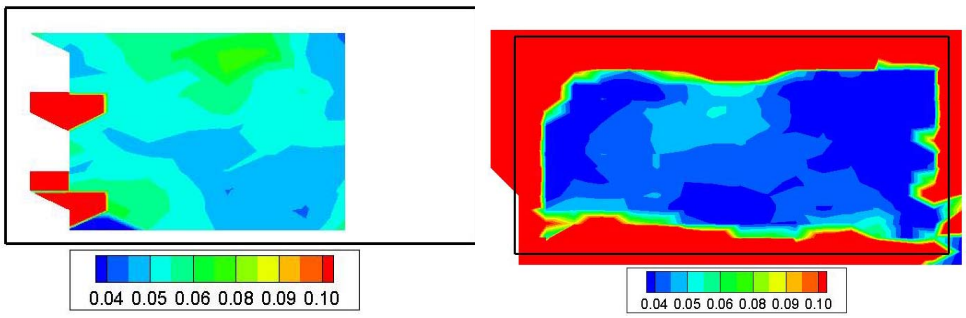

(a) w'w'/u^2_{avt} (-5 mm) (b) w'w'/u^2_{avt} (exit)

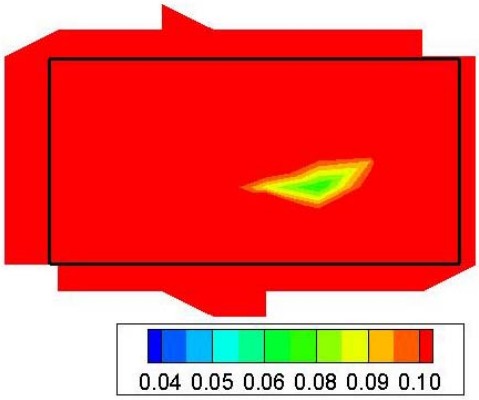

(c) w'w'/u^2_{avt} (2 D_h)

Figure 27. The Reynolds stress for the horizontal duct and the progression of the components from x/D_h=-0.5, 0.5, 2.0 for w'w'.

measurement limitations of measuring w'. The u'v'-component of the shear stresses is more accurate and considerable information was gleaned from this component.

The results for the shear stresses for the u'v'-component is shown in Figure 28. The interior location of the u'v'-component in Figure 28(a) has lower shear stresses along the bottom and wall locations of the duct. A slightly larger region of turbulent energy appears in the location where the secondary flow falls in the center. The magnitude range is small in the interior of the duct since the mixing of the jet occurs downstream of this location. The minimum is $0.012u^2_{avt}$ and the maximum $0.008u^2_{avt}$. These minima and maxima extend far beyond these values at the exit, as given in Figure 28(b). At the exit, the shear layer dominated the range, a maximum in the positive y-direction and a minimum in the negative y-direction. Fluctuations in the

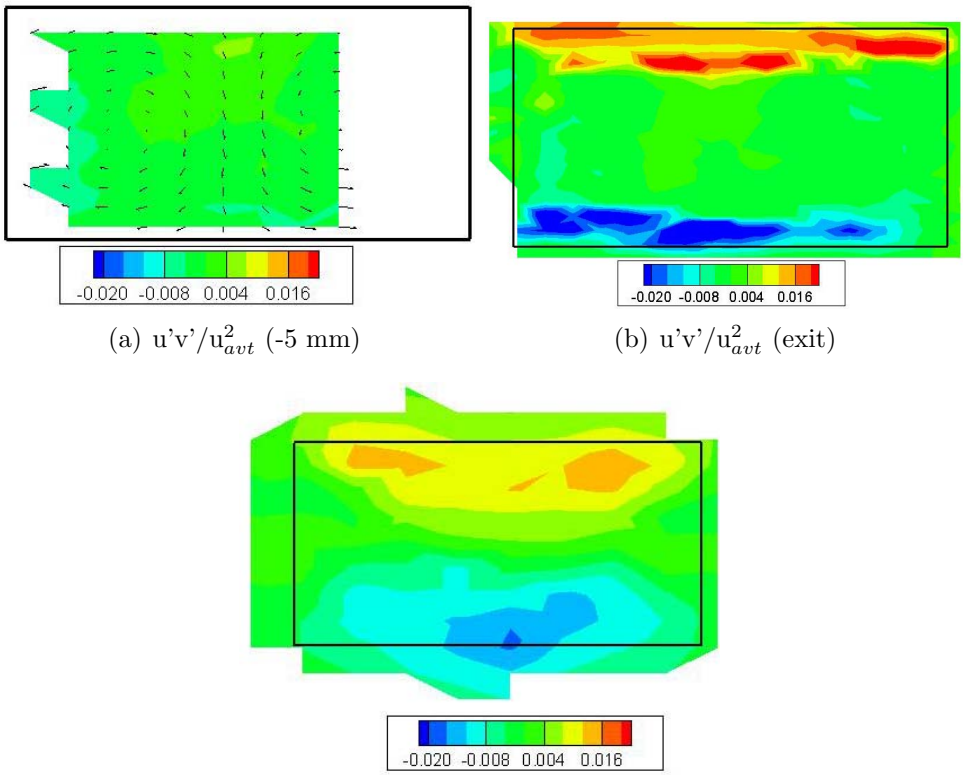

(a) u'v'/u^2_{avt} (-5 mm) (b) u'v'/u^2_{avt} (exit)

(c) u'v'/u^2_{avt} (2 D_h)

Figure 28. The Reynolds stress for the horizontal duct and the progression of the components from x/D_h=-0.5, 0.5, 2.0 for u'v'.

vertical component are small on each side of the jet causing the values of u'v' to be lower there. The direction and magnitudes correspond with jet flows examined in other experiments.[83] The shear stresses remain consistent within expectations at x/D_h=2.0, shown in Figure 28(c), with the positive stresses at the top of the duct and the negative stresses at the bottom. Mixing distributed the energy content over a broader area and lessened the magnitudes, which is typical for a jet. The local maximum is slightly asymmetric in the bottom of the duct with two peaks forming in the upper half. The distributions are typically evenly distributed over the region.[83]

Despite the difficulty in measuring w'-component, the u'w'-component lent some insight into the flow. Some of the same characteristics as the u'v'-component show, where u' is positive and w' is positive has higher shear stresses. Where only one is

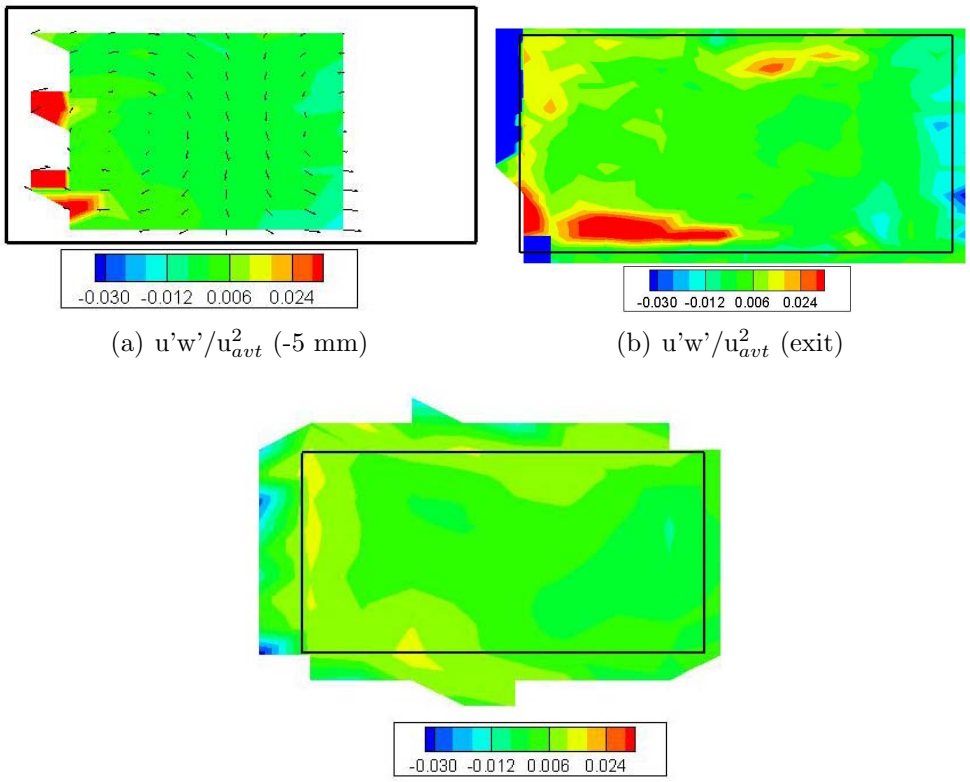

(a) u'w'/u^2_{avt} (-5 mm)

(b) u'w'/u^2_{avt} (exit)

(c) u'w'/u^2_{avt} (2 D_h)

Figure 29. The Reynolds stress for the horizontal duct and the progression of the components from x/D_h=-0.5, 0.5, 2.0 for u'w'.

negative, there is a minimum. The left hand side of all locations in Figure 29 has a maximum of 0.024u^2_{avt} and on the right a minimum of -0.020u^2_{avt}. These values are larger than the measured u'v'-component due to the difficulty in capturing the w-component. The downstream location in Figure 29(c) displays that mixing spread the shear stresses over the measurement region and reduced the peak values. The largest magnitudes for the u'v' occur on the bottom and top of the jet, whereas the largest magnitudes for the u'w' occur on each side of the jet. The v'w'-component is the least reliable of the measurements, the combination of two lower velocities makes measurements uncertain, as shown in Figure 30. This component is the most difficult to obtain and is rarely reported. The magnitude is smaller than the u'v' and u'w'-components by a full order of magnitude. The shear stresses follow with the vortex cores and the interaction between the vortices and the shear layer of the jet, as shown

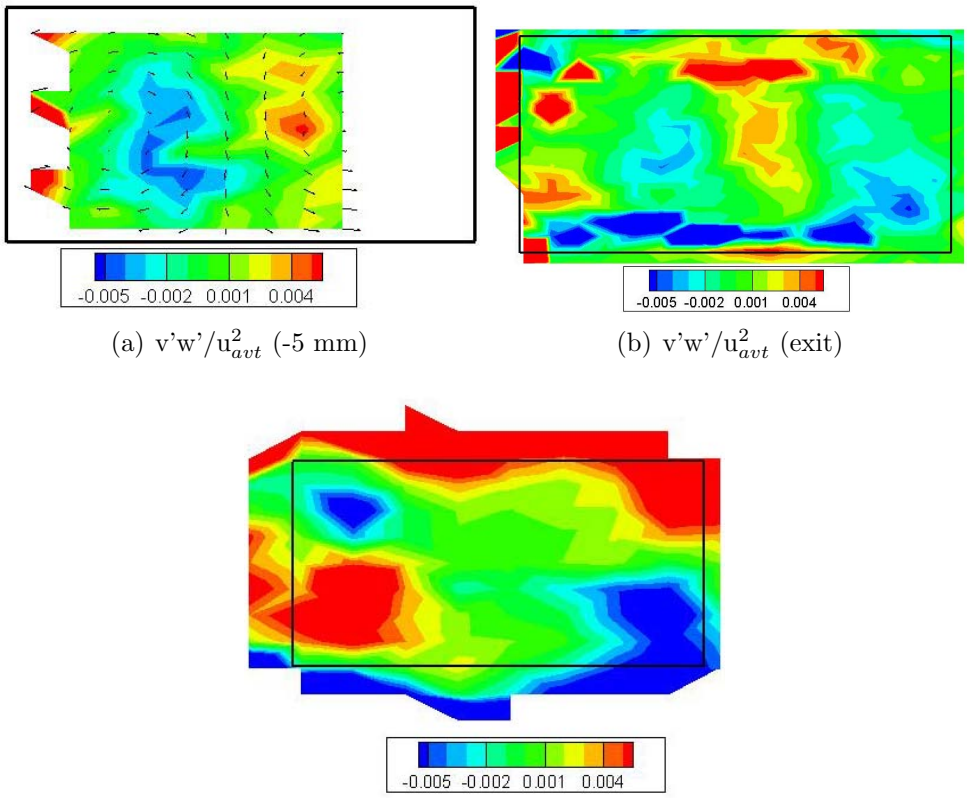

(a) v'w'/u^2_{avt} (-5 mm)

(b) v'w'/u^2_{avt} (exit)

(c) v'w'/u^2_{avt} (2 D_h)

Figure 30. The Reynolds stress for the horizontal duct and the progression of the components from x/D_h=-0.5, 0.5, 2.0 for v'w'.

in Figure 30(a) and (b). Features deteriorate with the mixing of the flow, as shown in Figure 30(c), showing jet mixing rather than the flow features observed at the interior and exit locations. The low shear stress region is not apparent at this location.

The understanding of the flow behavior in the horizontal duct with the two bends is enhanced by measurements of the secondary velocities and Reynolds stresses. The horizontal duct has two dominant secondary flow features, analogous with two vortices. The flow pattern expected for a single 90 degree bend is opposite to that presented in the two bends in that the secondary flow rotates contrary to the bend direction in Berger.[16],[102] The mean u and v-components delineated the flow and provided comprehensive results. The w-component proved difficult to obtain, but did provide overall trends and quantitative results. The results involving w'-components

of the Reynolds stresses were much more uncertain, demonstrating the inaccuracy clearly. The cross components show the shearing or mixing locations from the presence of the vortices and the boundary of the jet.

4.3 LDV Examination of the Vertical Duct

The results of the LDV investigation for the vertical duct are shown in Figure 31 for the mean velocity components, Figure 32 for the turbulent kinetic energy components, and Figure 33 for the shear stresses. The results in the interior of the vertical duct are harder to obtain due to the beam reflection through the Plexiglas and the less organized nature of the secondary velocities. The jet portion presented no difficulty in terms of the measurements with LDV.

The mean velocity in the jet for the vertical nozzle is given in Figure 31. The shift of the peak streamwise velocity towards the outside of the second bend occurs at the exit, as shown in Figure 31(a). An unexpected asymmetry formed in the w-component from the right and left side of the duct. This led to two additional repeated measurements of the velocity in this full plane, and all cases demonstrated the asymmetry. A large lower velocity region forms in the lower portion of the jet shown in Figure 31(a) and (b). The streamwise velocity has the same magnitude as that of the horizontal nozzle at $1.4u_{avt}$. The velocity deficit is the region of less than $1.0u_{avt}$. This low velocity region translates to the downstream location, since mixing deteriorates the size of the core in Figure 31(b). The weaker organization and strength of the secondary flow allowed the streamwise velocity to retain some of its peak value to this location. The horizontal duct had deteriorated to $1.2u_{avt}$ by this location for the maximum. The weaker secondary flows a evaluate better from the components that created the vector overlays.

The v-component at the exit is given in Figure 31(c), while shows two rising velocity regions indicated by a mild descending region in the middle formed in the lower half. For the top only one rising and one falling region was measured. A counter-rotating vortex pair in the upper half requires a second rising region in the

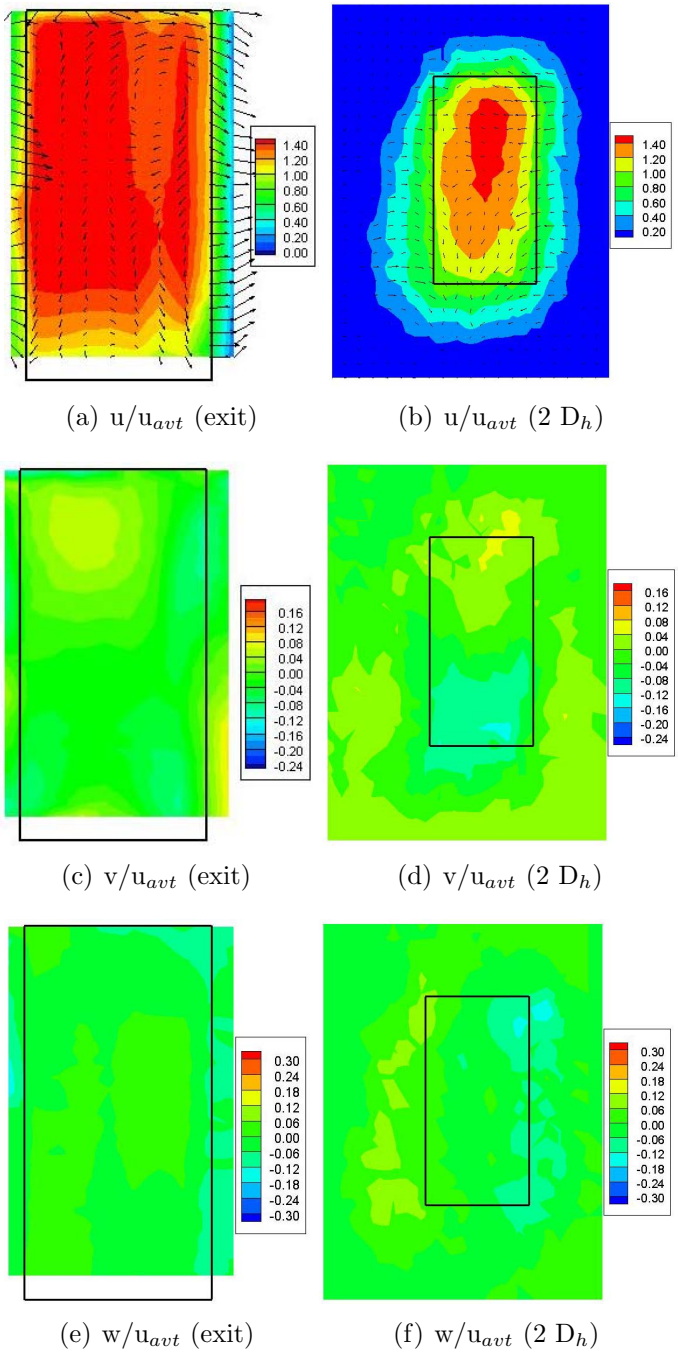

(a) u/u_{avt} (exit) (b) u/u_{avt} (2 D_h)

(c) v/u_{avt} (exit) (d) v/u_{avt} (2 D_h)

(e) w/u_{avt} (exit) (f) w/u_{avt} (2 D_h)

Figure 31. Mean velocity components for the vertical nozzle for x/D_h=0.5 and 2.0.

upper half which is not indicated in the measurements. The v-component is half the magnitude of that observed in the horizontal nozzle at -0.12 and $0.08u_{avt}$ making the measurements more difficult to resolve. The v-component demonstrates that the secondary structure is not the simple pattern found in the horizontal serpentine duct. The v-component interacts with the shear regions greatly, as shown in Figure 31(d). The shear layer dominates the flow altering the secondary structure further. The shear layer merging with the core flow structures obscures all distinguishable features. The maximum dominates the upper portion of the nozzle while the minimum dominates the lower portion at this location.

The w-component of the velocity is given in Figures 31(e) and (f). The w-component has half the strength of the horizontal nozzle with the minimum and maximum at -0.12 and $0.18u_{avt}$. The flow appears to be positive in the positive z-direction and negative in the negative z-direction. This continues holds for the x/D_h=2.0 location with some growth caused by the shear layer. The velocity measurements distinguish no flow patterns without combining with the v-component in vector representation. The direction of the flow was correct, but the scale and magnitude prevented attributing any behavior to the w-component for the vertical duct. This inhibited determination of pockets of flow changes, particularly at the jet exit. Mixing overtook the small velocity features, the spanwise direction easier to overtake due to the thinner profile and higher energy working on the longer dimension of the nozzle.[92],[79] The horizontal nozzle maintained stronger organization of the secondary velocities in comparison.

The fluctuating velocities are presented in Figure 32 for the vertical nozzle. The lowest fluctuations in the streamwise velocity (u') are found within the core region, as shown in Figure 32(a) and (b). All of the large variations occur within the mixing layer of the jet and the lower velocity region. The aspect ratio differentiated the interior structure and development of the two ducts, due to the distribution of the centripetal forces. Lower velocity fluctuations occurred in the interior of the jet for the u', and w'-components than the v'-component. The peak fluctuating component magnitudes

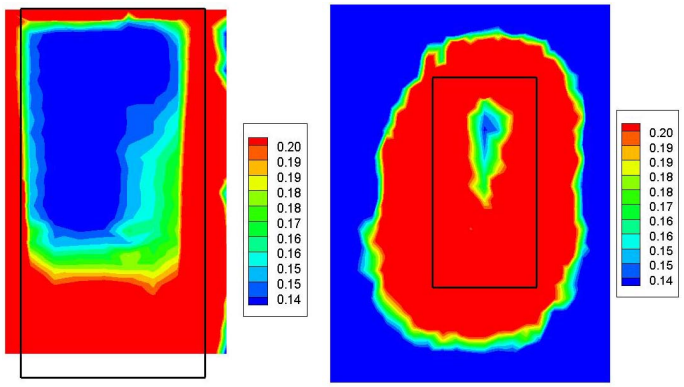

(a) u'/u_{avt} (exit) (b) u'/u_{avt} (2 D_h)

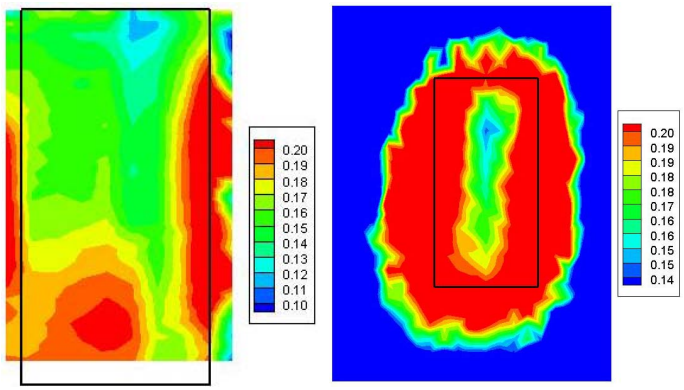

(c) v'/u_{avt} (exit) (d) v'/u_{avt} (2 D_h)

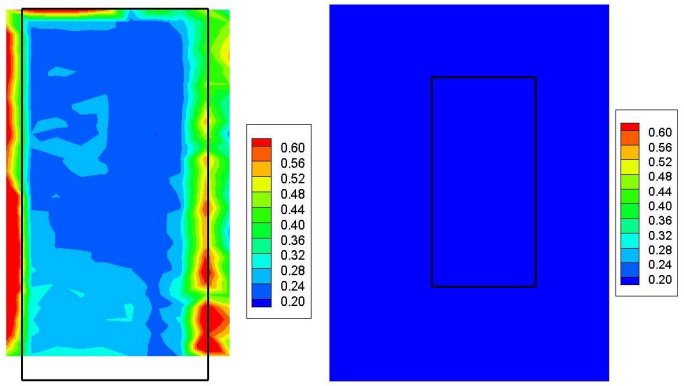

(e) w/u_{avt} (exit) (f) w'/u_{avt} (2 D_h)

Figure 32. Variation of the fluctuating velocity components for the vertical nozzle at x/D_h=0.5 and 2.0.

are similar to those in the horizontal nozzle. The largest fluctuations occur within the shearing layer of the jet and in the streamwise velocity deficit region.

The v'-component, given in Figures 32(c) and (d), has large shearing regions along the sides of the duct and the bottom of the serpentine duct. The shear layer dominates most of the jet measurements for the v'-component at the downstream location. The w'-component for the vertical duct generally agrees with the horizontal nozzle having lower level fluctuations in the core with greater intensity at the jet boundary. This component appears to redistribute quickly with downstream location, as shown in Figure 32(f). The magnitude of the w'-component is larger than that of the other two components, again displaying the lack of measurement fidelity for this component. The lack of a dominant pair of streamwise vortices lead to asymmetry in the shear layer, as observed in Figure 32. A distinct flow pattern is not discernable from this analysis. The u'u', v'v', and w'w' present the same information as the RMS values shown in Equation 3 and Equation 6.

The final examination for the LDV measurements are the cross components of the Reynolds stress for the vertical duct. The cross components of the Reynolds stresses, or the Reynolds shear stresses, are given in Figure 33 for the u'v', u'w' and v'w'-components. The exit displays that the u'v'-component of the Reynolds stress, shown in Figure 33(a) and (b), has the expected shear layer phenomena at the top and bottom of the jet. As with the horizontal duct, this result is anticipated from literature. The minimum and maximum region remain of the same magnitude, -0.02 to $0.02u_{avt}^2$ respectively, in progressing to x/D_h=2.0. An interesting feature is the pair of local maxima near the center of the y-plane. The presence of the local maximums suggest interaction from the upper and lower halves of the duct. This signifies that a weak complicated flow structure formed in the vertical duct.

The other components are only useful for qualitative observations due to the difficulty in obtaining the w-component of the velocity. The u'w'-component has some similarity to the horizontal duct. The values are positive in the positive z-direction and

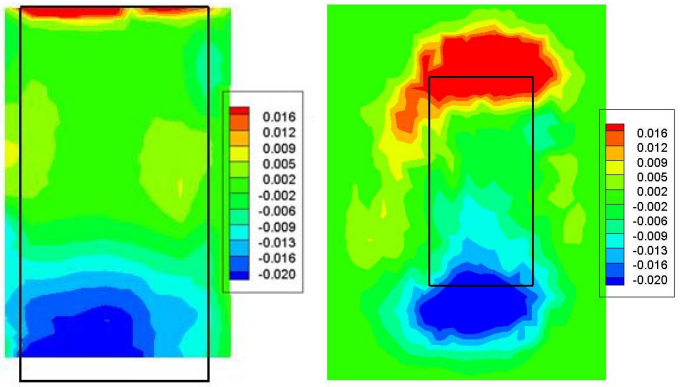

(a) u'v'/u^2_{avt} (exit) (b) u'v'/u^2_{avt} (2 D_h)

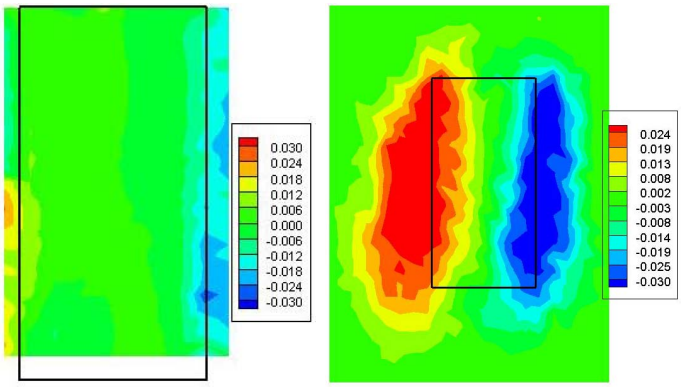

(c) u'w'/u^2_{avt} (exit) (d) u'w'/u^2_{avt} (2 D_h)

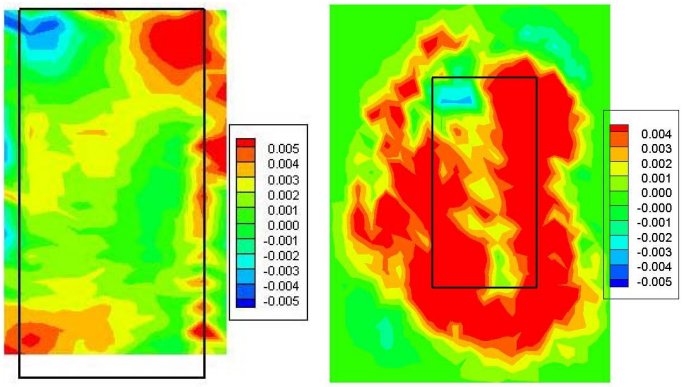

(e) v'w'/u^2_{avt} (exit) (f) v'w'/u^2_{avt} (2 D_h)

Figure 33. The Reynolds stresses for the vertical nozzle at x/D_h=0.5 and 2.0.

negative in the negative z-direction following with the direction of the w-component. Magnitudes of u'w' are larger on each side of the jet than on the top and bottom. The u'w'-component is overall higher than that of the u'v', evidencing the difficulty of the measurement. The qualitative analysis of the w'-component agrees with the jet measurements obtained by others.[103] The v'w'-component is difficult to analyze especially with the weaker secondary velocities. The magnitudes of the components are a full order of magnitude smaller than those of the u'v'-component and even the u'w'-component. The shear layer dominates the x/D_h=2.0 location, flow features in the core are nearly indistinguishable. Even the cores evident in Figures 33(a) and (b) of the vortices are weaker than those in the horizontal nozzle. The boundary layer shearing shows the source of the energy measured in the jet for this aspect ratio of the serpentine duct. Unlike the horizontal duct where some features of v'w' was evident in the core region, nothing is distinguishable in the vertical duct.

The observations obtained by looking at the two serpentine nozzle configurations with the LDV system elucidated the basic behavior of the flow. Flow turning created a lower streamwise velocity region in the bottom of the duct. The peak velocities for the u'v'-component compared in magnitude and location. The maximum in the jet exiting both ducts formed at the top with the minimum at the bottom. The u'w'-component was comparable for the two duct configurations. The maximum positioned at the edge in the positive z-direction and the minimum on the side in the negative z-direction. Specific to the horizontal duct was the presence of a strong pair of streamwise vortices. The vertical duct had no clear presence of paired vortices, the weaker secondary velocities did not allow clear organization of the flow. The weaker secondary flows contributed to the rationale for the computational study. Once validated, the CFD study additionally provided information on the flow development that created the observed structures.

4.4 500,000 Cell Grid Numerical Simulation

The k-ϵ method preliminarily examined the flow. However, as pointed out by Shur, the k-ϵ model functions poorly when separation occurs.[50] The k-ϵ model is naturally dissipative, features are less distinct compared to the RSM results.[41],[40],[50] The results were poor as predicted by literature, further discussion of the k-ϵ is refrained. The RSM model evaluated the experimental results. The calculations of the shear stresses made no assumption on the isotropy of the flow and handled the changes created by the curvature. The RSM model explored two levels of grid resolution, a moderately coarse grid resolution (≈500,000 nodes) and refined grid (≈4,000,000 nodes).

The results of the moderate grid resolution for the horizontal duct are shown in Figure 34 for a first order discretization of the RSM model. The moderate grid resolution shows the streamwise velocity (u) shift towards the outside of the second bend in Figure 34(a). The v-component, shown in Figure 34(b), displays the pattern of rising at the edges and falling in the middle, consistent with a two vortex pattern. The corresponding w-component, given in Figure 34(c), completed the flow pattern establishing the secondary velocities that were seen in the LDV measurements. The velocity magnitude values are different, but the model displays basic agreement with the flow features in Figures 20-21. The streamwise velocity shift appeared in the model along with the magnitude of the velocity being $1.40u_{avt}$. The slightly lower velocity in the bottom corners of the duct agree, with close magnitudes of $0.60u_{avt}$. The v-component magnitudes were larger at $0.16u_{avt}$ compared to the LDV results of $0.13u_{avt}$. The minimum of the v-component was similar for the two results. The w-component magnitudes are larger in the experimental results, 0.24 rather than $0.07u_{avt}$. The RSM model predicted similar behavior to that observed in the experiment. The correlation of flow features at the duct exit lends confidence that examining the computational results in the interior of the serpentine duct provides understanding of the flow behavior and development.

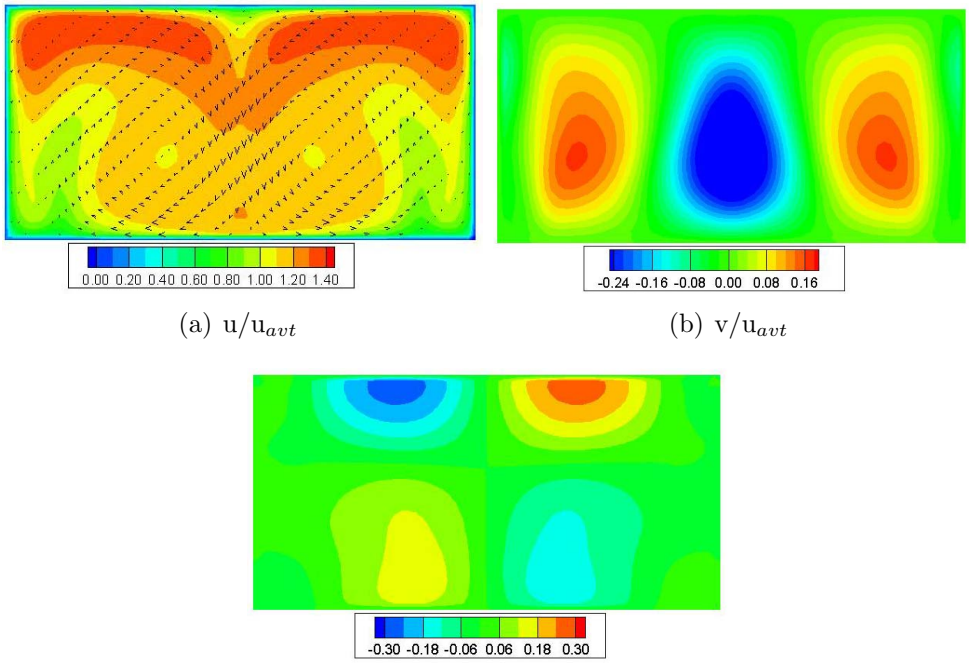

(a) u/u_{avt} (b) v/u_{avt}

(c) w/u_{avt}

Figure 34. The mean velocity components for the RSM computational study for the flow for the horizontal duct at a moderate grid resolution of 500,000 nodes.

The results from the moderate grid resolution for the vertical nozzle are given in Figure 35. The computational model predicts the shift in the streamwise flow towards the upper portion of the second bend. The magnitude of the velocity in the core is slightly lower than expected from the experiment. The results of the vector overlay in Figure 35(a) indicate two pairs of vortices with the bottom pair covering over half of the duct. The features seen in the v and w-component in Figures 35(b) and (c) indicated a dominant pair of streamwise vortices, which were not seen in the experiment. The magnitudes are slightly higher than the experiment. The secondary components for the vertical duct were weaker than those seen in the horizontal duct. The larger structure in Figure 35(b) in the lower half of the vertical duct appears in Figure 31 at the exit plane. The vortex indicated in the top half of the duct in the experiment is indistinct for this grid resolution. The vertical duct measurements had better fidelity than the horizontal duct, according to y^+=1.2 and y^+=12.39, respectively. The term y^+ is the viscous sublayer of the boundary layer. Resolution

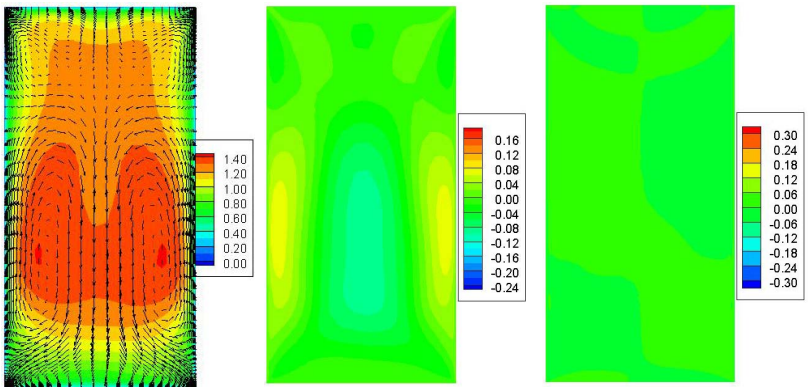

(a) u/u_{avt} (b) v/u_{avt} (c) w/u_{avt}

Figure 35. Computational study of the vertical duct using RSM to study the flow with a moderate grid resolution of 500,000 nodes.

of the sublayer as measured by y^+ indicates the computational model fidelity. The higher grid resolution ensured that the fidelity of the solution was not grid limited. The boundary layer, in particular, affects the solution.[96] The y^+ given are the maximum values observed in the ducts. These higher levels of the y^+ remained in the region of the bends. The value of y^+ in the straight sections were significantly lower, near the accepted range define what the acceptable range is.

The general flow features appeared in the coarse grid resolution of 500,000 nodal location solutions for the serpentine duct. Two circulation regions formed in the horizontal duct, matching the measured pattern in the experiment. The vertical duct displayed weaker secondary flow patterns which generally agree with experimental results. The flow shifted towards the outside of the bend in both computational results, consistent with expected curved flow behavior. The velocity magnitudes matched reasonably well, although low in some regions. The higher order grid resolution and discretization elucidates whether this is a grid inconsistency or a model limitation.

4.5 4,000,000 Cell Grid for the Horizontal Nozzle

To improve the resolution of flow features the serpentine ducts were re-gridded to a higher resolution, nearly four million nodes. A higher order discretization increased

the validity of the solution. Also, the differencing scheme changed from a first order to a third order. The grid resolution was necessary to confirm that the computational results were grid independent and capturing the relevant flow features. The predicted flow compared more favorably to the experimental results, particularly for the vertical nozzle.

The higher order discretization and grid resolution results for the horizontal nozzle are shown in Figure 36. Not all of streamwise profile is uniform, as observed in the experiment. Two high velocity regions appear in the upper part of the duct exit. The higher resolution result is better than the 500k node result. The regions of higher velocity cover more area than the 500k node case. The flow is more uniform in the upper region of the duct as given by Figure 36(a). A region of high velocity also formed in the lower center of the duct compares to the LDV results and this suggests improvement over the coarse grid results. The lower velocity in the bottom corners match with the experimental results. A strong secondary flow manifests in both the experiment and this computational results. Initiation of the free shear layer additionally obscured these structures. The v-component, given in Figure 36(b), has regions consistent with a two vortex system with the w-component, shown in Figure 36(c), completing the flow pattern for rotation of the flow. The magnitude of the minimum and maximum correspond better than the result of the lower grid resolution. The minimums are both -0.24u_{avt} in the four million grid and the LDV. The maximums slightly different, 0.12u_{avt} experimentally compared to 0.10u_{avt} for the four million node grid. There was a small difference in the maximum, 0.16u_{avt} for the 500k grid solution. The minimum and maximum for the w-component compared at values of -0.12u_{avt} and 0.12u_{avt} in the experiment to the computational results of -0.14u_{avt} and 0.14u_{avt}.

The fluctuating components for the horizontal nozzle are shown in Figure 37. The u'u'-component is highest in the region where large gradients formed in the streamwise velocity, following the circulation regions. The same holds for v'v' and w'w', shown in Figure 37(b) and (c) for the energy content. The v'v' portion of the

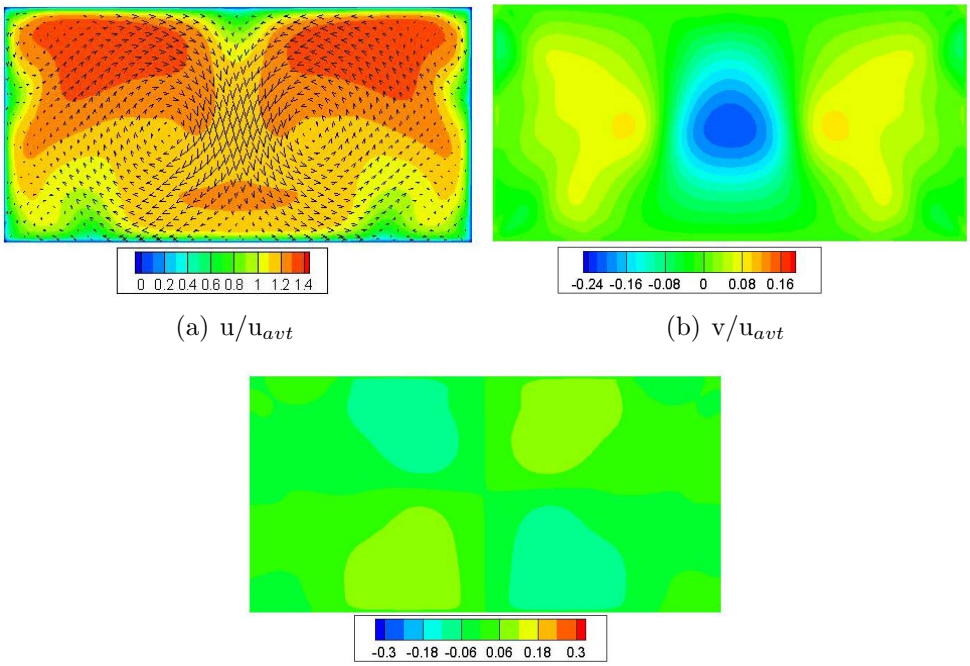

(a) u/u_{avt} (b) v/u_{avt}

(c) w/u_{avt}

Figure 36. High resolution (4 million nodes) and third order discretization of the horizontal duct using RSM for the mean velocities.

turbulent kinetic energy indicates greater turbulence between the two discrete vortices. The w'w'-component has no distinct attributes on this scale, which corresponds to the scale for the LDV data. The streamwise turbulent kinetic energy component is the most energetic of the three components.

The same lower energy region observed in Figure 37(a) for u'u' evidences a good comparison to the LDV data in Figure 25(a). The finer features from the computational results near the walls were features that the mixing layer obscured. The interior for the LDV study has levels from 0.015-0.08u^2_{avt}, while the computational study has levels from 0.01-0.025u^2_{avt}. The v'v'-component opposes in comparison for the minima and maxima as shown also in the highs and lows exhibited by Figure 37(b). The v'v'-component shows some similarities in the two peaks observed in close proximity in the lower half of the duct for both Figure 37(b) and Figure 23(b). The magnitude is 0.016u^2_{avt} for the higher grid resolution computational study and 0.034u^2_{avt} for the measurement. The matching features were encouraging that the

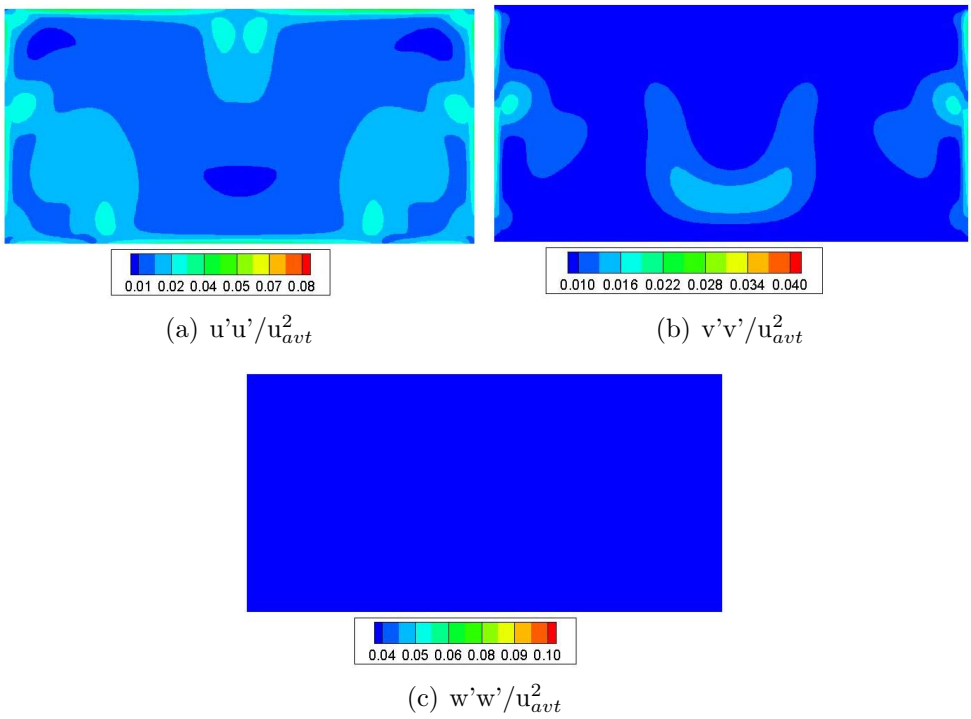

(a) u'u'/u^2_{avt} (b) v'v'/u^2_{avt}

(c) w'w'/u^2_{avt}

Figure 37. The velocity fluctuations predicted by RSM for the high resolution grid and third order discretization of 4M nodes for the horizontal nozzle.

two results were not completely different in this difficult to obtain data set. The w fluctuations or w'w' Reynolds stresses in this data display range were uniform, as shown in Figure 37(c). This is similar the LDV, shown in Figure 24(b). The scale set by the experimental results obscures the flow features. The range for the experiment was 0.05-0.06u^2_{avt} compared to 0.04u^2_{avt} or less for the computational study. The two are on the same order of magnitude, the best results that may be expected with the limitations on the w-component measurements.

The behavior of the cross components of the Reynolds stresses is shown in Figure 38, for the horizontal nozzle. The u'v'-component in Figure 38(a) yields lower values that the u'u' and v'v'-components, 0.016u^2_{avt} compared to the range of 0.08 or 0.04 u^2_{avt} maximums. A maximum extends over the positive y-direction of most of the top half of the duct. The mild negative region extends up into the cores of the vortices for the u'v'-component. The u'w' and v'w' Reynolds stresses are smaller in magnitude to the turbulent kinetic energy components, shown in Figures 38(b) and

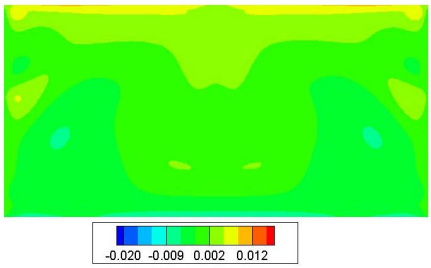

(a) u'v'/u^2_{avt}

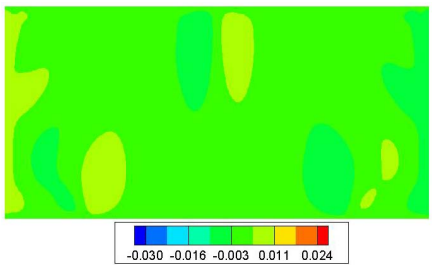

(b) u'w'/u^2_{avt}

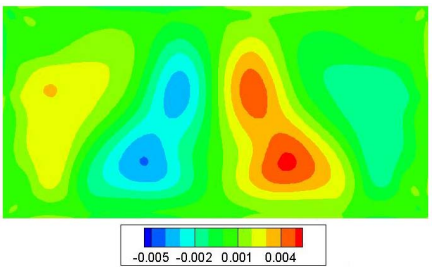

(c) v'w'/u^2_{avt}

Figure 38. The Reynolds stresses for the horizontal duct with the RSM computational model for the third order discretization of 4M nodes.

(c). The range for the u'w'-component is $\pm 0.009 u^2_{avt}$ and the v'w'-component ranged from $\pm 0.004 u^2_{avt}$. The simulation predicted the components to have similar ranges and magnitude to the measurements. The u'w'-component paired regions of negative and positive energy in the regions of interaction for the discrete vortices. The v'w'-component had two opposing regions, supporting the presence of two vortices. These regions of higher energy content are locations of increased shear. Comparison to the LDV proved difficult for these components, however, the same features appear to be shown in Figures 28-30. The intensity of the shear layer makes these features difficult to discern. The higher energy at the top of the duct and negative shearing in the bottom correlates with the LDV data for the u'v'-component in Figure 28(a) and (b). The LDV data for the u'w'-component is indistinct, conclusions impossible to make with the shear layer. The v'w'-component of the LDV measurements in Figure 30 appeared to agree with two central minima and maxima, as predicted in the CFD in Figure 38(c). The adjoining minima and maxima magnitudes indicated by the LDV are slightly larger by $0.001 u_{avt}$.

The higher order grid resolution resolved finer features than presented in the coarse grid or the LDV investigation. The magnitude and features of the finer grid resolution resolved more features and provided better agreement with the experiment. The coarse grid was not sufficiently resolved. Two strong vortical structures formed with smaller corner vortices. A greater area of higher velocity in the streamwise direction corresponded with the experimental study. The reasonable level of correlation warrants investigation into the interior region of the duct using the CFD results. In particular, it explains the opposite flow direction of the vortices compared to a single 90° bend. Examination of the vertical duct higher order simulation and grid resolution confirms the usefulness of interior investigation of flow development.

4.6 4,000,000 Cell Grid for the Vertical Duct

A similar higher resolution grid of 4 million nodes yielded results for the vertical serpentine duct. The mean velocity profiles at the duct exit are given in Figure 39. As in the case of the horizontal nozzle, the computational study predicted finer secondary motions than resolved in the experiment. The peak streamwise velocity shifted towards the upper half of the duct and was distributed more uniformly than the 400k grid in Figure35(a). The secondary flow pattern suggested four discrete vortices. The maximum velocity in the core was $1.4u_{avt}$. The velocity deficit along the bottom of the duct correlated well with $u=0.40u_{avt}$. The v-component in Figure 39(b) has opposing minima and maxima in the lower and upper halves of the exit plane consistent with two pairs of counter-rotating vortices. The magnitude of v is slightly larger in the top than in the lower half of the duct. The magnitudes of the top half are $0.12u_{avt}$ for the maximum and $-0.16u_{avt}$ for the minima. The lower half has a minimum of $0.14u_{avt}$ with a maxima of $0.10u_{avt}$. The w-component also corresponds with the flow direction required for two pairs of streamwise vortices. The w-component ranges from $\pm 0.12u_{avt}$.

The features in the vertical duct agree with the observation in the experimental data. The components were weak compared to the horizontal nozzle. The maximum

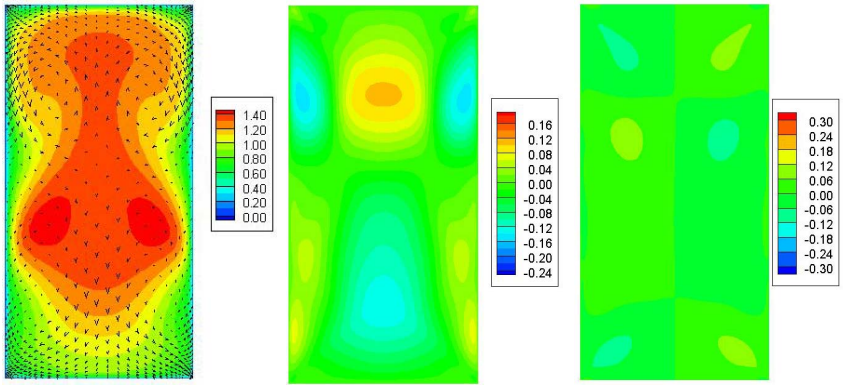

(a) u/u_{avt} (b) v/u_{avt} (c) w/u_{avt}

Figure 39. Mean velocity at the high resolution, third order discretization of the vertical duct using RSM for a 4M node grid.

matches with the LDV results at $1.4u_{avt}$. The v-component determination near the edge of the jet is difficult. The LDV measured weaker features than predicted by the RSM study. The difference of $0.12u_{avt}$ compared to the $0.16u_{avt}$ is a difference of 2%, potentially attributable to measurements obtained outside the duct. The w-component results, shown in Figure 39, are similar to the lower resolution case in Figure 35(c). The positive and negative regions fall in the same spatial locations. Correlation to the LDV results proved difficult, as shown by the measurements in 31(c). The w-component has the same range and magnitude. The secondary flow behavior, as overlaid on the u-component of Figure 39, demonstrates two weak vortex pairs. The vectors have the same magnitude as those used in horizontal nozzle.

The turbulent kinetic energy components for the vertical duct are given in Figure 40. The fluctuating energy or the u'u'-component concentrates in the lower half of the duct, the region created by the velocity shift and flow separation.[11],[14] The higher fluctuations in this region for the v'v'-component correspond with the flow equalization desire. The greater fluctuations were generated by shearing between the flow regions. The fluctuating v'v'-component in Figure 37(b) focused on transferring the momentum in the y-direction, creating the large values. This forms from the secondary flow redistributing the mean flow to restore balance. The w'w'-component

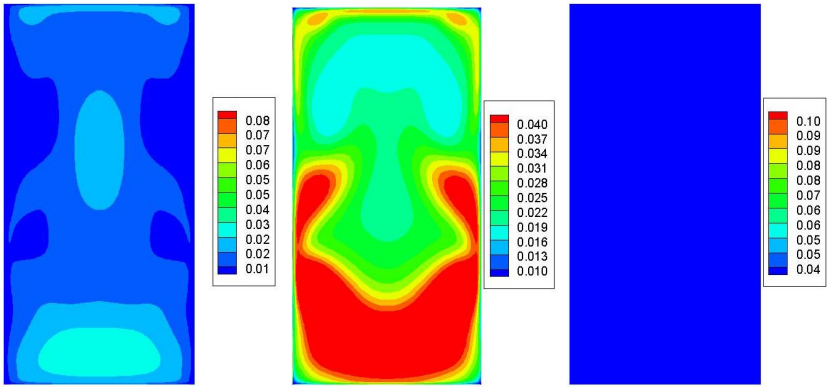

(a) u'u'/u^2_{avt} (b) v'v'/u^2_{avt} (c) w'w'/u^2_{avt}

Figure 40. The turbulent kinetic energy predicted by RSM for the high resolution 4M node grid and third order discretization for the vertical duct.

is featureless on the scale dictated by the experimental results, as shown in Figure 37(c).

The Reynolds shear stresses computed for the vertical duct simulations are shown in Figure 41. The flow features for the u'v'-components range from -0.018-0.014u^2_{avt}. A maximum exists at the top with a large minimum at the bottom. Two local maxima appeared in the center of the duct for the u'v'-component with a magnitude of 0.010u^2_{avt}. The u'w'-component has a maximum on the left and a minimum on the right with magnitudes of $\pm$0.010u^2_{avt}. The v'w'-component matched pairs of minima and maxima for a total of two each. The upper set is lower in magnitude than the bottom pair. The minimum and maximum are -0.003 and 0.004u^2_{avt}. The behavior observed in the computational study agreed with the LDV measurements for the shear stresses. The ranges were close in magnitude for the all three components, with main features accounted. The u'v'-component for the computational study is 2% smaller than the experiment for the minimum and maximum predicted. The pair of localized maxima in the center of the duct exhibited in measurements. The u'w'-component displays the split of positive shear stresses on the left and negative shear stresses on the right with the magnitudes being approximately the same. The v'w'-component is less conclusive with four apparent regions appearing in this computational result.

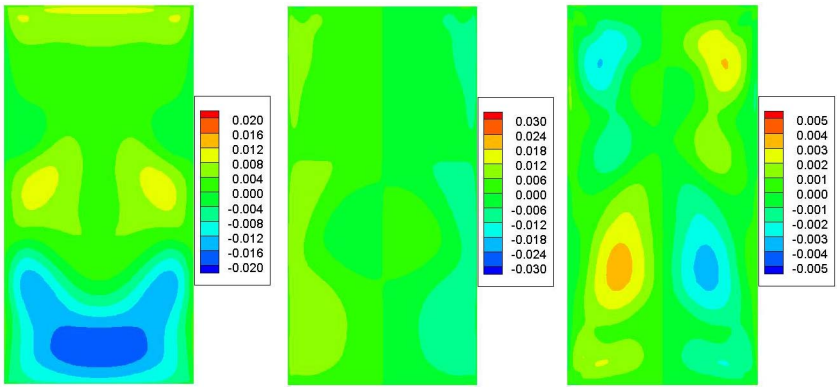

(a) u'v'/u^2_{avt} (b) u'w'/u^2_{avt} (c) v'w'/u^2_{avt}

Figure 41. The Reynolds stresses for the vertical RSM computational model for the third order discretization with 4M nodal points.

The computational results for the vertical nozzle predict four weaker vortices. Information in the shear stresses agree with the trends measured by the LDV existed. The shear layer obscured some of the flow structures, particularly in the weak secondary flows and its constituents. The overall magnitude and flow features correlated between the two results. The peak streamwise velocity was shifted toward the outer region of the second bend at the duct exit. The overall magnitude of the secondary flow features was weaker than those of the horizontal duct. The v-component indicated the presence of high and low velocity regions even though not all the features were captured. The u'v'-component displayed a large region of higher turbulence in the bottom of the duct where the streamwise velocity deficit occurred from the streamwise velocity shift. Additionally, two maxima in the u'v'-component formed in the region between the upper and lower half of the duct. Differences existed, but sufficient correlation exists to warrant investigation of the interior. The location of the vortex formation discerned from the results. Closer examination shows the differences and similarities between the computational and experimental results.

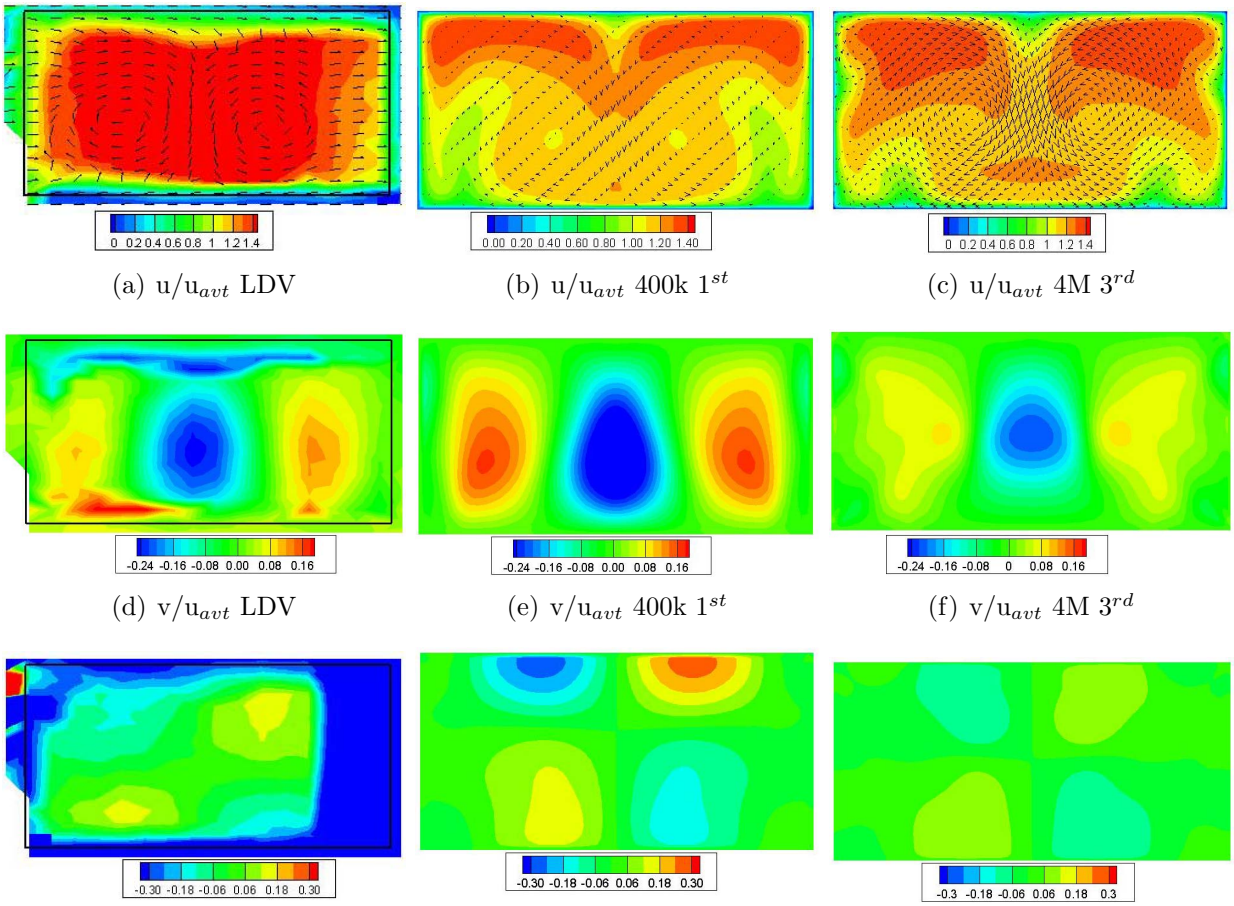

(a) u/u_{avt} LDV (b) u/u_{avt} 400k 1^{st} (c) u/u_{avt} 4M 3^{rd}

(d) v/u_{avt} LDV (e) v/u_{avt} 400k 1^{st} (f) v/u_{avt} 4M 3^{rd}

(g) w/u_{avt} LDV (h) w/u_{avt} 400k 1^{st} (i) w/u_{avt} 4M 3^{rd}

Figure 42. Comparison of the RSM models to the LDV data for the horizontal duct for the mean components of the velocity.

4.7 Comparison of Computational and Experimental Results at the Exit Plane

To summarize the results a direct comparison of the computational and experimental cases for the mean velocities are shown in Figures 42 and 43, for the horizontal and vertical ducts, respectively. The first order discretization was more dissipative and the third order less due to the sensitivity to the flow variations. The grid resolution played a part in allowing finer flow structures resolution compared to the coarser grid's capabilities.

Figures 42(a) through (c) for the streamwise u-component show higher velocities are distributed at the upper half of the duct and towards the vertical centerline. In Figures 42(d)-(f), the numerical solutions show two positive v-component velocity regions with one negative region in the middle. The w-component also has four indicated regions of two minima and maxima that correspond to the experimental results. The 4 million grid cell solution has better correlations to the experimental results in the magnitude of the velocities. Small scale features formed in the (c) in the refined grid that were unresolved in the experiment and coarse grid Figure 43 show the exit results for the experimental data and the two different numerical solutions performed for this work. The expected streamwise velocity shift appears both numerical solutions of Figures 43(b) and (c). The 4 million grid solution correlate better with the experimental results in Figures 43(a) and (d) for the u and v-components. In particular, the 400k solution in the v-component lacks the middle region in the upper half of the figure that matches a positive velocity. This region of positive velocity was predicted in the 4 million cell grid. The w-component was very weak in all solutions and in the experimental results. Comparison of the results between the experimental and computational results was difficult. The numerical simulations predicted the basic flow behavior and flow physics.(78) The general shape of the main flow structures represented well in comparison to the LDV for both the horizontal and vertical ducts. The secondary patterns established the strongest of the features. The smaller scale structures were beyond evaluation and the RSM model represented the flow.

Slight variations in the magnitude between the experiment and 3^{rd} order computational result are normal. The mass flow controller provides consistent flow but experiences variation. The variation accounted for the higher velocities. The assumption of sea level conditions for the computational study inaccurate. A higher normalizing value for the LDV data accounts for the differences. A correction to the horizontal duct examined the velocity profile with the CFD, accounting for the higher exit velocities. Figure 44 is the profile for the LDV if normalized by a higher theoretical flow rate average through the serpentine duct. Rather than normalizing

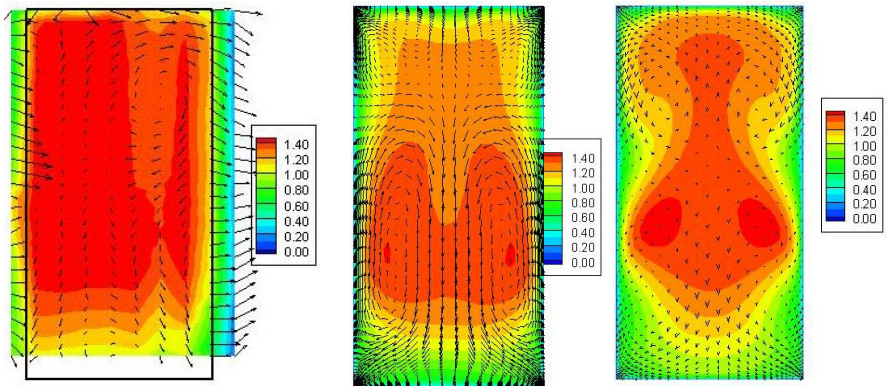

(a) u/u$_{avt}$ LDV (b) u/u$_{avt}$ 400k 1st (c) u/u$_{avt}$ 4M 3rd

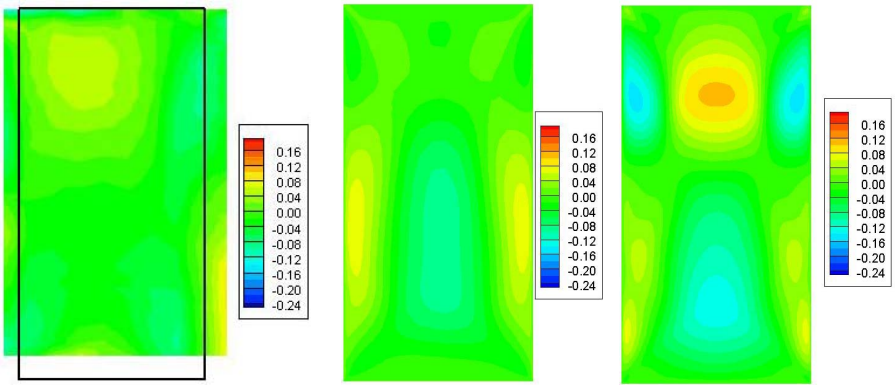

(d) v/u$_{avt}$ LDV (e) v/u$_{avt}$ 400k 1st (f) v/u$_{avt}$ 4M 3rd

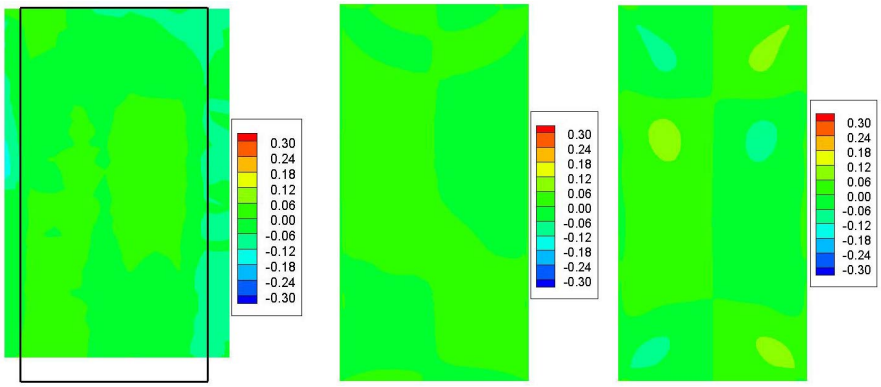

(g) w/u$_{avt}$ LDV (h) w/u$_{avt}$ 400k 1st (i) w/u$_{avt}$ 4M 3rd

Figure 43. Comparison of the means components of the velocity for the vertical duct for the computational and LDV results.

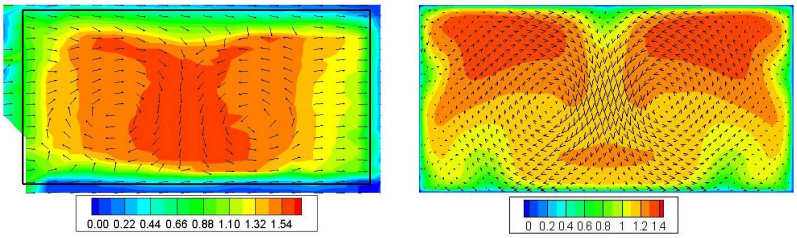

(a) u/u_{avt} LDV (b) u/u_{avt} 4M 3^{rd}

Figure 44. Comparison of the streamwise velocity to the computational with scale adjustment for the higher flow rate u_{avt}.

by another value, the scale increased to $1.65u_{avt}$ instead of the $1.4u_{avt}$. This simulates the difference imposed by the sea level and coincidentally higher flow rate with the contour map adjusted to show similarities. The higher velocity regions on each side of the y-centerline at the top of the duct are visible, a higher velocity region formed at the bottom of the y-centerline. Good agreement exists between the computational and experimental results if the flow rate conditions factor into the experimental result. The results obtained for the LDV were good in general, and not the problem.

The comparison distinctly showed the similarities between the results. Magnitude differences for the coarse grid illustrate grid resolution errors. The higher order discretization compared to the experiment. Adjustments in flow rates provided closer correlation, monitoring the mass flow regulator output required to quantify the inconsistency. Overall, the main flow features established in all the results. Further examination gleaning information on the vortex and flow development observed at the exit.

4.8 Interior Examination of Computational Ducts

Additional planes in the interior of the nozzles determine the flow evolution within the serpentine ducts with the high curvature and differing aspect ratios. The flows shown in these figures go from left to right, following convention. The development of the flow for each of the horizontal duct mean velocity components are given in Figure 45. The u-component shown in more detail with overlaid secondary flow

components is given in Figure 46. Separation occurred on the latter half of the second bend in the serpentine ducts with a region of recirculating flow in the inner bend.

The flow begins uniformly in both serpentine ducts in Figures 46(a). As the flow approaches the first bend, some effects of the curvature are seen, as the effects translates upstream in subsonic flow.[12],[13],[18] The velocity shift is evident near the outside of the first bend. After the first bend, the primary direction of the flow is upward. The highest positive values for v occur near the outside portion of the duct, while no separation is present near the inside of the turn. Flow separation is minimal, but present, in the duct at plane five just after the second bend. At plane 5, the largest values for the u-component occur near the inside radius, rather than the outside radius. From planes 6 and 7, it can be observed that the peak velocity region essentially splits with each half rotating about the duct. This is consistent with the formation of two streamwise vortices, and the v-component and w-component results illustrate their development in this section of the duct.

If one considers the counter-rotating pair of streamwise vortices, which develops from a turn, it can be rationalized that the secondary flow structure observed at the exit of the horizontal nozzle develop from the first bend, as shown in Figures 45 and 46. These dominant vortices restricted the second bend's structures to a small region in the lower portion of the horizontal duct, shown in Figure 46(f) and (g). The small secondary flow was difficult to measure at the exit plane, due to the development of the free shear layer. Ultimately, only one dominant vortex pair, with a downward velocity in the center exists in the horizontal duct. The examination of the vortex growth through the duct explained the opposing rotation of the vortex to the expected direction if the flow had only passed through the second ninety degree bend.[16] The horizontal duct has flow dominated by the growth of the vortex pair created by the first ninety degree bend, the second pair is essentially nonexistent, as shown by the progression of the secondary flow in Figure 46.

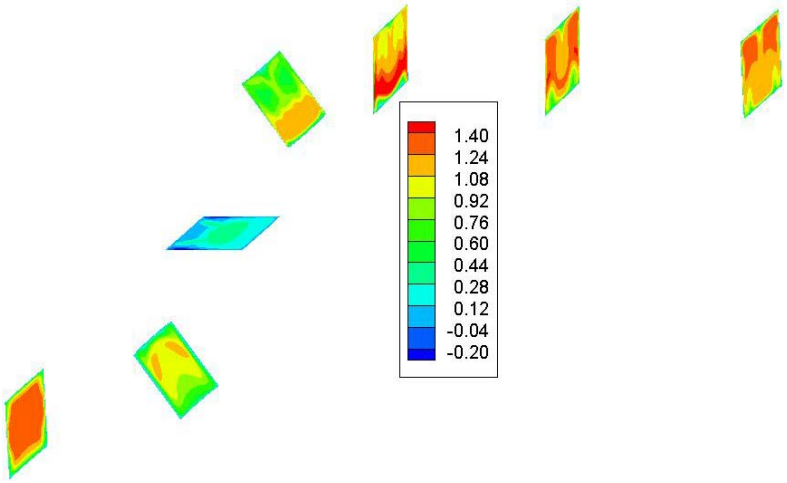

(a) u/u_{avt}

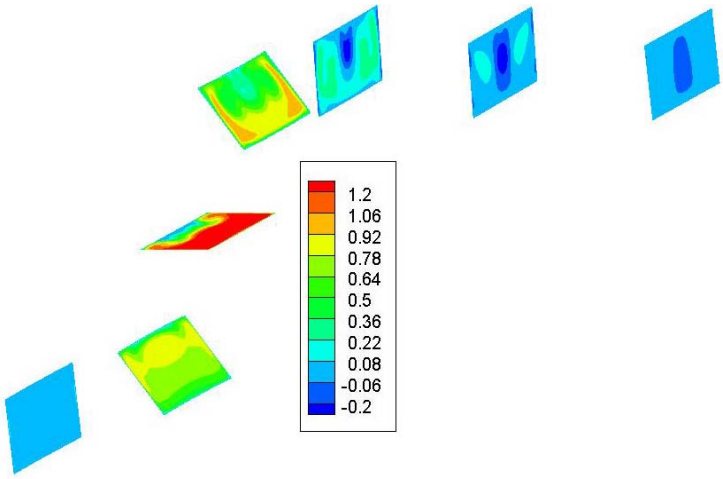

(b) v/u_{avt}

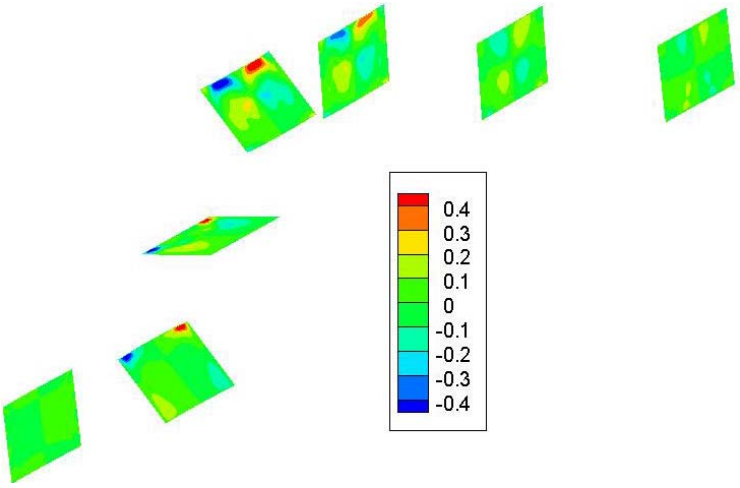

(c) w/u_{avt}

Figure 45. Flow development through the horizontal duct for the third order discretization of the RSM model with 4M nodal points. Flow follow convention going from left to right.

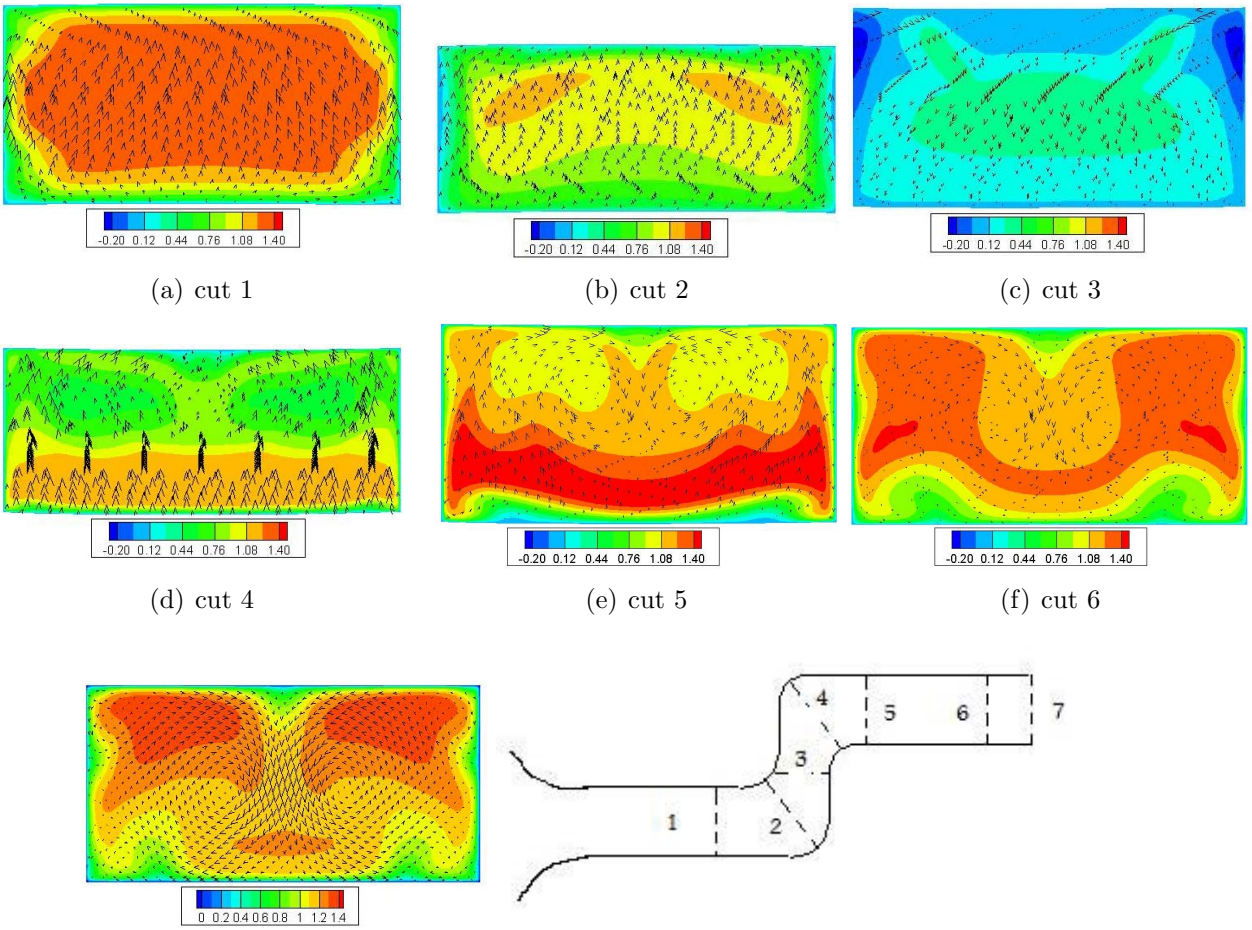

(a) cut 1 (b) cut 2 (c) cut 3

(d) cut 4 (e) cut 5 (f) cut 6

(g) cut 7 (h) cut planes

Figure 46. Streamwise development of the horizontal duct for the 3^{rd} order RSM with 4M nodal points.

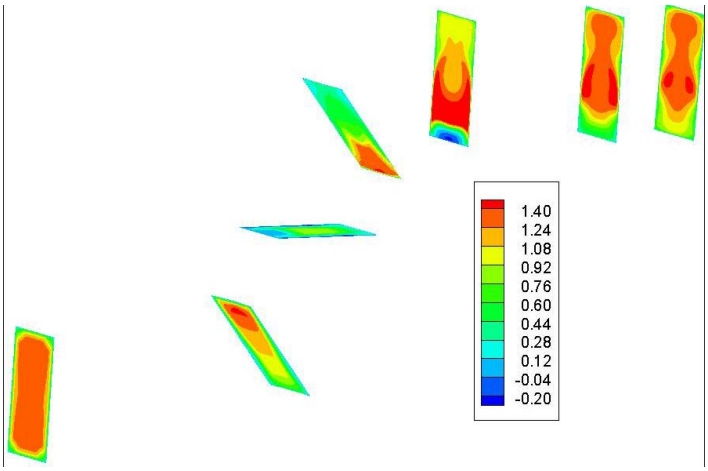

(a) u/u_{avt}

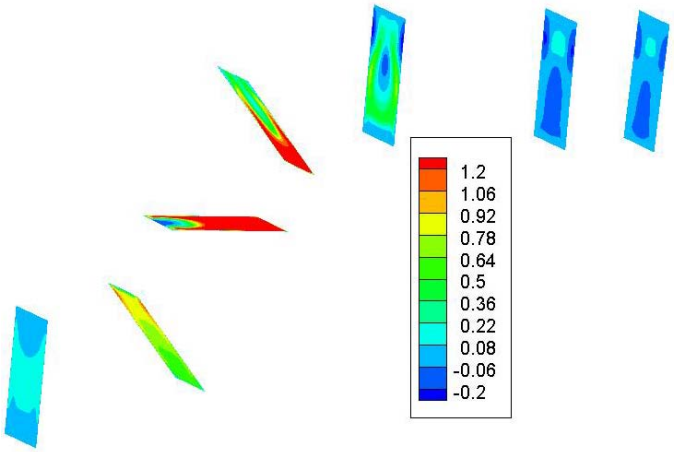

(b) v/u_{avt}

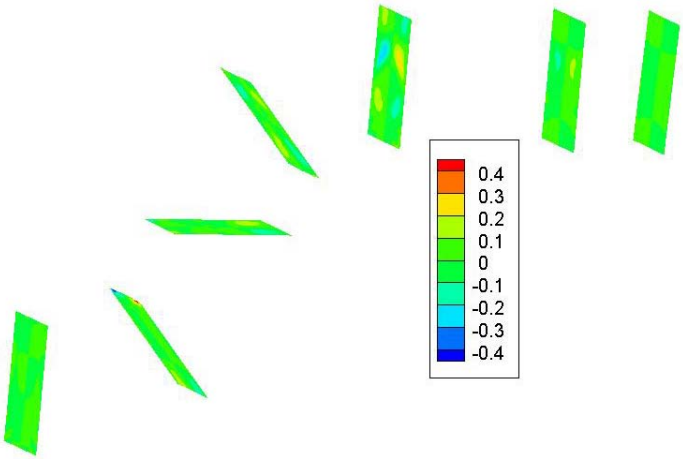

(c) w/u_{avt}

Figure 47. Flow development through the vertical duct for the third order discretization of the RSM model and 4M grid points. The flow follows convention going from left to right.

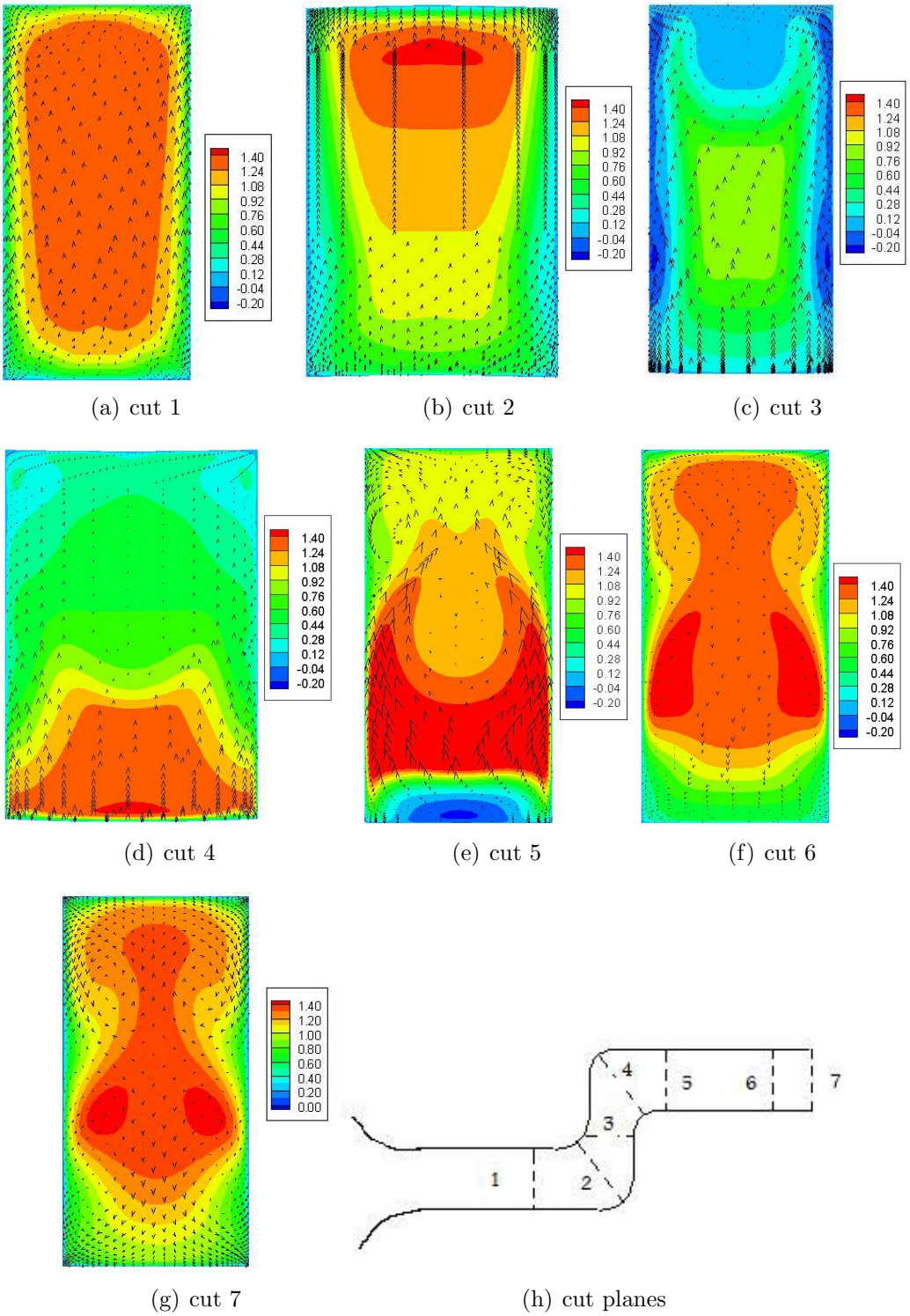

(a) cut 1 (b) cut 2 (c) cut 3

(d) cut 4 (e) cut 5 (f) cut 6

(g) cut 7 (h) cut planes

Figure 48. Normalized streamwise development of the vertical duct for the 3_{rd} order RSM with 4M grid points.

Table 5. Summary of the computational wall normalized value found for the serpentine ducts.

Model	Max y+
horizontal	
RSM 1^{st}, 400k	12.39
RSM 3^{rd}, 4M	9.36
vertical	
RSM 1^{st}, 400k	1.2
RSM 3^{rd}, 4M	1.36

The evolution of the flow through the vertical duct is shown in Figure 47 and with more detail in Figure 48. Despite having the same hydraulic diameter and flow rate, the results are far different from those for the horizontal nozzle. The computation for the vertical duct yielded two pairs of vortices at the exit, as shown in Figure 48. From the depiction of v in the third plane of Figure 47(b), one can observe that the strong upward flow after the first bend is concentrated near the outside bend. From the fifth plane of Figure 47(a), the highest streamwise velocities after the second bend are near its inside radius. The stronger secondary structures redistribute the momentum in the serpentine duct to create a more uniform velocity profile. The secondary flow works to redistribute the peak streamwise velocity, which makes the efficiency of the redistribution dependent on the flow magnitude.

One important difference between the CFD results for the two nozzles is that the vertical nozzle had a much larger region of separation after the second bend. The region of separation is generally very difficult to predict. In the Reynolds stress model one indicator of the validity of the approach is y^+. The summarization of the y^+ is provided in Table 5. The y^+ place the computational solutions in perspective in regards to boundary layer resolution. The y^+ and wall normalized height affects the legitimacy of the computational results. According to Tannehill, any value of y^+ below twenty resolves the wall region sufficiently.[96] For wider acceptance preference for the wall number y^+ is less than one. The higher the y^+ value, the more problematic the resolution of the boundary layer equations. The maximum value for the horizontal duct is much higher and more questionable than that of the vertical nozzle despite the

better agreement of the results with the experimental. Both computational results captured the gross flow features, the number of vortices present and the velocity shift of the core. Better resolution required great computational cost with higher grid resolutions than performed in this study. The relatively large region of separation for the vertical nozzle helps explain why there is less agreement between the CFD and the experiment for that case. The values of the y^+ in Table 5 advise that the region of the bends are less reliable than the rest of the duct. The higher values of y^+ occurred in the turning regions of the flow. The rest of the results fell within the desired range of y^+=1.0.

Even though the serpentine ducts are low Reynolds number flows with a simple geometry, a very complex flow was cultivated. The number of vortices formed and the flow behavior obtained for the two aspect ratios were very different and geometry dependent. The LDV provided a means to validate the computational results while the computational results elucidated the creation of some of the flow features. The third order model compared closely to the experimental results in the magnitudes of the velocities. The higher resolution of the flow field and smaller dissipation of the Reynolds stresses better represent the flow. The computational study displayed regions lost due to wall proximity for the LDV and clarified measurements in regards to the w-component.

The submerged inlet has much milder s-curves than the serpentine ducts, providing easier predictions for a typical RSM model, since the likelihood of separation is reduced. The experimental and computational results demonstrated that the LDV captured fairly small velocity differences with some veracity in all mean and fluctuating components. The u'v' shear stresses were especially well represented, while some trends were obtained from the u'w' and the v'w'-components. This suggested that the flow control's impact upon the submerged inlet and the effect on the flow field would be measurable by the system.

V. Submerged Inlet Results and Analysis

Given the level of insight into the flow behavior of the serpentine duct gained via the LDV system, similar measurements were expected to shed light on the submerged inlet. The submerged inlet has a rectangular entrance at the throat preceded by the ramp, as shown in Figure 1. The curvature is less prominent than that of the serpentine ducts. The throat aspect ratio received attention from Knight et al.[37], Lee et al.[46], Kim et al.[104] and Mossman et al.[1]. A uniform pressure at the compressor face is a typical goal. A more uniform boundary layer region formed in Lee's study through a small ramp width compared to the height of the entrance.[46] The ramp boundary layer deficit accounted for less variation in stresses experienced by the compressor blades. These studies demonstrate the effect of geometry on the submerged inlet. The velocity ratio of the inlet speed to the freestream velocity is also important, as noted by NACA. The ratio is normally closer at flight speeds, the ratio tested at 3.6 U_{av}/U_{∞} is typical of takeoff and landing conditions.

In general, the primary goal of passive or active flow control in the submerged inlet is a more uniform flow, the basis for this study and all other attempts to improve the pressure recovery. The general shape of the NACA submerged inlet ensured that the model had some of the characteristics of an aircraft while keeping the model compact for testing. Line traverses in the interior of the model along the y-axis and z-axis at the inlet throat provided preliminary data on the inlet. A simple method of quantifying the effect of the flow control developed from examining the velocity profile for the inlets in this manner. A full grid covering a region of the y-z plane at the throat provided more information on the inlet profile.

Blowing through multiple jets rather than a slot served as the flow control method for this investigation. It was necessary to establish whether the jets themselves introduced non-uniformity. Jet theory for a single free jet initiated a preliminary estimate determining the required mixing distance for jet overlap to cover the inlet width.[14] Equation 9 was used to calculate the distance for the half-widths to meet. The components of the equation and the jet profile are shown in Equation 7 and Figure

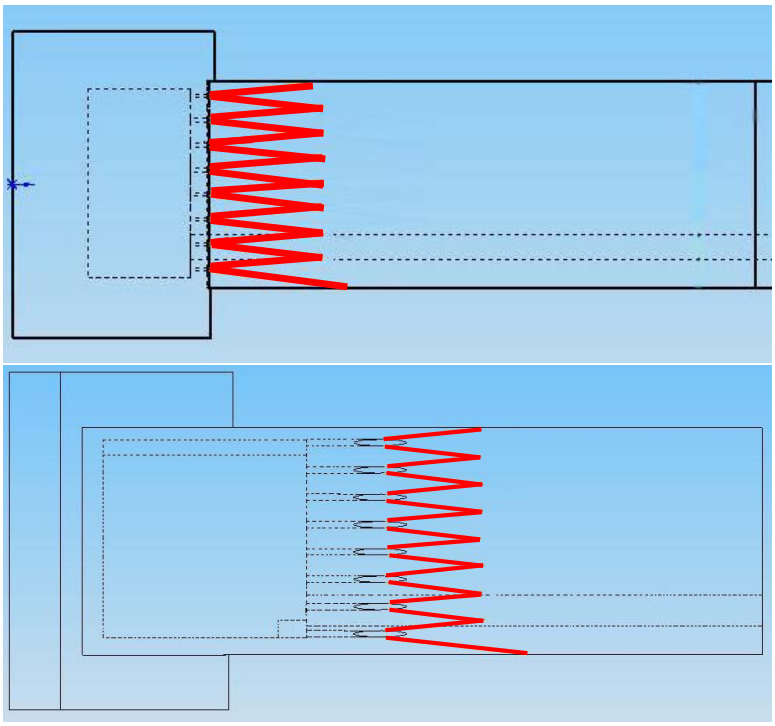

Figure 49. Mixing overlap distances predicted by laminar jet theory for a seven degree spread for the inlet configurations. Two configurations are shown, the step (top) and the ramp(bottom) for the straight jet with the projected spread rate and overlap of the jet.

9. The term z/δ is the spanwise distance over the streamwise distance. The equation was covered further in the experimental chapter, but is briefly highlighted here. Laminar theory generated a conservative estimate while turbulent theory predicted the jets' dispersal within millimeters of exiting (turbulent jet divergence occurs at a half angle of thirteen degrees).[14] Laminar growth of the jet had a slower breakdown of the core momentum. The momentum redistributed more slowly than a turbulent jet. In Figure 9, the jet growth rate is shown for approximately seven degrees, corresponding to the predicted value of u/u_s=0.10. The representation of a seven degree jet spreading rate is shown in Figure 49 for the flow control figurations. The predictions show that the overlap should occur well before the throat, if this were a reasonable characterization of the jet.

$$U/U_s = sech^2(z/\delta) \tag{9}$$

More streamwise distance allotted for mixing ensured mean velocity variations negated before the inlet throat. While jet theory provided a reasonable estimate of mixing length, the conditions experienced were far from that of a single free jet. Shearing of the jets occurred from the ramp surface and the freestream, and there are some similarities to a [Glawe et al[84]] study for a wake profile. Two of the flow control configurations exited from a short backward facing step. The jets issuing from the ramp surface exited at an angle of seven degrees to the primary flow. Cross-flow mixing is a common occurrence in combustion, due to the concern of fuel dispersal.[90],[91],[81],[85],[89] The additional complications affect the mixing and spreading of the jet. For this reason, additional length for jet mixing was included in the design to improve the flow control uniformity at the inlet throat, as evidenced in Figure 49. The spreading angle for the jets was seven degrees as calculated from laminar mixing theory. The jets were centered to the best ability in the program however some discrepancy still formed on one side compared to the other in the symmetry. Another reason to provide this margin for error is that the different definitions of the mixing length are dependent on the component of interest. The mean flow develops quickly while the turbulence requires more time.[14]

As discussed in Section 3.5 of the experimental setup, four different flow control geometries were studied. The first configuration examined was the straight step, defined in the configurations of Figures 7 and 8(a). The jets entered the flow from a backward facing step and exited parallel to the streamwise direction (x-direction) without spanwise fanning (z-direction). This configuration was similar to the geometry investigated in RECITE with the exception that the jets were used in place of a single slot.[25] The jets theoretically require less mass flow to achieve the same results as the slot used in the AFRL study.[25] The exit velocity of the jet is faster than the corresponding flow rate for the slot for the same mass flow rate.[10] The slot with the highest exit velocities in RECITE required far more blowing than what would be acceptable for the bleed allowance off the compressor. This study investigated blowing from discrete holes.

The straight step configuration was tested under a variety of circumstances to establish general trends in the flow control. Figures 50 through 59 pertain only to this geometry. Figures 60 through 79 are focused only on a comparison of the four flow control geometries described in Chapter 3, the experimental setup.

5.1 Linear Traverses

5.1.1 Z-direction for 259 scfm up to 2% mass flow addition, Straight Step configuration. Linear traverses of the LDV probe, referred to as *line studies*, determined if the jets' effectiveness in the inlet existed. The half grids were more time intensive. Centerline traverses in the z and y-direction served at first with the vacuum pump as a preliminary examination at higher speed flows. Later a few vertical lines examination near the wall extended the examination. Mass flow addition, up to 2%, ascertained whether low flow additions sufficed. The line studies served as a means of determining if there were any visible trends. The highest mass flow rate was the 259 scfm flow through the inlet. The centerline traverses at this condition, the free stream velocity was 26.82 m/s. The mass flow rate and freestream velocity referenced as U_{av}/u_{∞}=3.8, the results are shown in Figures 50-55. The inlet velocities normalized by the average inlet velocity calculated from the data U_{av}.

At this condition and location, the effect of the 2% flow control (5.18 scfm) was minimal. The profile is uniform to within $0.02U_{av}$ in the mean u-component, some of the near wall effects captured by the LDV (z=23 mm). An addition of two percent of the mass flow through the inlet served to alter the inlet uniformity for the data shown in Figure 50. Regardless of the flow control addition, the u-component decreased on the near wall of the inlet consistent with the no-slip condition. The slight decrease in velocity approaching the far wall (z=-23 mm) showed that the flow field was mildly asymmetric. This phenomenon surfaced in all configurations of the flow control to a lesser extent, a consequence of this particular inlet and wind tunnel orientation. The positioning of the inlet model towards the near wall of the wind tunnel (positive z-direction) induced the asymmetric flow possibly. The necessary curvature required

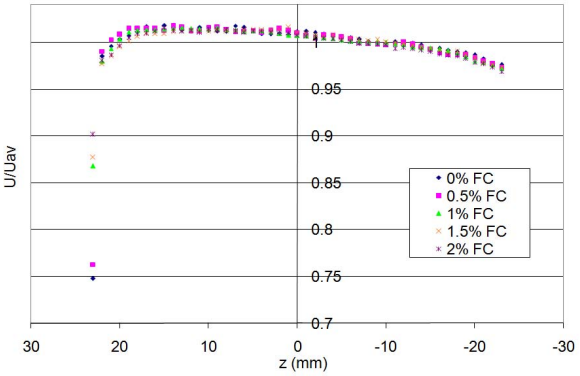

(a) u/U_{av}

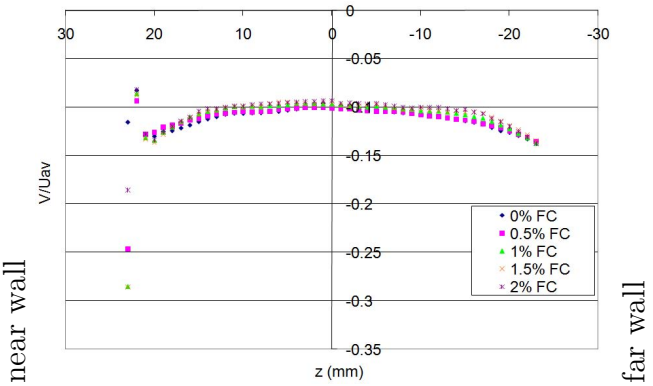

(b) v/U_{av}

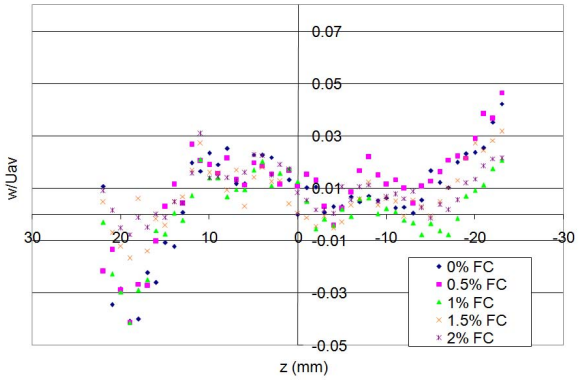

(c) w/U_{av}

Figure 50. The mean velocity for the 259 scfm flow obtained with the vacuum pump through the line traverse across the z-direction at y=0. (U_{av}/u_{∞}=3.8)

by the hose downstream of the model leading to the blower introduces another factor for the minor asymmetry of the u-component.

The v-component is symmetric without any deviance at the far wall. The velocity at the center was near -0.1U^{av}, as shown in Figure 50(b). The nonzero value of the v-component is a consequence of the throat angling downward slightly at the throat or near throat region. Some of the near wall effects evidence in the results, the increasing downward trend created by the wall spillage after a slight decrease in the magnitude. The w-component in Figure 50(c) is antisymmetric with a slight positive mean velocity. Overall, the value of $\bar{w}$=0.01U_{av} is low. In all of the mean velocity components shown for the linear traverses in Figure 50 the effects of the flow control (up to 5.18 scfm or 2% of the mean flow) were minor.

The fluctuating velocities for the z-direction traverse at y=0 are shown in Figure 51. The streamwise fluctuation in Figure 51(a) has no discernable trend with the application of flow control up to 2%. The fluctuating u'-component ranges from 0.01-0.036U_{av}, consistent across the inlet. The v'-component, given in Figure 51(b), is uniform in the middle with increasing energy near the walls. The fluctuations for v' range from 0.015 in the center to 0.060 at the walls. The w'-component is an order of magnitude higher than the u' and v'-components, showing the difficulty in accurately measuring the w-component of the velocity. The w'-component is fairly uniform with no distinctive characteristics ranging from 0.14-0.20U_{av}. For all components of the fluctuations there were no visible trends to the turbulent kinetic energy's behavior for mass additions up to 2%. The energy from the jets remained below the y=0 location closer to the ramp. This examination determined that the inlet was generally symmetric. The low mass flow additions (2% or less) remained below the midline of the throat or dispersed before the throat region. Examination near the ramp was needed to determine if the low flow control addition affects the flow near the ramp of the inlet.

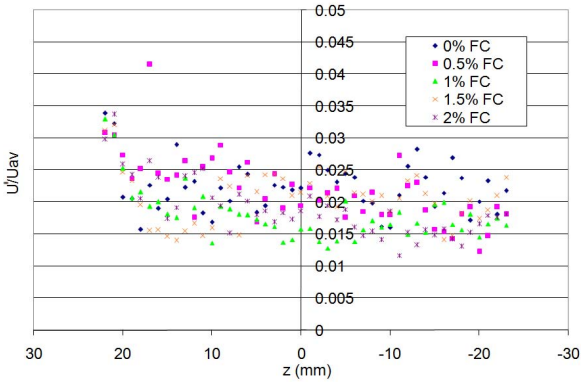

(a) u'/U_{av}

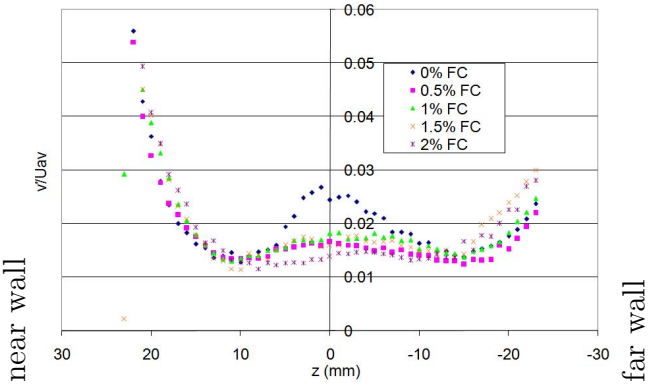

(b) v'/U_{av}

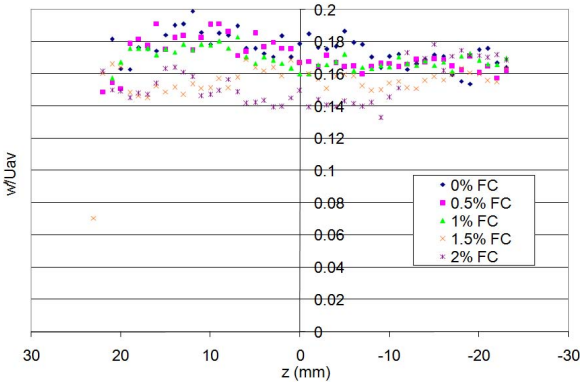

(c) w'/U_{av}

Figure 51. The turbulent kinetic energy components for the 259 scfm flow with the vacuum pump through the line traverse across the z-direction at y=0. (U_{av}/u_{∞}=3.8)

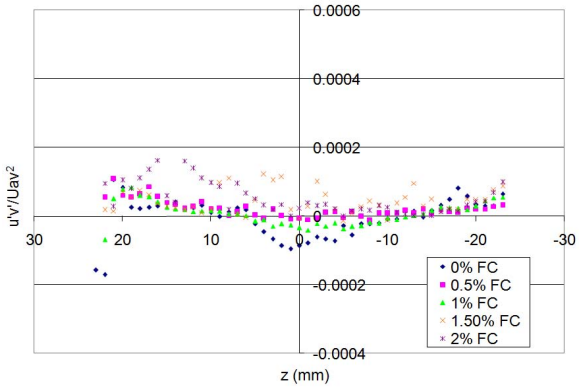

(a) u'v'/u_{av}^2

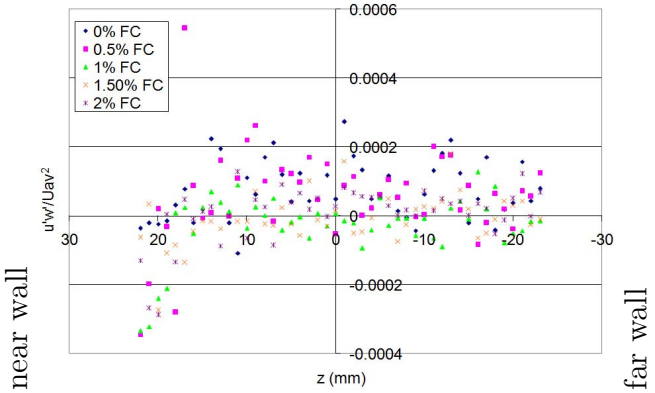

(b) u'w'/u_{av}^2

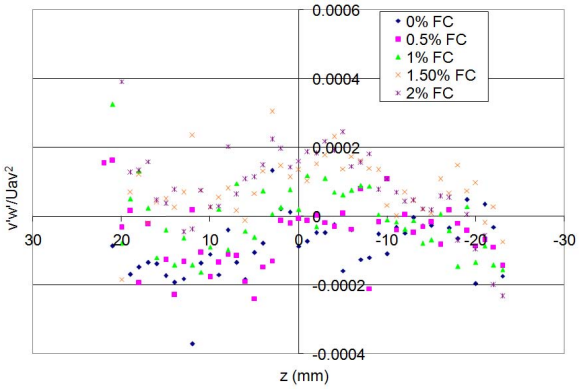

(c) v'w'/u_{av}^2

Figure 52. The shear stresses for the 259 scfm flow with the vacuum pump found through the line traverse across the z-direction at y=0. (U_{av}/u_∞=3.8)

The Reynolds stresses in Figure 52 show that the u'v', u'w' and v'w' Reynolds stresses are fairly uniform, except near the boundary layer. The u'w' and the v'w' were displayed only for the sake of completeness, since the serpentine ducts and w'-component in the centerline determined the unreliability in resolving the fluctuating w-component of the velocity. The increase in magnitude of the turbulence holds with wall shear created by the boundary layer. No visible effect showed with the addition of up to 2% flow control to the shear stresses. The u'w' and v'w' measurements exhibit more noise in the turbulence with the less certain w'-component. The u'v' is mostly under $\pm 0.001 U_{av}^2$, the u'w'and the v'w' are twice this range. The turbulence components in the submerged inlet, based upon Figure 52 indicate the flow is isotropic.

5.1.2 Y-direction for 259 scfm up to 2% mass flow addition, Straight Step configuration. Unlike the data acquired in the spanwise direction, the streamwise velocity data for the vertical centerline was not symmetric due to the due to the ramp turning the flow to enter the throat and the effects of the boundary layer growth. The results of the traverse in the y-direction at z=0 are shown in Figures 53 through 55. The velocity is higher near the lip of the inlet decreasing towards the ramp surface for the u-component, as shown in Figure 53(a). With the addition of flow control the uniformity improved slightly, as indicated by the decrease in the slope of the velocity profile. The slope is quantified in Table 6. The linear fits to the data display the slope alteration by the flow control. The jet velocities were low compared to the inlet flow with the low mass additions and no real change was observed. The jet velocities are given in Table 3 compared to the throat velocity of approximately 100 m/s. The other components exhibit minor effects from the flow control.

The v-component of the y-direction traverse is shown in Figure 53(b). The v-component is nonzero as seen in the z-direction traverse. The downward flow decreases from the lip to the ramp. The v-component experienced a slight shift becoming more uniform with the addition of flow control. The w-component, shown in Figure 53(c), was essentially zero and unaffected by the flow control.

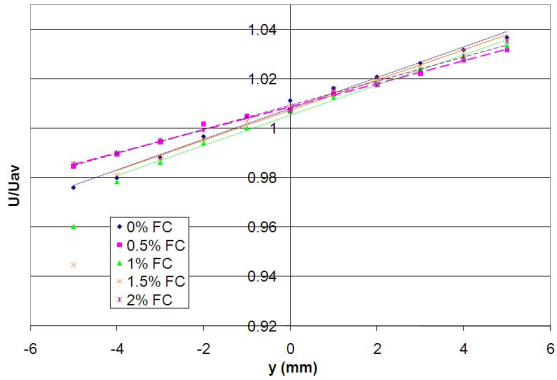

(a) u/U_{av}

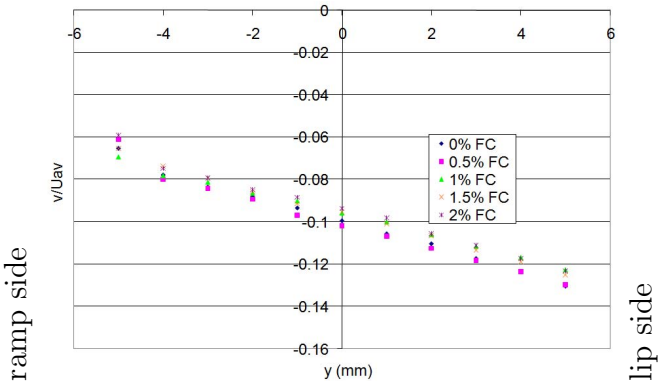

(b) v/U_{av}

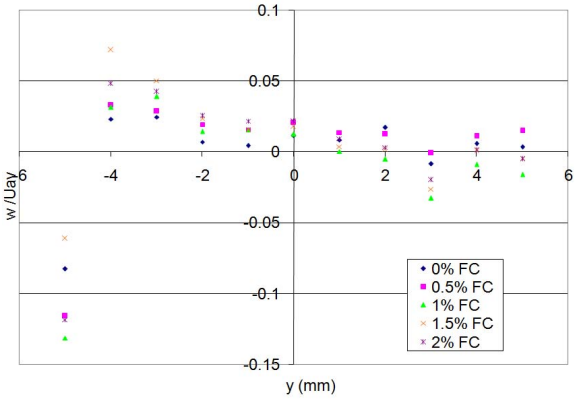

(c) w/U_{av}

Figure 53. The mean velocity components at 259 scfm flow with the vacuum pump found through the line traverse across the y-direction at z=0. (U_{av}/u_{∞}=3.8)

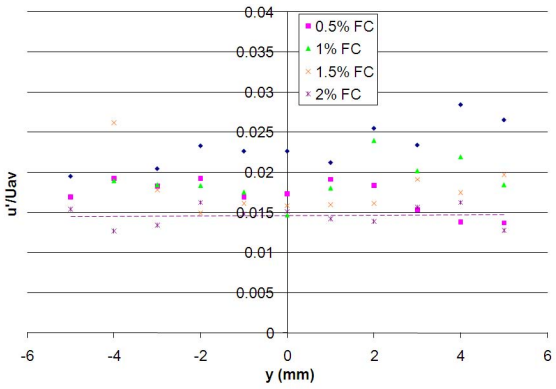

(a) u'/U_{av}

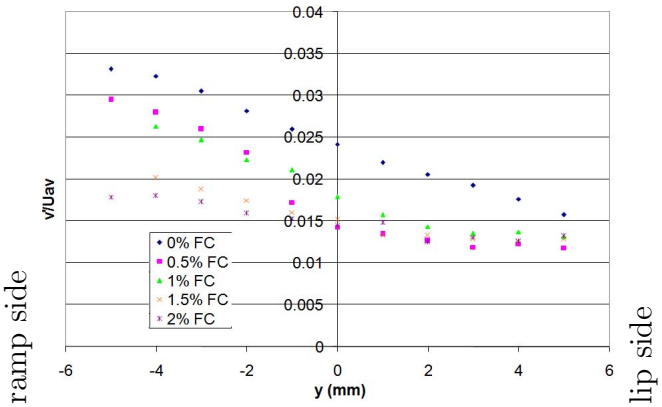

(b) v'/U_{av}

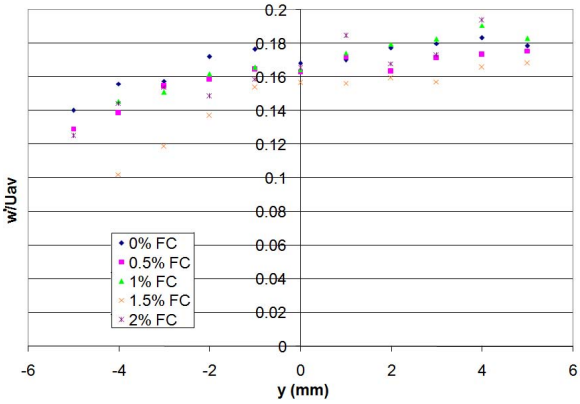

(c) w'/U_{av}

Figure 54. The turbulent kinetic energy components for the 259 scfm flow with the vacuum pump through the line traverse across the y-direction at z=0. (U_{av}/u_{∞}=3.8)

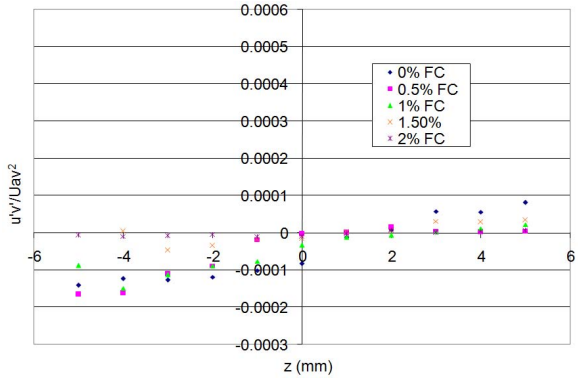

(a) u'v'/u_{av}^2

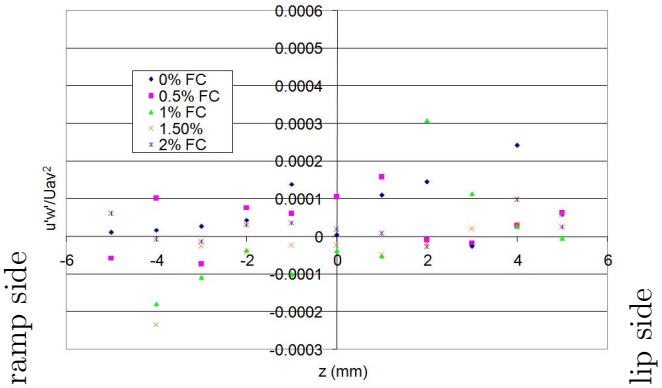

(b) u'w'/u_{av}^2

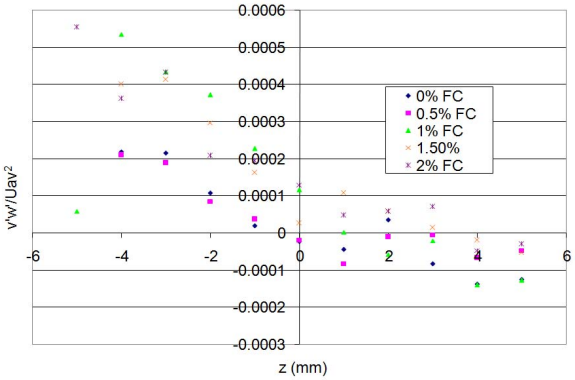

(c) v'w'/u_{av}^2

Figure 55. The 259 scfm flow with the vacuum pump and the flow characteristics found through the line traverse across the y axis. (U_{av}/u_{∞}=3.8)

Table 6. Slope alteration of the u-component with mass flow addition.

Flow control (%)	Slope (normalized by U_{av}
0	0.0062
0.5	0.0047
1	0.0061
1.5	0.0061
2	0.0049

The components of the normal Reynolds stresses are given in Figure 54. The u'-component, shown in Figure 54(a), ranges from 0.01-0.03U_{av}. The energy is consistent over the entire measurement for this component. The v'-component, given in Figure 54(b), increases near the ramp. The flow control apparently affects this component. The v'-component varies from 0.5% at the lip to 2% at the ramp side and ranges from 0.01-0.035U_{av}. The w'-component, shown in Figure 54(c), is slightly antisymmetric around 0.16U_{av}. The range is an order of magnitude higher than that of the u' and v'-components. No trend evinces with the addition of flow control for this component. The only component displaying sensitivity to flow addition is the v'-component. The u'v'-component potentially exhibits this sensitivity as the most reliable of the shear stress components.

The turbulence indicated by all three Reynolds shear stresses in Figure 55 shows the behavior for up to 2% addition of blowing. The turbulence is on the same order of magnitude, generally indicating isotropy with small magnitudes. The u'v'-component is smaller than the other components. The gradient and trend with the application of flow control translated to this component. The range for the u'v'-component is $\pm 0.001 U_{av}^2$, compared to the $\pm 0.002 U_{av}^2$ and -0.001-0.004U_{av}^2 for the u'w' and v'w'-components, respectively. The v'w' turbulence appears to increase near the ramp in the turbulence with flow control, suggesting localized effects at the ramp. The same behavior materialized in the other inlet flow cases for the y and z-centerlines. The other flow conditions examined, are given in Table 7. The vertical traverse confirmed the localized effect of the flow control near the ramp. The two percent mass flow addition was insufficient for improving flow uniformity. The flow remained unaffected

Table 7. Summary of the flow conditions for the submerged inlet. All variations performed for the straight step, all others configurations experienced variation 5.

Variation	Tunnel Velocity(m/s)	Inlet flow rate(m^3/s)	Inlet Configuration	U_{av}/U_∞
1	26.82	0.1222	straight step	3.9
2	26.82	0.0986	straight step	3.6
3	13.41	0.0481	straight step	5.3
4	13.41	0.0415	straight step	4.4
5	13.41	0.0340	all	3.7

for less than 2% mass flow addition. More mass flow addition is necessary to alter the submerged inlet flow profile.

5.1.3 Throat Velocities 72-259 scfm at tunnel speed of 30 and 60mph, Straight Step configuration. Information for the different flow conditions are given in Table 7. The straight step was tested over the most conditions, providing a basis for comparison to the other geometries. All variations of the flow control configuration occurred for the zero and one percent additions of the straight step. Focusing first on 0% flow control cases for the mean velocity components, the z-direction at y=0 has the same behavior for all U_{av}/u_∞. The behavior is the same as observed for the 259 scfm case. The mean velocity components collapse when normalized by the mean streamwise velocity. This demonstrates that the results for one flow variation essentially hold for the others. The u-component in the z-direction is shown in Figure 56(a) to collapse to within 2% of each other. Overall, the behavior in the center of the inlet is similar in Figures 56(c) and (e). The v-component collapses to within 2% in most regions except near the wall. A 5% variation in v/U_{av} forms in the near-wall region corresponding with increasing U_{av}/u_∞ increasing the downward velocity. For example, at z=20 mm, v/U_{av} is $-0.18U_{av}$ for 60 mph freestream velocity with an inlet mass flow rate of 209 scfm, but only $-0.12U_{av}$ for the 60 mph freestream with inlet mass flow rate of 259 scfm. The w-component is noisy with a variation of around 7%. There is little difference in the u, v, and w-components with the addition of one percent flow control,

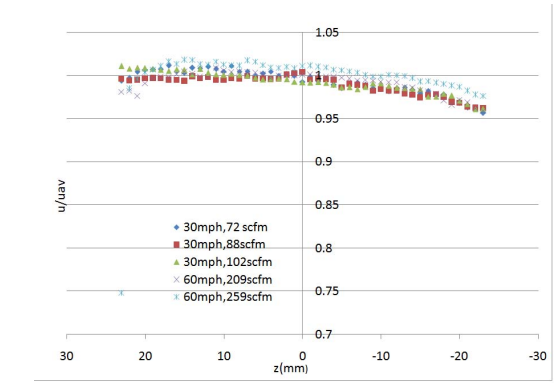

(a) 0%u/U_{av}

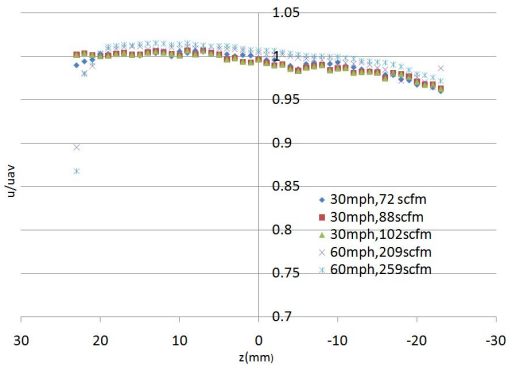

(b) 1%u/U_{av}

near wall

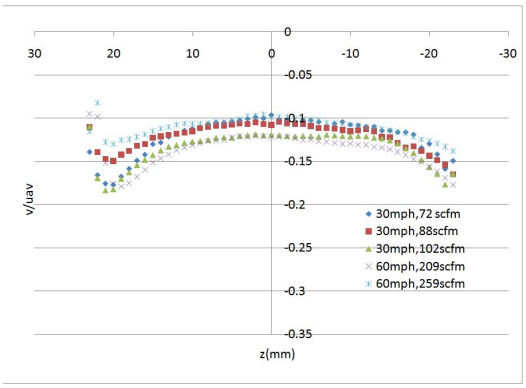

(c) 0%v/U_{av}

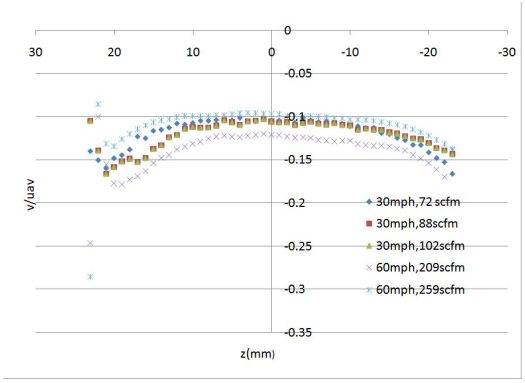

(d) 1%v/U_{av}

far wall

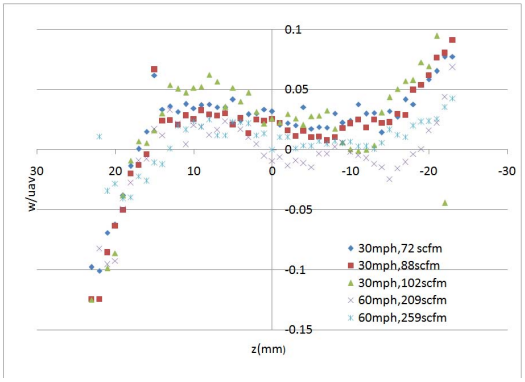

(e) 0%w/U_{av}

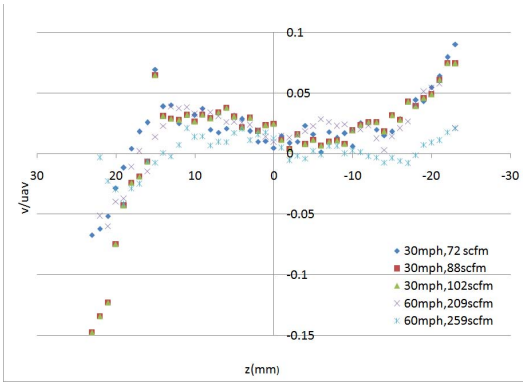

(f) 1%w/U_{av}

Figure 56. Comparison of the 0% and 1% flow addition for the mean velocities in the z-direction linear study at y=0. Refer to Table 7 for the inlet to freestream velocity ratios.

as shown in Figure 56(b), (d) and (f) respectively. The behavior is identical at the centerline for these mean velocities.

The slope of the u-velocities, shown in Figure 57, are the same as those observed in Figure 53 for the flow variations in Table 7. The y-centerline data given in Figure 57(a) and (b) for the u-component with zero and one percent flow control do not collapse as closely as the z-centerlines in Figure 56. The velocity gradient changes slightly with the ratio of U_{av}/u_{∞} and the gradient created by the ramp geometry. The variation of the velocity from the lip to the ramp side is 4% of the mean flow speed, the different run conditions collapse to within 2% for the streamwise velocity. The v-component collapses to within 2%, shown in Figures 57(c) and (d). The w-component, given in Figure 57(e) and (f), differs by 5%. The figures show the same behavior found in the 259 scfm cases for the u, v, and w-components in the vertical traverse in the y-direction. The one percent addition is insufficient to affect the measured region. This level of mass flow addition is inadequate to overcome the momentum deficit created by the boundary layer along the ramp. The w-component in Figures 57(e) and (f) is above zero, a positive velocity exists along this centerline. This correlates with the overall positive velocity measured in the w-component along the z-centerline in Figure 56. Turbulence values were similar to those given in Figure 52 and Figure 55.

The inlet to freestream velocity ratio examinations established a few things. Near the wall a more pronounced downward flow, as a percentage of U_{av}, occurred when U_{av}/u_{∞} was increased from 3.6 to 5.4. The u and v-components in the y-direction had a gradient from the ramp to the lip. Using up to 2% of the inlet mass flow rate provided no significant changes to the flow field. Higher mass flow additions would be required for the straight step geometry. Only a small effect was possibly demonstrated in the u-component in the y-direction for the addition of flow control at 2%. The u'v' shear stress had the least noise of the shear stresses as did the u' and v'-components of the turbulent kinetic energy.

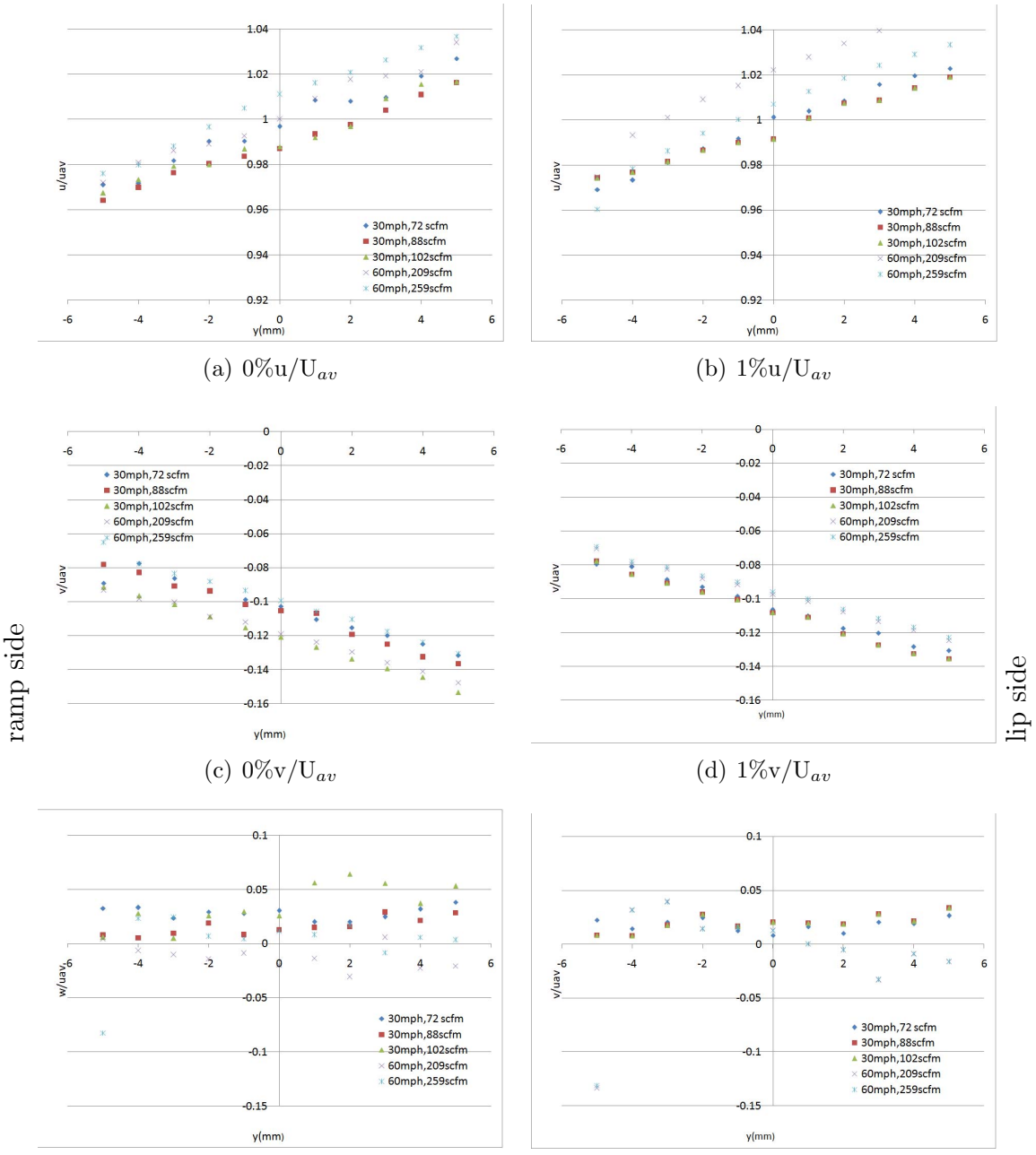

(a) 0%u/U_{av} (b) 1%u/U_{av}

(c) 0%v/U_{av} (d) 1%v/U_{av}

(e) 0%w/U_{av} (f) 1%w/U_{av}

Figure 57. Comparison of the mean velocity profiles for the 0% and 1% flow addition cases in the y-direction traverse at z=0. Refer to Table 7 for the inlet to freestream velocity ratios.

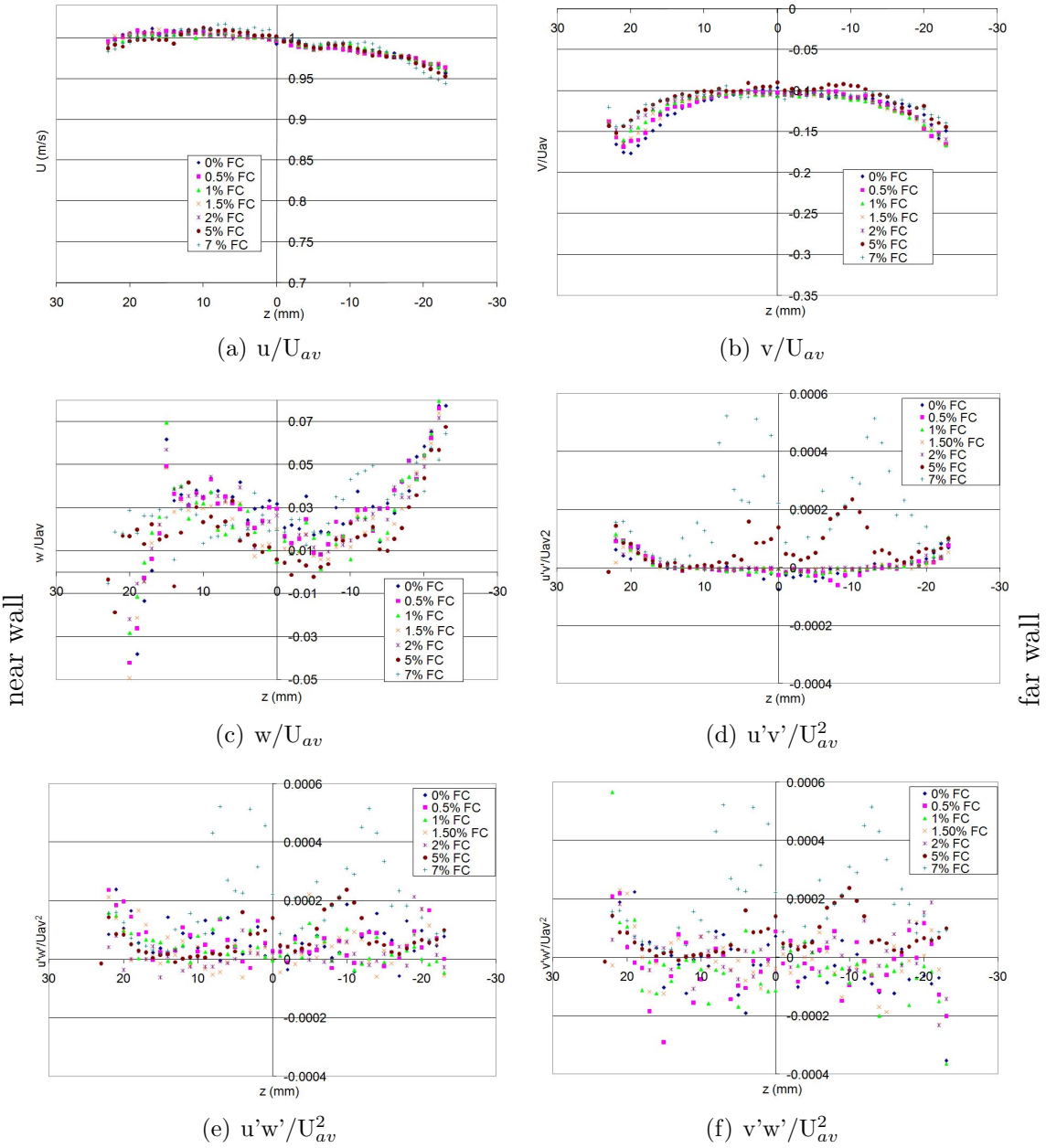

(a) u/U_{av} (b) v/U_{av}

(c) w/U_{av} (d) $u'v'/U_{av}^2$

(e) $u'w'/U_{av}^2$ (f) $v'w'/U_{av}^2$

Figure 58. Mean velocity and Reynolds shear stress components for the z-centerline, straight step configuration. Examination of flow control up to 7% at the 72 scfm case.(U_{av}/u_{∞}=3.5)

Table 8. Slope of the u-component measured in the inlet at the y-centerline.

Flow control (%)	Slope of normalized u-component
0	0.0055
0.5	0.0059
1	0.0054
1.5	0.0053
2	0.0052
5	0.0032
7	0.0015

5.1.4 Higher Mass flow addition at 72 scfm, 30 mph, Straight step configuration. The freestream and inlet flow rate examined for the remainder of the flow configuration tests was 72 scfm for 30 mph freestream velocity. Higher flow control settings of up to 7% were permitted, since 7.5% created a uniform compressor interface in RECITE.[25] The u-component trends correlate with the expected behavior for the mean velocities observed in the previous cases. The z-traverse of the u-component in Figure 58(a) collapses with marginal differences. The addition of up to 7% flow addition did not meaningfully change the results of the z-centerline streamwise flow.

The z-centerline in Figure 58 continues to support the symmetry observed for the u-component in the straight step configuration. The u-component in Figure 58(a) has the skew seen in all of the test cases. No trend shows with the addition of the flow control for the z-centerline. The higher flow control cases of five and seven percent flow addition create no difference in the u-component profile, leading to the conclusion that the flow control impacts the boundary layer region.

The v-component data given in Figure 58(b) is symmetric, having the same profile on both sides of the centerline, although lacking some of the far wall (z less than 0) region. The beam diffraction through the optical Plexiglas prevented adequate signal-to-noise ratio at the far wall. The effect of the flow control is to decrease the wall induced spillage. The downward velocity lessened with flow control, while the region at y=0 stayed the same. The w-component of the velocity shows no clear trends, as shown in Figure 58(c). The Reynolds stresses in (d)-(f) have no distinguishable

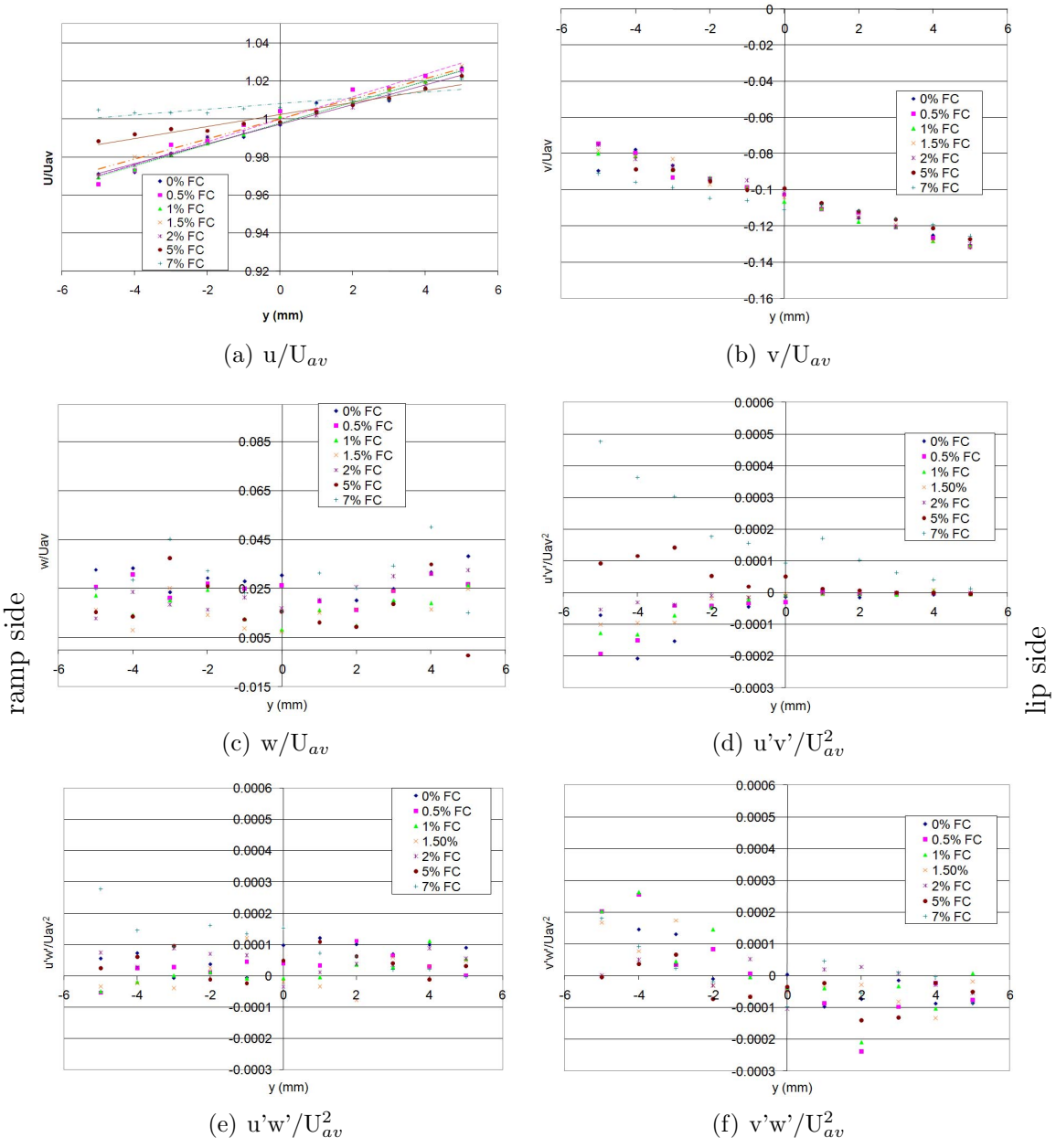

(a) u/U_{av} (b) v/U_{av}

(c) w/U_{av} (d) $u'v'/U_{av}^2$

(e) $u'w'/U_{av}^2$ (f) $v'w'/U_{av}^2$

Figure 59. Mean velocity and Reynolds stress components for the y-centerline traverse, straight step configuration. Examination of up to 7% flow control at the 72 scfm case.(U_{av}/u_∞=3.5)

behavior with increased flow control, until 5% and 7% flow addition. The increase in the Reynolds stresses are small at 5%, but visible at the 7% case for all cross component Reynolds stresses in Figures 58(d)-(f). The u'v'-component shows this effect best, due the lower noise in obtaining the u' and v'-components. The w'-component in the u'w' and the v'w'-components nearly obscures the higher levels created by the 5% flow control. The turbulence at the centerline increased from the addition of 7% mass flow, indicating mixing occurred in the submerged inlet.(61), (83), (78)

Flow control established in the straight step configuration that the flow control altered the submerged inlet's velocity profile. For the straight step geometry, the traverses along y=0 showed little effect for the mass flow addition until 5% of the main flow was added.

Smaller increments in the flow control initially provided clear resolution of the effects of the flow control. The lower flow control cases (up to 2%) were ineffective, as examined through the y-centerline in Figure 59(a). The change in the u-component with respect to y is unchanged up to this level of mass flow addition. Limited examinations for the other configurations and grid studies resulted from the lack of benefit. The 0, 2, 5, and 7 percent required investigation for the straight and fanned ramp cases while 0, 2 and 7 percent for the fanned step case. The slope change in Figure 59(a) suggested nothing gained by further examination of additions between zero and two percent. The slopes for the u-component, given in Table 8, shows the same information.

The vertical traverse at z=0 for the straight step configuration with up to 7% flow control is shown in Figure 59. The u-component, as shown in Figure 59(a), displays the same slope change in the y-centerline with the addition of flow control. The 5% and 7% flow addition continues the trend, reducing the slope of the u-component with respect to y. The u-component having less variation is desirable, as less pressure distortion exists at the throat. The u-component profile shows less variation at the

higher flow control settings (5% and 7%). The v-component in Figure 59 (b) and w-components in Figure 59(c) follow with the behavior observed in Figure 53 for the higher inlet velocities. The differences in the v-component from the top and bottom half of the inlet reduces with flow control. The w-component data has no discernable pattern with the addition of flow control.

The turbulence values in the vertical centerline traverse of the straight step configuration, shown in Figures 59(d-f), support the mixing theory. The Reynolds stresses increased in the lower half, -5 mm to 0 mm, of the traversed measurement region. The lip side halfway above the centerline, 0 mm to 5 mm, remains unchanged in the u'v'-component until the 7% case. At this value the effect of the flow control crosses the centerline to affect the entire behavior of the inlet. The v'w' and u'w' shear stresses indicated the flow control increased the energy on the ramp side of the duct, even with the higher overall turbulence in the lip side. The u'w'-component in Figure 59(e) shows an indication of higher turbulence on the ramp side, but only at the 7% flow control case at the very lower limit of the measurement region. Based upon these centerline examinations, the components to determine the effect of the flow control are the u-component and the turbulence in the contour grids. With the behavior established for the straight ramp combined with the discrete jets, the other configurations examine straight forwardly.

5.1.5 Comparison of flow control Configurations. The results of the centerline traverses for each of the four geometries are given for the u-component in the z-direction for y=0 is given in Figure 60. The linear study for the y-direction at z=0 is shown in Figure 61 for the u-component of the velocity. Some variation occurred in the u-component, a slight decrease in velocity at the far wall for the 2% and zero flow control cases. The difference is the behavior for the fanned step in the near wall region(23 to 0 mm). The fanned step and fanned ramp at the 7% mass flow in the near wall region has higher velocities in the near wall region (z=23 mm) towards the center and then returning to the pre-described behavior of the lower flow control cases. The

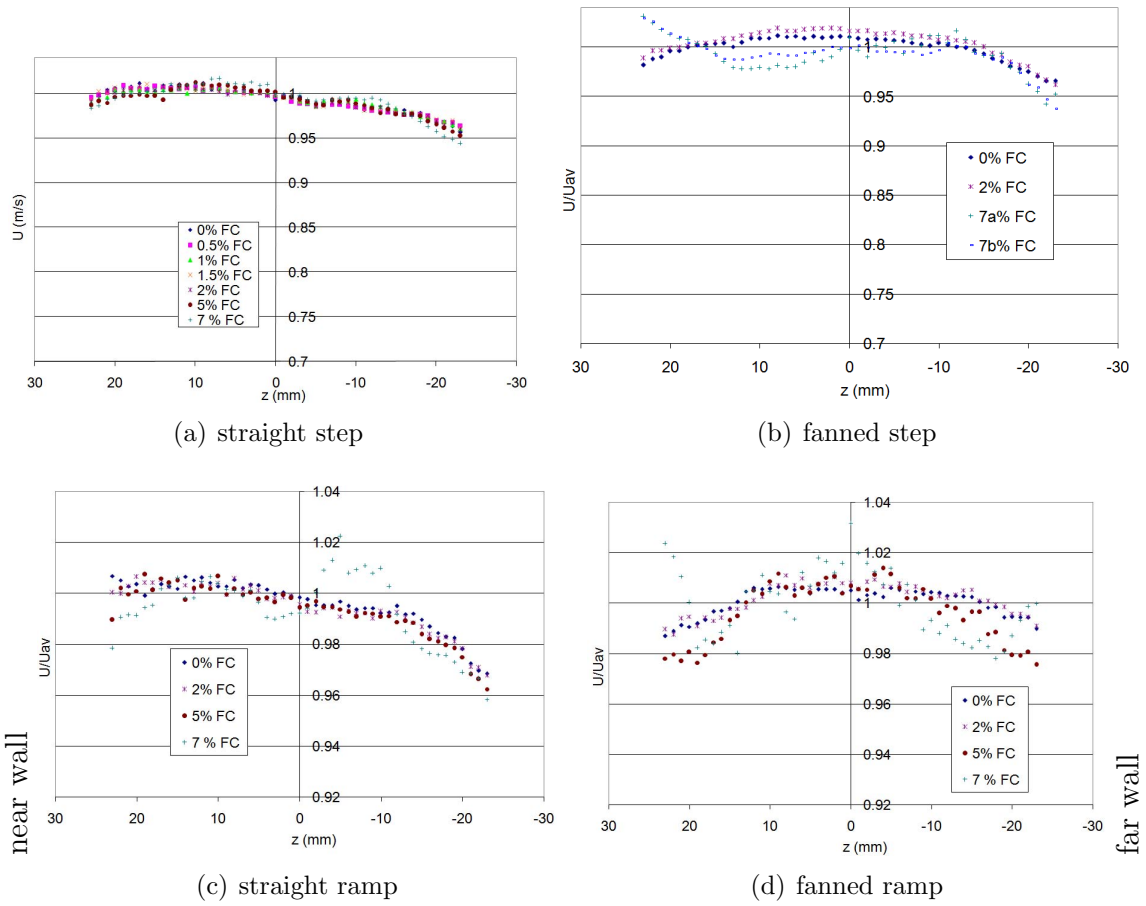

(a) straight step

(b) fanned step

(c) straight ramp

(d) fanned ramp

Figure 60. Streamwise velocity in z-direction linear traverse for the four flow control configurations normalized by the U_{av}. (U_{av}/u_{∞}=3.5)

centerline experiences possible attenuation from the flow control. The seven percent cases in the fanned configurations produced greater influence on the flow than the straight configurations. The behavior was confirmed, as shown by the repeated run in Figure 60(b). This same phenomena appeared in the fanned ramp, given in Figure 60(d), but is not evident in the straight flow control jets. The behavior occurs at 7% mass flow addition with the angled jets. The differences become exaggerated by the scale chosen to differentiate the mass flow additions' behavior.

The y centerline data, shown in Figure 61, provides good insight into the effect of the flow control. In all cases increased flow control flattens the streamwise velocity profile. For both the straight step and the fanned step configurations there is only

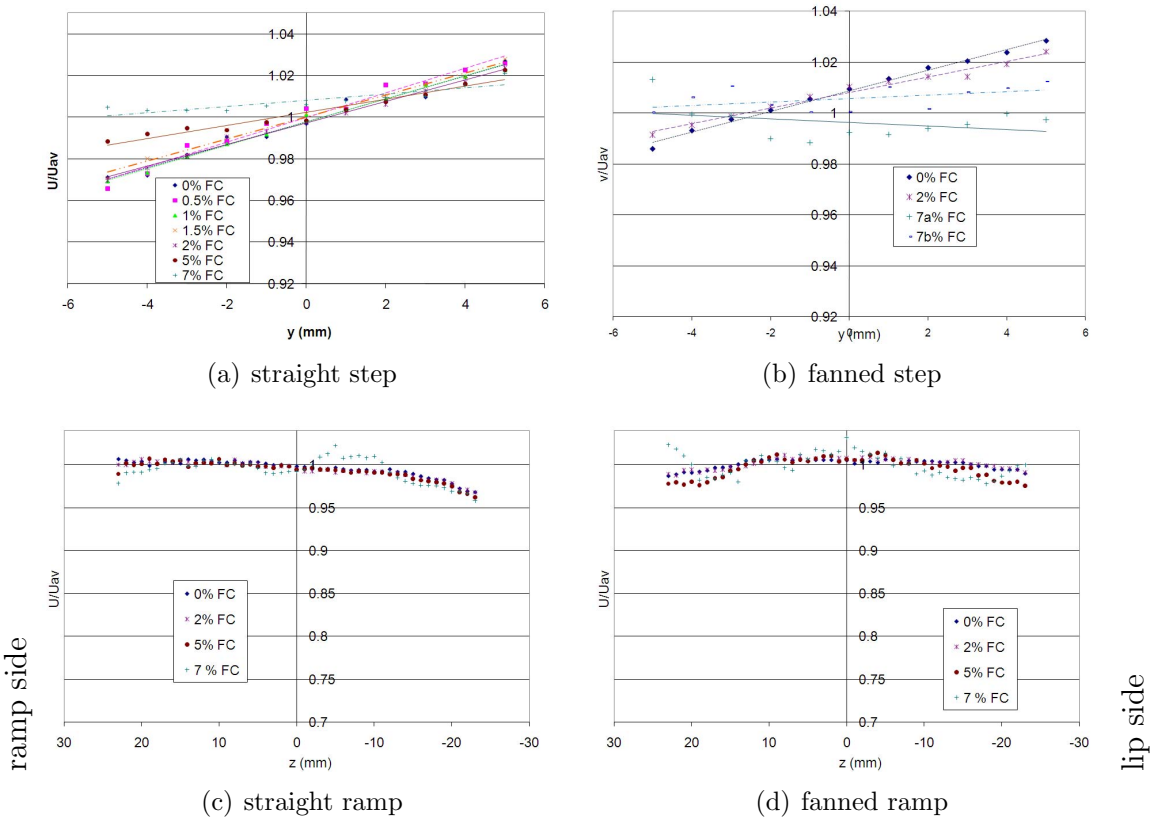

(a) straight step

(b) fanned step

(c) straight ramp

(d) fanned ramp

Figure 61. Streamwise velocity in the y-direction linear traverse for the four flow control configurations. (U_{av}/u_{∞}=3.5)

Table 9. Slope of the u-component measured in the inlet at the y-centerline for the four configurations.

Flow control (%)	Straight step	Fanned Step	Straight ramp	Fanned Ramp
0	0.0055	0.0041	0.0041	0.0040
0.5	0.0059	-	-	-
1	0.0054	-	-	-
1.5	0.0053	-	-	
2	0.0052	0.0030	0.0036	0.0038
5	0.0032	-	0.0031	-0.0003
7	0.0015	±0.0007	-0.0010	-0.0013

marginal improvement between the 0% and 2% mass flow addition. The 5% addition for the straight step clearly flattens the profile and the 7% addition continues the trend. The 5% mass flow addition was not performed for the fanned step case since flow uniformity was not expected. Both the straight ramp and the fanned ramp configurations exhibit a change in the slope, for the 5% flow control addition cases. The slope of the u-component lines are zero at the 7% mass flow. The negative sign in the slope indicates too much mass flow addition. The higher velocity located along the ramp instead of the lip side of the inlet indicates an excess of momentum. In the fanned ramp configuration, the 5% mass flow leads to nearly zero slope indicating the flow is uniform. The slopes of the best linear fit of the data are given in Table 9. The data for the 0 to 2% cases are different than those in Table 6 since the freestream velocity and inlet mass flow rate. The data is the same as that displayed in Table 8 for the straight step configuration and is repeated for comparison to the other configurations.

The range of the flow speeds and inlet speeds examined collapsed with the average streamwise velocity at the throat. The low flow control settings of less than 5% were ineffective in altering the flow, as shown in the z and y-direction line studies. At 5% flow control addition differences in the profile demonstrated in the y-direction centerline traverse, particularly for the fanned ramp geometry. The data for the z-traverses, y=0 mm, did not show much difference between the four geometries tested. The trends for the secondary flow components v and w as well as the Reynolds

stresses u', v', w' and u'v', u'w' and v'w' all follow trends seen for the straight step configuration and were therefore not repeated here.

5.2 Half Plane Examination of the Different Flow Control Configurations

5.2.1 Straight Step Zero Mass Addition. Data was acquired for each each of the four geometries using grids extending over one half of the throat region. The mean velocity components for the baseline condition for the straight step geometry are given in Figure 62. The u-component has a corner deficit and is marked by a gradual increase from the ramp to the lip in the measurement region. The higher velocities concentrated at the lip side, as expected from flow acceleration around the lip.[10] This behavior agrees with the linear traverses. The profile is uniform in the z-direction, but is not uniform in the y-direction due to slower flow near the ramp. The v-component reflects a larger downward component at the lip side of the throat with less downward motion near the ramp. The profile along the z-direction is uniform near z=0 with increased velocities near the wall. The w-component has a positive value ($\sim 0.05 U_{av}$) at z=0 with the flow transitioning to the opposite direction at the wall (23 mm to 17 mm). This positive velocity existed in the linear traverses with the same profile behavior along the y and z-centerlines. The flow behavior for all three components holds for all of the flow control cases and flow control configurations. Most notable in the v-component is the large downward component in proximity to the sidewall. This region corresponds to a larger u-component at the lip and a region of lower velocity near the ramp.

The velocity fluctuations u', v' and w' in the baseline condition for the straight step configuration is given in Figure 63. Except for the near wall region, the fluctuations in the u-component and v-component are near $0.02 U_{av}$ over the measurement region. Changes in the turbulence occurring as it enters the inlet are small, the freestream intensity falls near the level of $0.02 U_{av}$. The v'-component shows an increase near the sidewall, which is consistent with boundary layer growth, and along

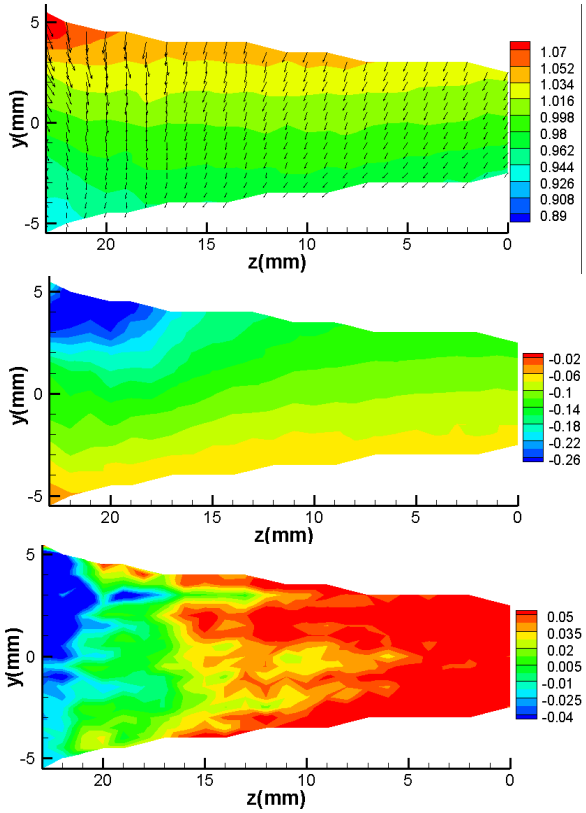

Figure 62. Mean velocity components for the straight step configuration without flow control. The the u/U_{av} (top), v/U_{av}(center) and w/U_{av} (bottom) velocities. (U_{av}/u_{∞}=3.5)

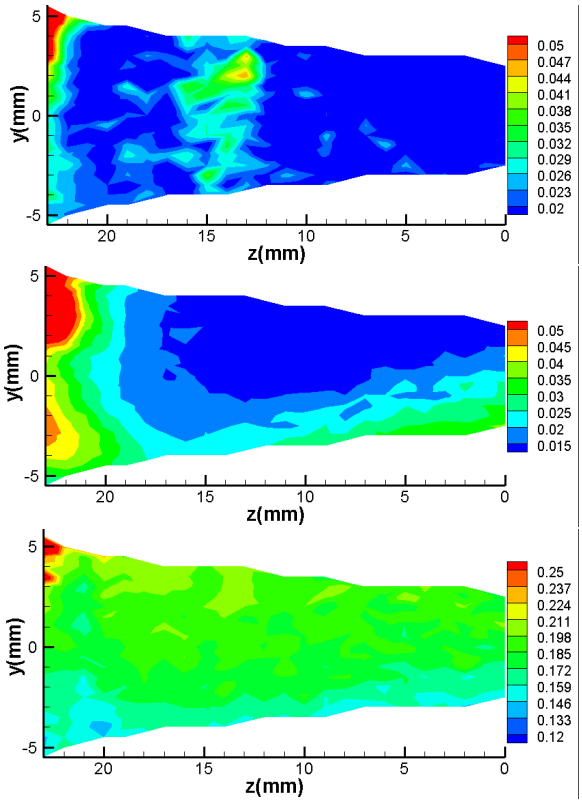

Figure 63. RMS velocity components for the straight step configuration without flow control, the u'/U_{av}, v'/U_{av} and w'/U_{av} fluctuating velocities are in descending order. (U_{av}/u_{∞}=3.5)

the ramp where the boundary layer and the spillage over the side wall affect the flow. The w'-component is relatively uniform over the entire grid, aside from the range. The magnitude of the w'-component is five times larger than the u' and v'-components. The w'-component being significantly higher than the u' and v'-components display the difficulty in obtaining the w-component.

The Reynolds shear stresses are shown in Figure 64. The Reynolds shear stresses further confirm that quantitative measurements with the w-component are not reliable.[93],[98] The energy content in the Reynolds stresses is low and only active in the shear layer regions in the combination of the u and v-components. The u'w' and v'w' were shown for completeness. The u'v'-component is the most reliable measurement.[93],[98] The u'v'-component has a high energy region located at the lip and wall juncture, but is otherwise essentially uniform. Lower turbulence levels

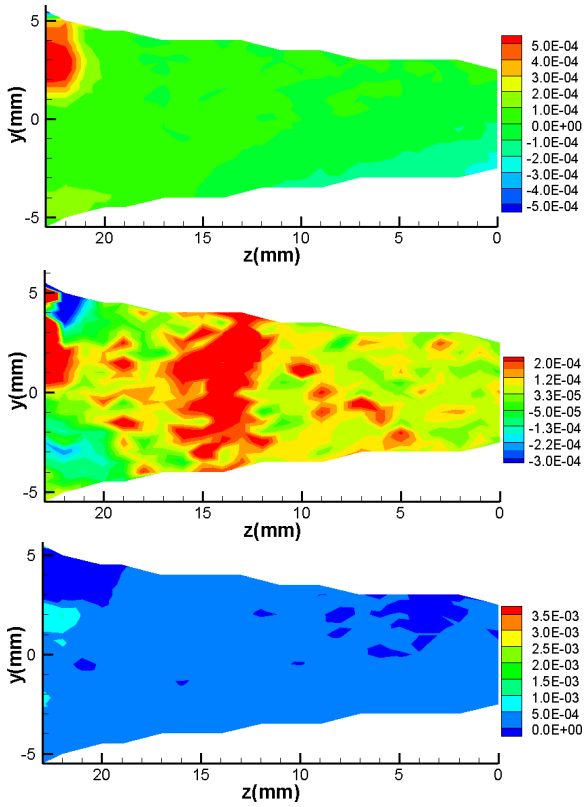

Figure 64. Reynolds shear stresses for the straight step configuration without flow control. The u'v'/U_{av}^2, u'w'/U_{av}^2 and v'w'/U_{av}^2 components are in descending order. (U_{av}/u_∞=3.5)

manifest near the ramp indicating flow activity. The u'w' has a complicated result not aided by the difficulty in obtaining the w'-component. The v'w'-component is a full magnitude higher in range.

These measurements of the baseline geometry match well with the linear centerline traverses from Figures 58 through 59. A gradient exists at the z=0 location for the u and v-components. The magnitudes of the velocities are of the same range and value. The y=0 location correlates, the u and v-profiles are relatively uniform with decreasing velocities at the wall. The turbulent kinetic energy components realized by the u' and v'-components, the w' is larger in magnitude. An increase in turbulent kinetic energy occurred at the wall and near the ramp for the u' and v'-components. The measurement errors dominate u'w' and v'w' shear stresses, scattered and higher in general compared to the u'v'-component. The u'v'-component agrees with the lin-

ear studies in that there are low levels of turbulence and is relatively uniform along both the y=0 and z=0 lines.

The u-component is representative of the total pressure at the throat, which determines of the uniformity of the incoming flow. The u'v' Reynolds stress determines the effect created by the mixing and the momentum and energy addition. The flow vectors represented the secondary flow features created by the v and w-components on the u-component in all figures. The flow vectors have the same scale, direct comparison possible between figures. The v-component reacted similar to the u, with less pronounced effects in the linear traverse. The u' and v'-components differentiate the flow control effects in addition to the u'v'-component. Establishment of the baseline flow allows comparison of the flow control effects.

5.2.2 Comparison of Zero Mass Addition Configurations. The mean streamwise velocity and u'v'-component of the Reynolds stress are indicators of the flow control jets' effectiveness. In these experiments there were small changes in the geometry, such as the addition of the step well upstream of the throat, of the inlet mandated by the addition of the flow control. The baseline case for all of the geometries as given in Figure 65. Despite these small geometry changes only small differences were generated between the flow control configurations. Slight differences exist in the deficit at the ramp-sidewall juncture. The high velocities from the induced spillage are essentially the same. None of the secondary flow vector overlays in Figures 65 displayed any indication of the roll up vortex predicted from the wall spillage per Figure 2.[3] The plausible explanation is the inlet flow velocity was large compared to the freestream velocity. The inlet velocity is normally close to that of the freestream velocity. The ratio is over three times greater in these examinations.

The vorticity for a ramp and step configuration are shown in Figure 66. The vorticity near the lip-sidewall juncture in Figure 66 has a region of negative value indicative of the downward flow and the resulting boundary layer.[3],[13],[12] No discrete vortex was detected in the calculations as expected from literature as given in

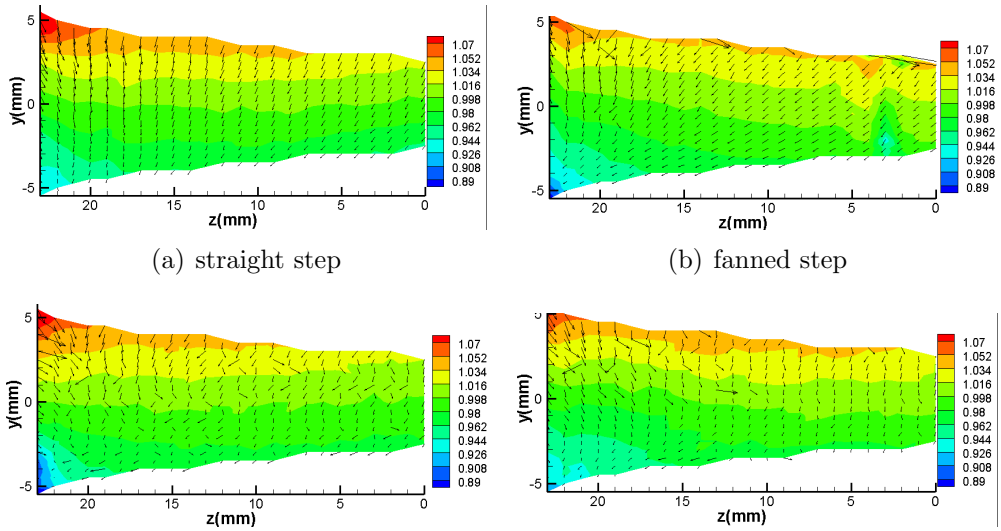

(a) straight step (b) fanned step

(c) straight ramp (d) fanned ramp

Figure 65. The four flow control configuration's streamwise velocity profiles with 0m_r addition. (U_{av}/u_∞=3.57 for the straight step, 3.70 for the fanned step, 3.76 for the straight ramp and 3.64 for the fanned ramp.)

Figure 2.[3] The presence of the step had a small effect on the downward flow, since only one large negative vorticity region formed in the top half of the inlet. Without the step, the low region of vorticity extended further into the inlet, down to the ramp corner.

No significant differences existed between the baseline profiles for each flow control configuration. The natural evolution of the flow obscured the presence or absence of the step. The absence of the wall vortices shows in the vortex plots in addition to the secondary flow pattern.

5.2.3 Straight Step Mass Flow Addition. The addition of flow control now displays the changes to the inlet profile established by the prior grid examinations. Figure 67 shows the behavior of the straight step configuration with the addition of flow control. The u-component is on the left and the u'v'-component of the Reynolds shear stress is on the right. The addition of flow control decreased the maximum u-component at the lip of the inlet. The ramp corner low regions' area increased slightly. The velocity along the ramp from 19 to 0 mm increased, displaying the effect of the

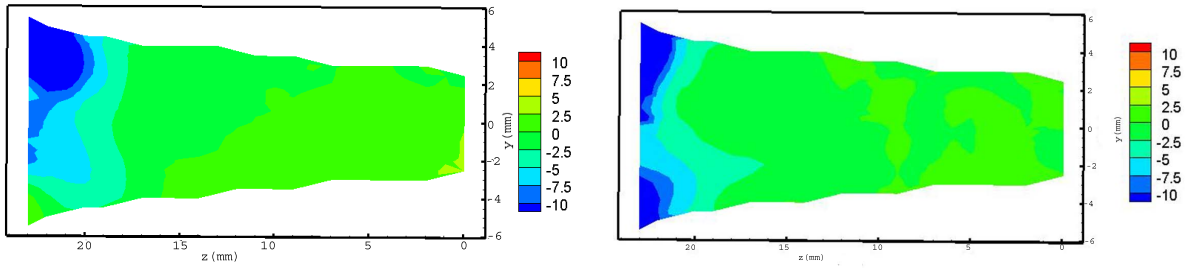

(a) step (b) ramp

Figure 66. Vorticity for the zero flow control cases for the ramp and step configurations. (U_{av}/u_∞=3.58 for the step configuration shown and 3.76 for the ramp configuration.)

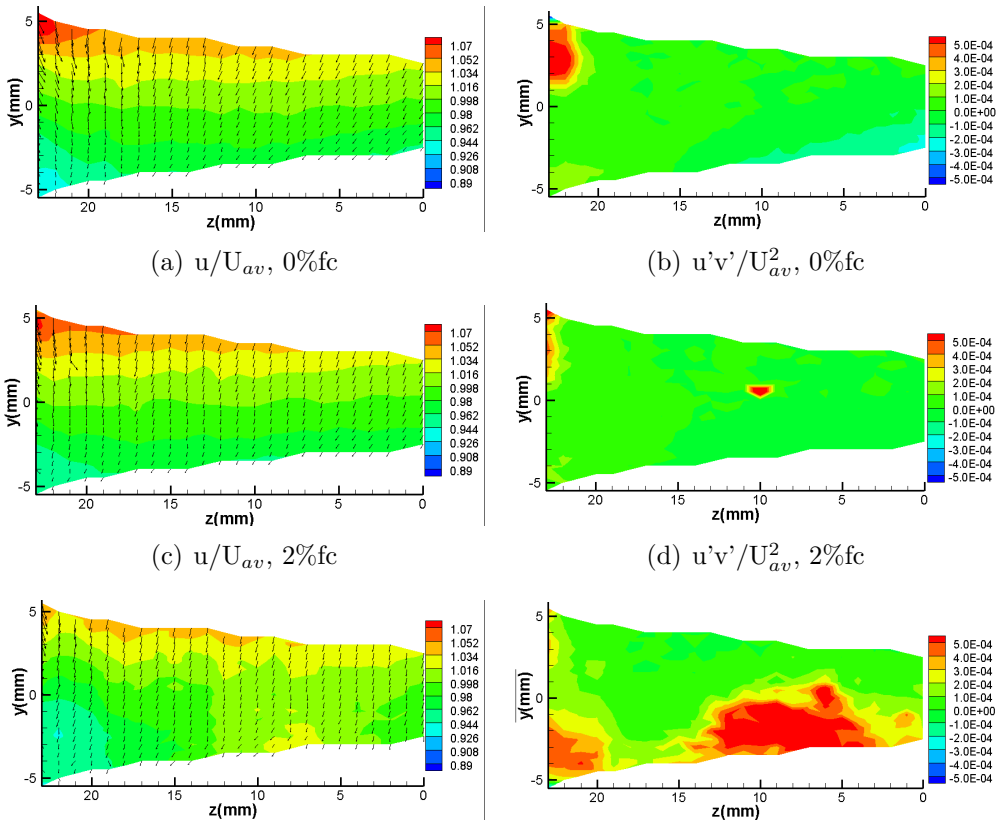

(a) u/U_{av}, 0%fc (b) $u'v'/U_{av}^2$, 0%fc

(c) u/U_{av}, 2%fc (d) $u'v'/U_{av}^2$, 2%fc

(e) u/U_{av}, 7%fc (f) $u'v'/U_{av}^2$, 7%fc

Figure 67. Mean velocity component and u'v'-component of the Reynolds stress with flow control (fc) addition for the Straight step configuration. (U_{av}/u_∞=3.57)

flow control upon the velocity deficit created by the boundary layer. The decrease in the overall range of the u-component represents the flow control's effect towards uniform flow.

The u'v' data confirms that the flow control jets affect the inlet, as shown in Figure 67. The 2% mass flow addition reduced the high energy region at the wall, the flow control counteracts the downward effect of the velocity spillage over the wall. The region of negative u'v', which is consistent with expectations in a boundary layer, evident at the center of the measurement region with 2% addition in Figure 67(d). The 7% mass flow case shows that the Reynolds stresses increased because of mass flow addition. With sufficiently high mass addition the jets induce mixing and turbulence that persists to the throat. The energy provided by the flow control for the straight step configuration reaches the throat inducing mixing which ultimately led to a more uniform profile. The pocketed regions of high u'v' suggest that the jet turbulence might be concentrated in specific locations, instead of distributing over the span of the inlet, over the z-direction.

The u' and v'-components display the constituent effects of the flow control. These two turbulent kinetic energy components for the straight step configuration are shown in Figure 68 for 0%, 2% and 7% mass flow addition. The fluctuations are highest at the wall with the flow control affecting the area and magnitude of the fluctuations. Higher fluctuations at the wall are consistent with boundary layer shearing. The u'-component is quieter than the v'-component for the 7% addition case. If anything, two percent mass addition actually appeared to reduce the value of u' and v' fluctuations in Figure 68(c) and (d). The same behavior hold for the v'-component in Figure 68(d) in reducing the magnitude at the ramp wall. The flow control of 2% has a noticeable effect in the fluctuating components in reducing the magnitude of the fluctuations from the incoming wall flow. At 7% the energy increased at the ramp with more fluctuations occurring in this half of the measured grid. The entire region was affected in the v'-component fluctuations, more so than the u'-component.

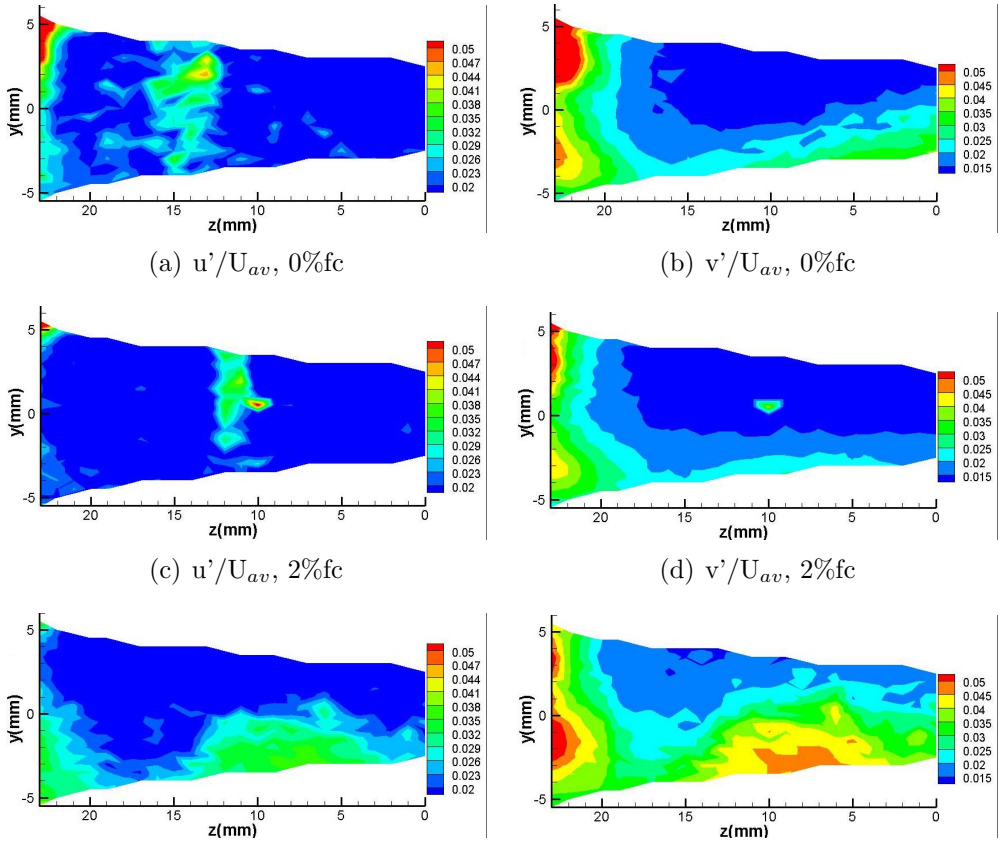

(a) u'/U_{av}, 0%fc

(b) v'/U_{av}, 0%fc

(c) u'/U_{av}, 2%fc

(d) v'/U_{av}, 2%fc

(e) u'/U_{av}, 7%fc

(f) v'/U_{av}, 7%fc

Figure 68. Turbulent kinetic energy components with flow control for the straight step configuration.

To summarize, the 7% mass flow addition led to flow uniformity for the straight step configuration. The u'v'-component measurements indicated the mixing within the inlet. The changes were gradual until the mass flow overcame the boundary layer deficit. The u' and v'-components reacted to milder additions, showing a small effect at the 2% flow control while the u'v'-component remained essentially unchanged. The examination of both the u' and v' constituent components enabled quicker verification of the net effect of the flow control.

5.2.4 Fanned Step Mass Flow Addition. The results for the fanned step configuration with flow control are examined in Figure 69. The difference from this configuration to the straight step is the outward flaring of the jets from the center at increasing increments of three degrees. The outer most jets had an angle of nine degrees relative to the freestream in the spanwise direction. The directed flow targeted the deficit in the corner region, where the ramp and sidewall meet. The deficit in the y=-5 mm to 0 mm and z=23 mm to 20 mm changes because of the directed jets. The deficit vanishes from the corner at the 7% mass flow and the rest of the inlet experiences a decrease in the observed range of the u-component.

The u'v' turbulence was relatively quiet, with none of the effects of the flow control evident for the 2% case. The turbulence levels increased sharply for the 7% mass flow case as shown in Figure 69(f). The fanned step configuration evinced a strong negative u'v' near the ramp side corner. A portion of the high energy turbulence lifted off the ramp and resided at the wall in the upper half of the inlet. Rather than a continuous band of energy along the ramp, the step configurations formed discrete pockets of higher energy from the jets similar to the slower mixing cases in Glawe.[84] The energy in the u'v'-component of the 7% was distributed unevenly over the entire ramp. Higher energy localized in the center of the inlet near z=0 mm to 5 mm for y less than zero and another region in the z=15-23 mm in the region of y=-1 mm to 5 mm in the inlet. The u-component changed in a beneficial manner with the 7% addition, decreasing the velocity variation despite the

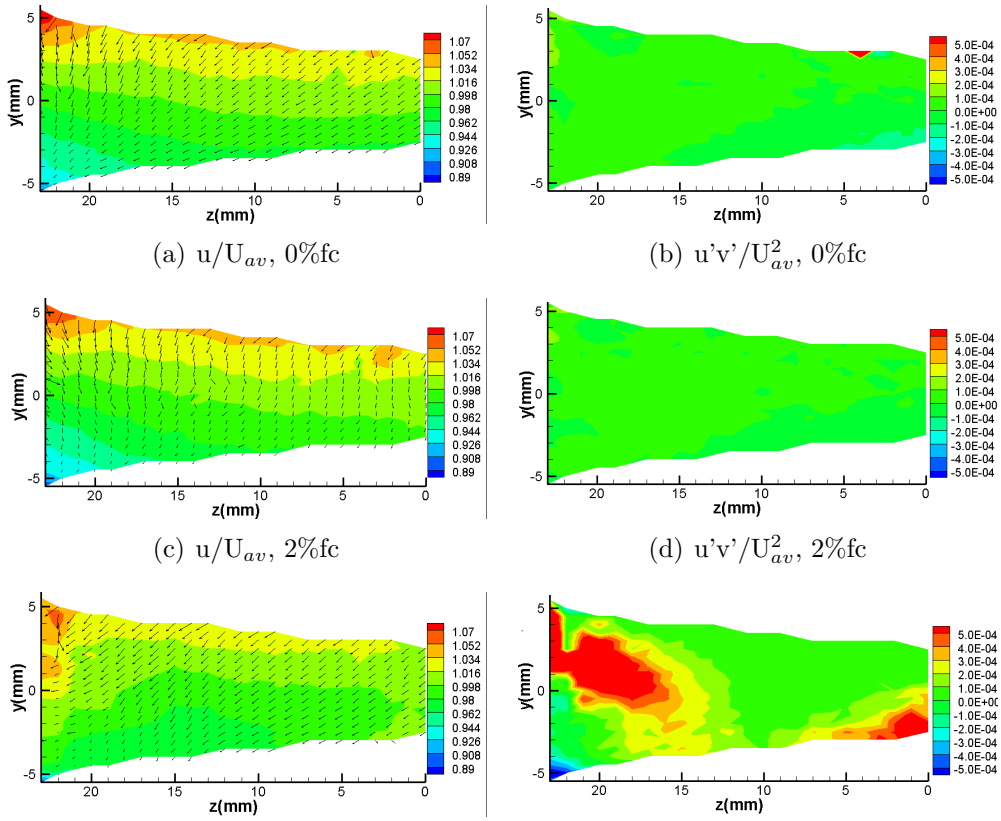

(a) u/U_{av}, 0%fc (b) $u'v'/U_{av}^2$, 0%fc

(c) u/U_{av}, 2%fc (d) $u'v'/U_{av}^2$, 2%fc

(e) u/U_{av}, 7%fc (f) $u'v'/U_{av}^2$, 7%fc

Figure 69. Mean streamwise components with the addition of flow control for the fanned step configuration and u'v' Reynolds shear stress. (U_{av}/u_∞=3.70)

non-uniform distribution of the shear stresses.[39] Isolation of the turbulence aided by the step is verified by the examination of the ramp profile.

The u' and v'-components of the turbulent kinetic energy for the fanned step configuration are given in Figure 70. The 0% mass flow addition profile is cleaner than the straight step. The profiles are similar to the straight step with milder fluctuations. The two percent addition in the u'-component displays no change from the 0% addition case and the same holds for the v'-component. The effect of the flow control on the turbulence appears at 7% mass flow addition for both the u' and v'-components in Figure 70. The energy focused at the wall with mild effects near the ramp. The straight step configuration in Figure 68 had concentrated turbulent energy near the ramp rather than at the sidewall. The inlet had a streamwise velocity deficit

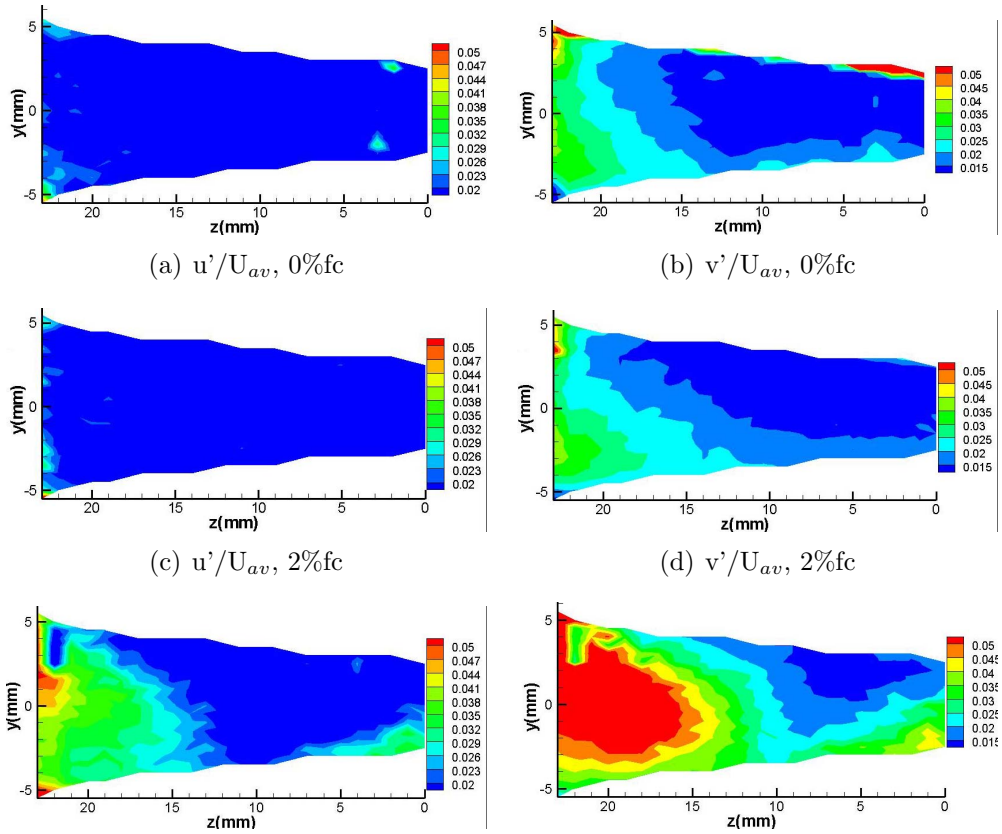

(a) u'/U_{av}, 0%fc (b) v'/U_{av}, 0%fc

(c) u'/U_{av}, 2%fc (d) v'/U_{av}, 2%fc

(e) u'/U_{av}, 7%fc (f) v'/U_{av}, 7%fc

Figure 70. Turbulent kinetic energy components u' and v' with flow control addition for the fanned step configuration. (U_{av}/u_{∞}=3.70)

at the wall-ramp corner, the energy content being higher in the u' and v'-components demonstrates that directing the jets at the wall promoted flow to this region. The magnitudes of the fluctuations for this configuration are higher at the sidewall than for the straight step configuration.

The addition of a secondary component directed the flow toward the wall, which helped eliminate the ramp-wall velocity deficit. Seven percent mass flow addition achieved good flow uniformity by reducing the overall u-component variation. The jet interaction created coherent regions of u'v', rather than developing a fully uniform distribution. Reduction of the mass flow quantity remained nearly unchanged from the RECITE slot configuration (7.0% vs. 7.5 The investigation of flow control implementation within the ramp was driven by the hypothesis that energizing the

boundary layer closer to the throat would lead to a reduction in the percentage of mass flow addition required to achieve uniformity.

5.2.5 Straight Ramp Mass Flow Addition. The ramp flow control configurations reset the boundary layer closer to the inlet. The flow control configuration positioned closer to the inlet on the ramp surface introduced a cross-flow component to the entering flow control jets. The results of the measurements for the straight ramp flow control configuration are given in Figure 71. The 5% flow control setting affects the corner deficit in the u-component. The ramp-sidewall deficit is essentially gone with the deficit increasing from $0.89U_{av}$ to $0.944U_{av}$. Additionally, the region covered by flow greater than $1.0U_{av}$ has reduced slightly. The region covered by maximum value at the sidewall and lip reduces significantly with the 7% mass addition. The magnitude of the u-component of the velocity decreased with the addition of flow control, as occurred with the step configurations. The 7% addition shows that the velocity along the ramp and exceeds the amount necessary to obtain flow uniformity. The range in the u-component throughout the plane decreases from 0.89 to $1.07U_{av}$ at 0% to 0.96 to $1.07U_{av}$. The region along the ramp in the 7% flow control case increased to $1.03U_{av}$ from $0.96U_{av}$ due to the mass flow addition.

The energy content changed with the addition of flow control. The u'v'-component displays a negative shear stress near the corner ramp-sidewall juncture, which is eliminated by the 5% flow control addition, as shown in Figure 71(f). The 5% addition led to positive values for u'v' for the y less than -2 mm for the entire width of the measured region. The energy uniformly distributed over ramp side of the inlet at a value of $3.0e^{-4}U_{av}^2$ for the 5% flow control. The 7% case, shown in Figure 71(h), has a stronger u'v' presence than that of the 5% m_r with a magnitude of $5.0E^{-4}U_{av}^2$.

The straight ramp configuration results for u' and v' are given in Figure 72. Overall the trends are similar to the behavior of the u'v'-component of the turbulence. There is little difference between the 0% addition and the two percent addition cases. The similarity indicated that the flow control at 2% mass addition is insufficient to

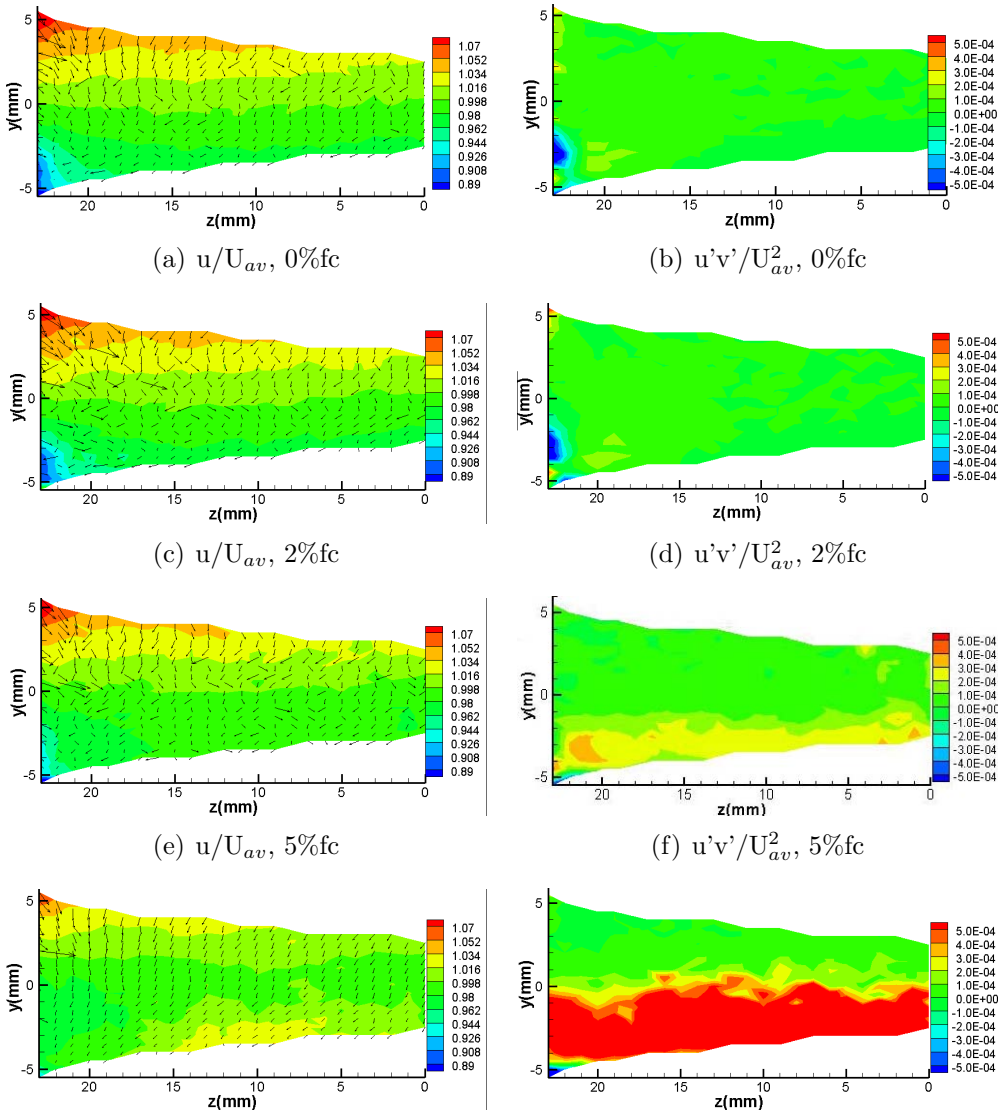

(a) u/U_{av}, 0%fc

(b) $u'v'/U_{av}^2$, 0%fc

(c) u/U_{av}, 2%fc

(d) $u'v'/U_{av}^2$, 2%fc

(e) u/U_{av}, 5%fc

(f) $u'v'/U_{av}^2$, 5%fc

(g) u/U_{av}, 7%fc

(h) $u'v'/U_{av}^2$, 7%fc

Figure 71. Mean streamwise component and u'v' Reynolds stress with flow control addition for the straight ramp configuration. (U_{av}/u_∞=3.76)

alter in the inlet profile. The 5% m_r in the u'-component evidences high values along the ramp as shown in Figure 72(e). The same holds for the v'-component at 5% addition, as increased values exist near the ramp. Both the u' and v'-components display a spanwise uniform area of fluctuations where the jets mixed near the ramp, as shown in Figure 72(g) and (h). The v'-component has energy content added to the entire throat, while the u'-component remains mostly unaffected in the upper half of the inlet even at 7%.

Implementing flow control using the straight ramp geometry led to a decrease in the level of mass flow addition required to achieve uniformity in the streamwise velocity. The corner velocity deficit reduction with 5% addition of the flow control compared closely to the 7% addition required for the step configurations. The 5% addition led to an even distribution over the ramp surface for the u'v'-component. Seven percent added a slight momentum excess to the system for the ramp geometry. The secondary flow in the straight ramp configuration remained small for this configuration as shown by the vectors overlaid on the u-component.

5.2.6 Fanned Ramp Mass Flow Addition. Figure 73 shows the results for the fanned ramp configuration and the effects of the flow control on the u-component and the u'v'-component of the turbulence. The u-component decreases significantly near the lip and sidewall junction of the inlet with the addition of 5% and 7% addition flow control. As noted in the other configurations, the 2% mass flow addition profile was essentially unchanged. None of the excessive streamwise velocity remained along the lip at the 7% flow control addition. The corner deficit was eliminated by a 5% addition. The 7% mass flow addition increased the velocity along the ramp region above a u/U_{av}=1.0, signifying too much mass flow addition to the inlet throat. The excess velocity was anticipated from the straight ramp configuration in Figure 71(g). The higher velocity seen at the centerline for the fanned ramp configuration also indicated over blowing. The highest value seen in the straight ramp configuration was $1.05U_{av}$ compared to $1.01U_{av}$ for the fanned ramp geometry at the lip. The

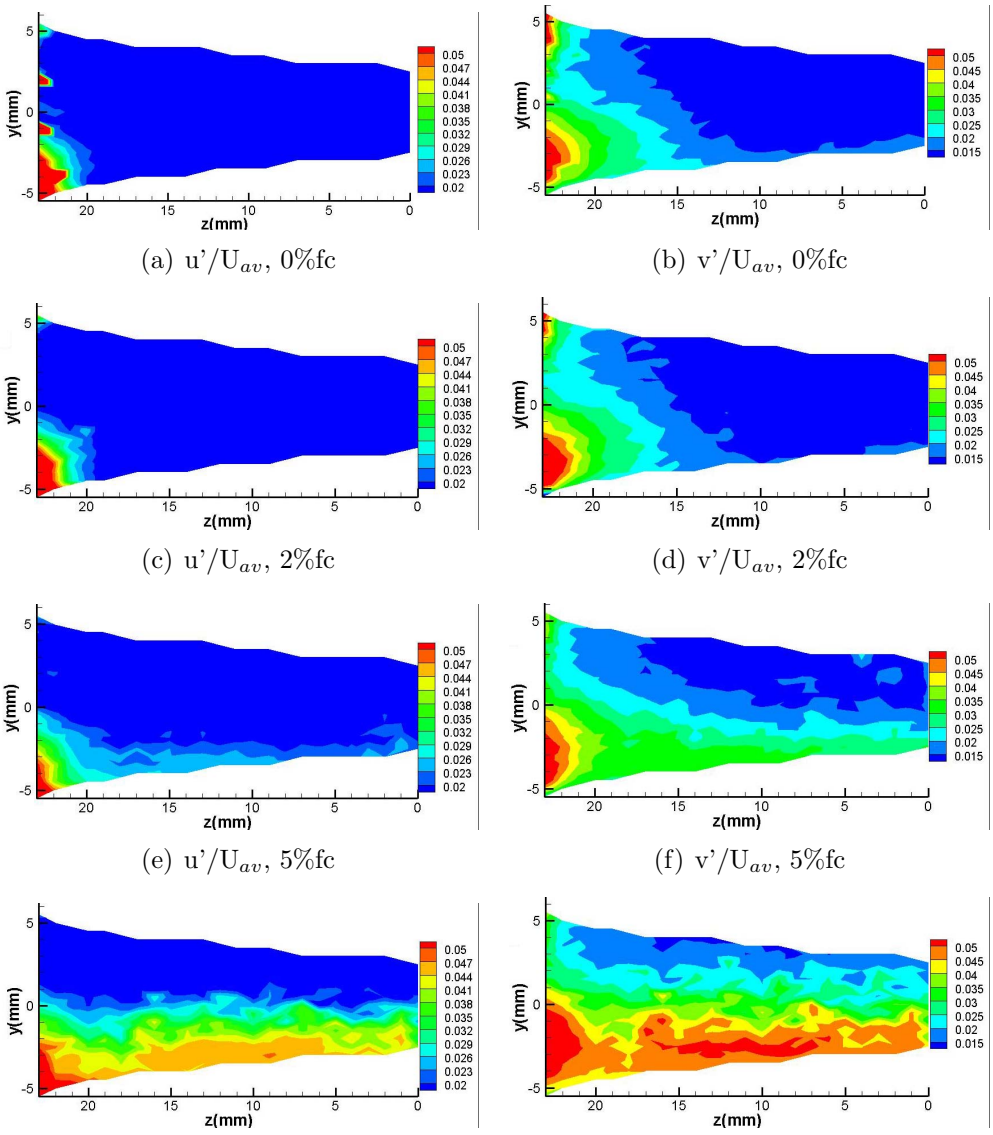

(a) u'/U_{av}, 0%fc (b) v'/U_{av}, 0%fc

(c) u'/U_{av}, 2%fc (d) v'/U_{av}, 2%fc

(e) u'/U_{av}, 5%fc (f) v'/U_{av}, 5%fc

(g) u'/U_{av}, 7%fc (h) v'/U_{av}, 7%fc

Figure 72. Turbulent kinetic energy components u' and v' with flow addition for the straight ramp configuration. (U_{av}/u_{∞}=3.76)

excess velocity along the ramp for the fanned ramp geometry in the 7% case means that the 5% mass flow is more uniform due to having a larger region of U_{av}=1.0.

The effect of angling the jets is more prominent in the u'v' turbulence in Figure 73. The 2% flow control addition evidenced the jets presence, specifically in the ramp-sidewall juncture region, unlike the other flow control configurations. The 2% flow control has more turbulent energy there than that of the zero mass addition case in Figure 73(b). The energy directed at the wall had some effect on the mean streamwise velocity, as seen by the decrease in the u-component corner deficit's magnitude and area. The momentum is higher along the sidewall and more uniformly spread over the remaining area of the inlet for y less than 0 mm for the five and seven percent additions. The magnitude of u'v' is low in the 5 to 10 mm region of the z-direction for the 5% case, unlike the straight ramp configuration which was uniform. The largest values of u'v' was $3.0E^{-4}U_{av}^2$ compared to $5.0e^{-4}U_{av}^2$ along the rest of the ramp. The increased distance between the jet cores might be expected to create a region of lower energy compared to the ramp corner region. The u'v' magnitude is higher at 5% mass flow addition for the fanned ramp configuration than for the 5% addition in the straight ramp configuration. This difference is no longer evidenced at 7%addition. The secondary motions for this configuration were weaker than those of the step configuration. The spanwise component in the z-direction is nearly twice as strong in the fanned step configuration as it is in the fanned ramp configuration. The turbulence, in general, is uniform deviating only in the presence of flow mixing.

The u' and v'-component values for the fanned ramp flow control geometry are shown in Figure 74. There are some differences between the two percent mass addition and zero mass addition cases, though they are not as significant as the near complete loss of the wall fluctuations presented in Figure 68. As predicted from the u'v'- component results and the other configurations, the fluctuations for the u' and v'-components are greater near the wall. The proximity of the blowing to the throat increased the strength of the fluctuations and turbulence. The jets angled towards the wall increased the energy at the wall. The profile of the 5% mass addition in

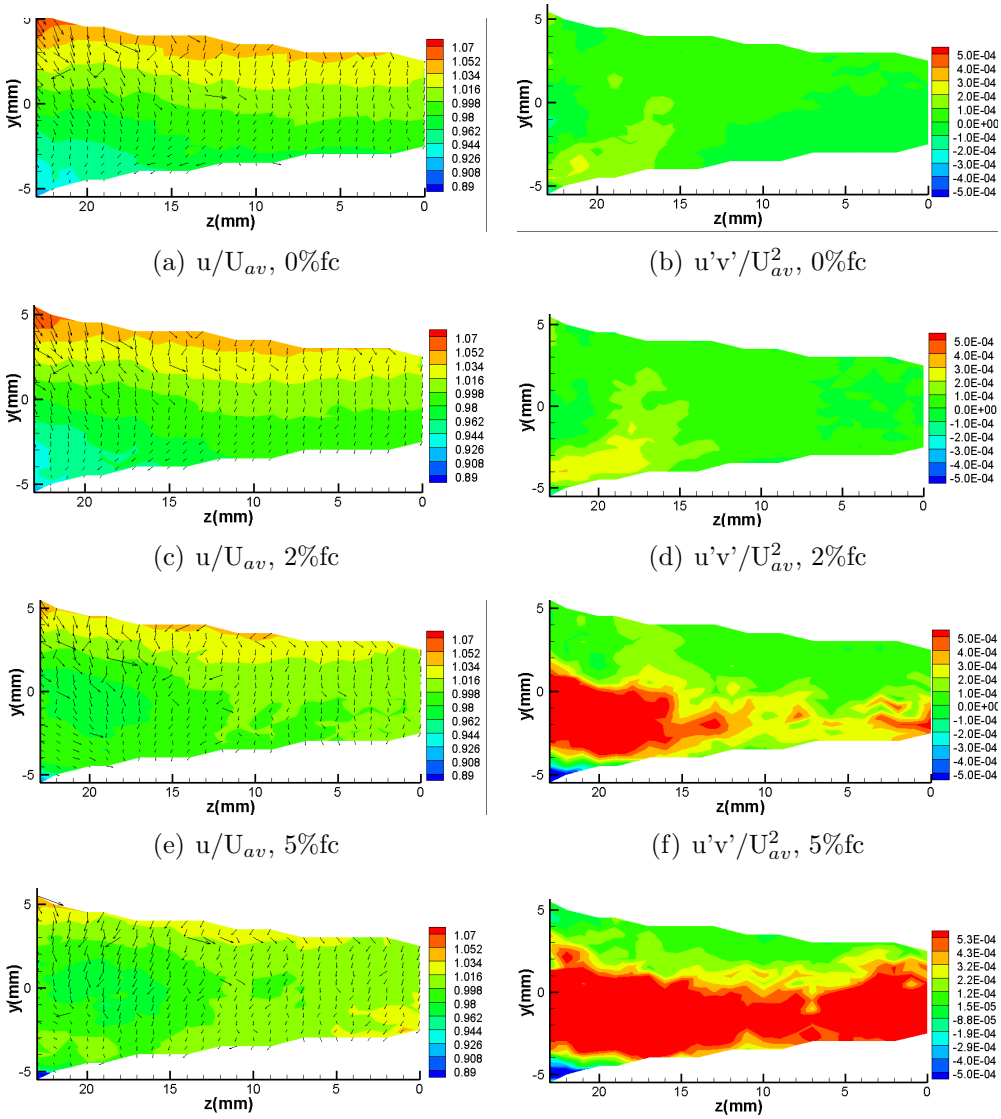

(a) u/U_{av}, 0%fc (b) $u'v'/U_{av}^2$, 0%fc

(c) u/U_{av}, 2%fc (d) $u'v'/U_{av}^2$, 2%fc

(e) u/U_{av}, 5%fc (f) $u'v'/U_{av}^2$, 5%fc

(g) u/U_{av}, 7%fc (h) $u'v'/U_{av}^2$, 7%fc

Figure 73. Mean streamwise component and u'v' Reynolds stress with flow addition for the fanned ramp configuration. (U_{av}/u_∞=3.64)

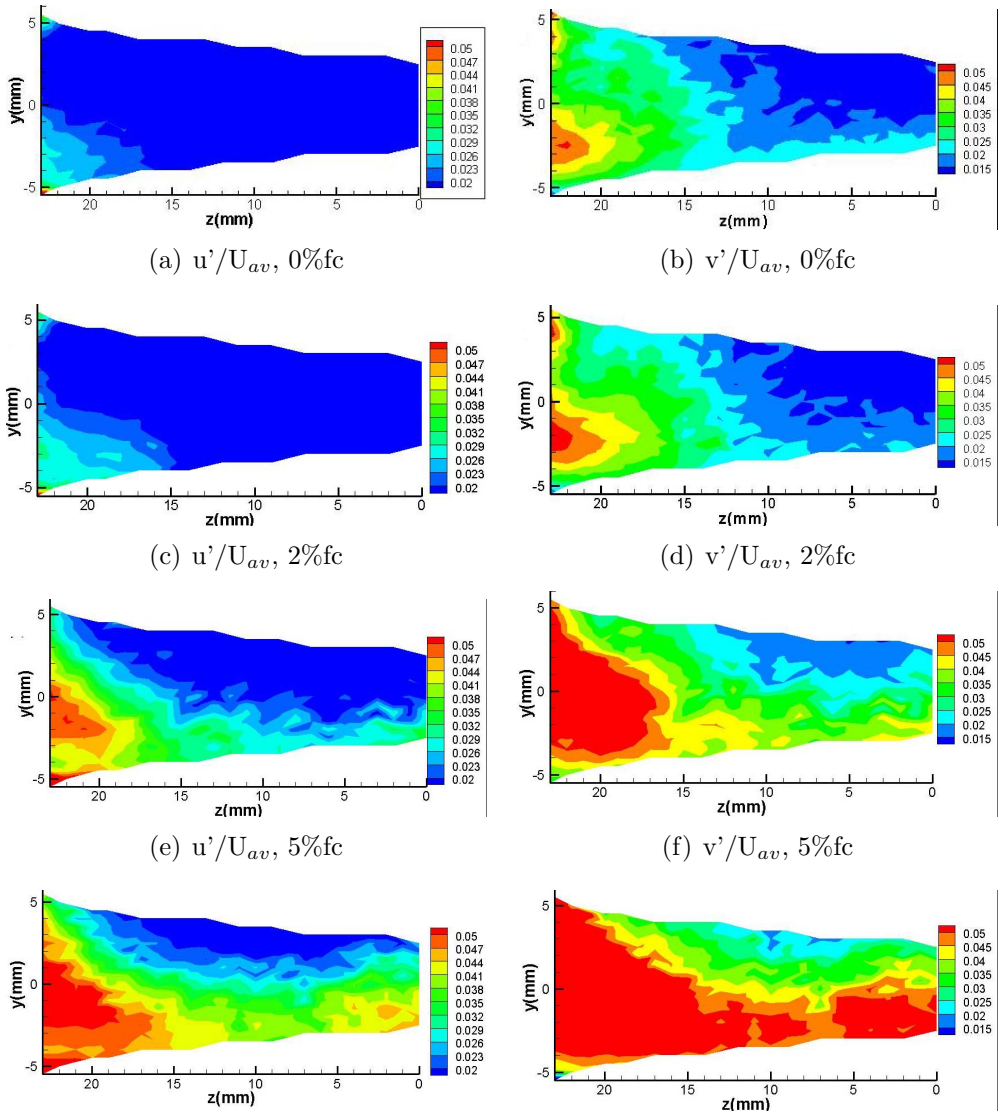

(a) u'/U_{av}, 0%fc (b) v'/U_{av}, 0%fc

(c) u'/U_{av}, 2%fc (d) v'/U_{av}, 2%fc

(e) u'/U_{av}, 5%fc (f) v'/U_{av}, 5%fc

(g) u'/U_{av}, 7%fc (h) v'/U_{av}, 7%fc

Figure 74. Turbulent kinetic energy components u' and v' with flow control addition for the fanned ramp configuration. (U_{av}/u_{∞}=3.64)

the Figure 74(e) has approximately the same fluctuating content as the 7% mass addition step configurations, given in Figure 68 and Figure 70. With seven percent addition, shown in Figures 74(g), u' is more widely increased than for the other three geometries. The v'-component profile is at or above the maximum of the fluctuations seen among the four inlet configurations. The increased energy in the v'-component might also be interpreted as evidence of too much mass flow addition.

5.2.7 Vorticity Effects Due to Flow Control on the Different Configurations. The effects of the flow control on the vorticity with 7% flow control addition are shown in Figure 75. The minimum region of the vorticity altered from the 7% mass flow addition for all cases. The negative vorticity region's area reduced in all instances compared to those shown in Figure 66. The upper region traveled further into the core of the inlet instead of remaining in the z=23 mm to 20 mm in the fanned ramp configuration. The addition of the flow control added vorticity into the core region of the duct, a positive component appeared in addition to the wall spillage. No discrete vortex existed in the submerged inlet. The plots indicate the presence of vorticity in the side wall boundary layer.

5.2.8 Quantification of Flow Control Results. One way to quantitatively compare the results of all four geometries is through a spatial standard deviation of the components. The normalized standard deviation alleviated the small differences in the mean velocities experienced due to run conditions. For each condition a total of 360 points computed the standard deviation. All spatial data corresponded to the same locations within the inlet throat. This data is summarized in Table 10. The standard deviation of the spatial variation is given in Equation 10. The term U_{sd}/U_{av} is the normalized standard deviation, with u_n/U_{av} being the normalized velocity at each measurement location. Lower values of U_{sd}/U_{av} equate to better uniformity of the throat velocity profile.

$$\frac{U_{sd}}{U_{av}} = \frac{1}{360}\sum_{i=1}^{360}\left(\frac{u_n}{U_{av}} - 1\right)^2 \tag{10}$$

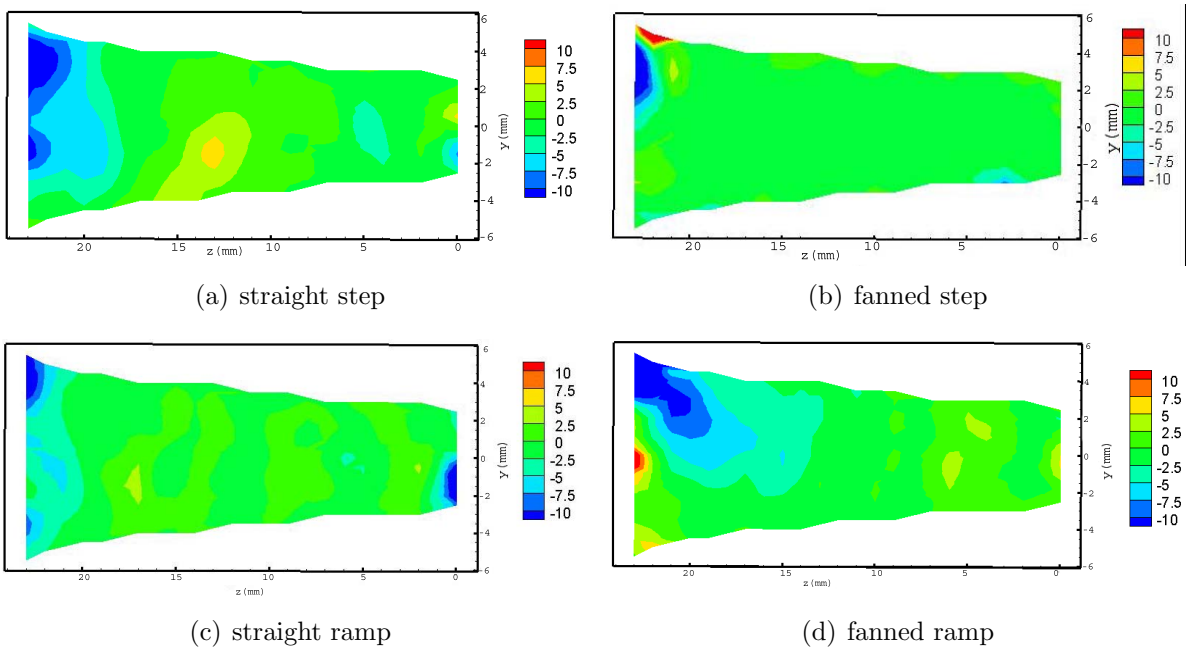

(a) straight step

(b) fanned step

(c) straight ramp

(d) fanned ramp

Figure 75. Vorticity for the 7% flow control cases for the four flow control configurations. (U_{av}/u_{∞}=3.58 for the straight step configuration, 3.70 for the fanned step, 3.76 for the straight ramp and 3.64 for the fanned ramp.)

Table 10 represents the spatial variation of the streamwise velocity shown in Figures 79 with flow control addition and configuration. The average streamwise velocity and the inlet to freestream velocity ratio are also included. The higher flow control cases have the most uniform profile with the smallest standard deviation in all cases except the fanned ramp. The minimum occurs at 5% instead of 7% mass flow addition. This demonstrates the increase in velocity along the ramp from the flow control decreased the submerged inlet's uniformity. The lowest overall standard deviation occurred for the straight ramp at the 7% case. Where the minimum occurred with the amount of flow control matters more than the smallest standard deviation.The smallest standard deviation is not the controlling factor, the location of the minimum and the flow control to achieve it matter more. With this consideration, the fanned ramp at 5% flow control addition obtained the overall best results. The next best configurations are the straight ramp at 7% flow control addition and the 7% case for the fanned step configuration.

Table 10. Summary of the submerged flow control effectiveness by examination of the spatial variation of the streamwise velocity for each flow control configuration with the average and inlet to freestream velocity ratios provided.

Model	Flow control(%)	U_{av} (m/s)	U_{sd}/U_{av}	U_{av}/u_{∞}
Fanned Ramp	0	48.78	0.0281	3.64
(Fig. 73	2	48.76	0.0270	3.64
74)	5	48.75	0.0186	3.64
	7	48.75	0.0235	3.64
Straight Ramp	0	50.47	0.0287	3.76
(Fig. 71	2	50.48	0.2078	3.76
72)	5	50.38	0.0241	3.76
	7	50.50	0.0166	3.76
Fanned Step	0	49.63	0.0273	3.70
(Fig. 69	2	49.57	0.0266	3.70
70)	7	49.22	0.0199	3.67
Straight Step	0	47.96	0.0285	3.58
(Fig. 62, 63	2	47.96	0.0265	3.58
64,67,68)	7	47.86	0.0242	3.57

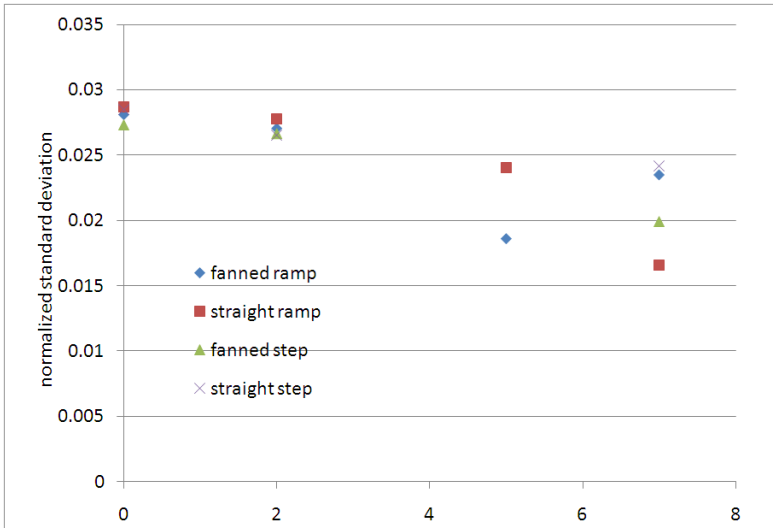

Figure 76. Normalized spatial standard deviation of the streamwise velocity for each flow control design with increasing mass flow addition.

The most direct indication of the inlet uniformity comes from the spatial variation of the streamwise velocity. The normalized spatial deviations for the streamwise velocity are given for each configuration and mass flow control setting in Figure 76. Some differences exist in each case, making the evaluation of the performance clearer in graphical presentation than from Table 10. The best configuration becomes more evident in Figure 76. The best configuration tested was the fanned ramp configuration at five percent mass addition. By increasing the mass flow addition to 7%, the uniformity decreased demonstrating nonlinearity. The less severe decrease in the normalized standard deviation, U_{sd}/U_{av}, suggests that the flow control method and location were not ideal in the two step configurations. The step configuration was less effective in altering the u-component uniformity compared to the two ramp configurations. The ramp configurations performed better since the flow experienced a less gradual shift towards a uniform streamwise profile with increased mass flow addition. Addressing the corner losses and moving the flow control jets closer to the throat were beneficial to decreasing the spatial variation of the u-component magnitudes.

The spatial deviation of the u' fluctuations in Figure 77 show generally increasing turbulence levels with flow control. These statistics hold with the behavior seen within the grids for each of the configurations. The variation is dependent on the scatter of the data since the overall level is smoothed or increased uniformly rather than growth in a particular region. A flat behavior manifested in u' with increased mass flow addition for the step configuration, as shown in Figure 77. Data for all four configurations remain unchanged with the addition of 2% flow control. The magnitude of u'_{sd}/U_{av} increased in the step configuration and straight ramp configuration at 7%. The fanned ramp increase in energy occurred with 5% mass addition. The step location limited the streamwise velocities fluctuations before reaching the throat. The distance to the inlet throat plays a role in the behavior and the energy content from the flow control jets.

The v'-component spatial variation increased with mass flow addition, as shown in Figure 78. The overall level of v'_{sd}/U_{av} was larger than the levels of u'_{sd}/U_{av}, as

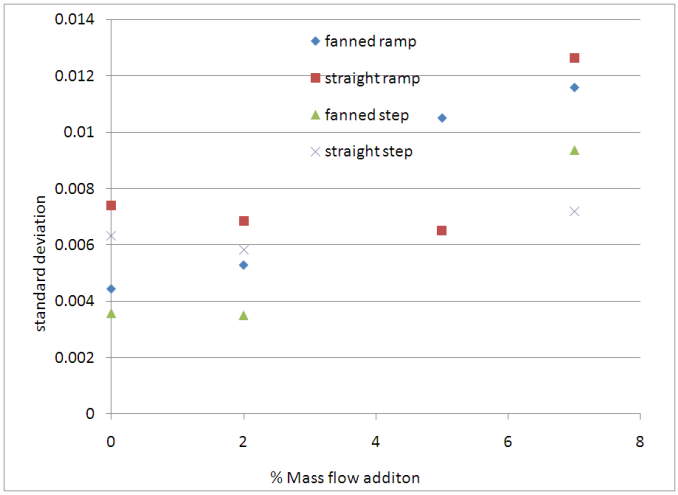

Figure 77. Spatial standard deviation of u'/U_{av} component for each flow control design with increasing mass flow addition.

reflected by the scale of Figure 78 compared to Figure 77. The energy content in the v'-component showed no increase with 7% flow control addition agreeing with the behavior seen in the grids. At 7% mass addition, the ramp configurations had considerably higher fluctuations than their step counterparts. The angled configurations had higher fluctuations than the straight configurations. The combination of the v'-component with the u'-component exhibits the trends of more turbulence with more imparted flow control.

The u'v'-component of the Reynolds stresses proved a good indicator of the flow control's presence in the grids. The spatial variation of the u'v'-component is shown in Figure 79. The addition of energy displayed an increasing trend in the turbulent energy in the u'v'-component of the Reynolds stresses as expected from the u' and v'-components. The behavior was pronounced and clear with the shear stresses, more so than the u' and v'-components of the turbulent kinetic energy. The ramp configuration has a larger value for u'v'$_{sd}$/U_{av} than the step configurations, 0.0004 compared to 0.0002. The magnitude of the u'v'$_{sd}$/U_{av} value for the straight ramp increased slowly until a large increase in the turbulence occurred at seven percent. The linear behavior or jumps in sudden turbulence levels correspond to the effectiveness of the flow control method indicated by mixing. Figure 79 appears as a good indicator of the turbulence.

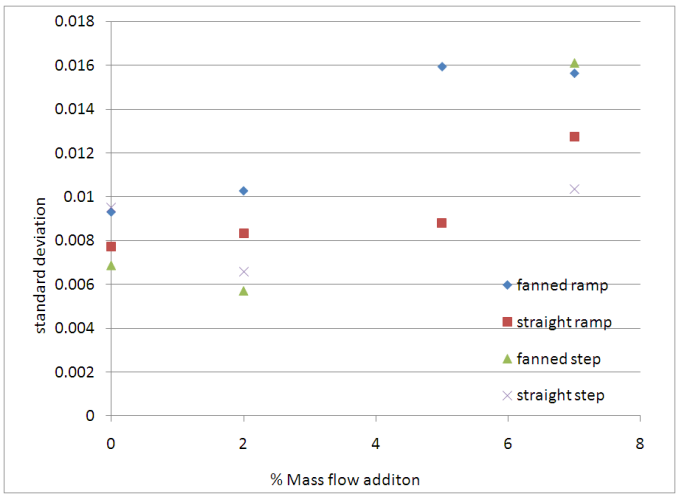

Figure 78. Standard deviation of v'/U_{av} component for each flow control design with increasing mass flow addition

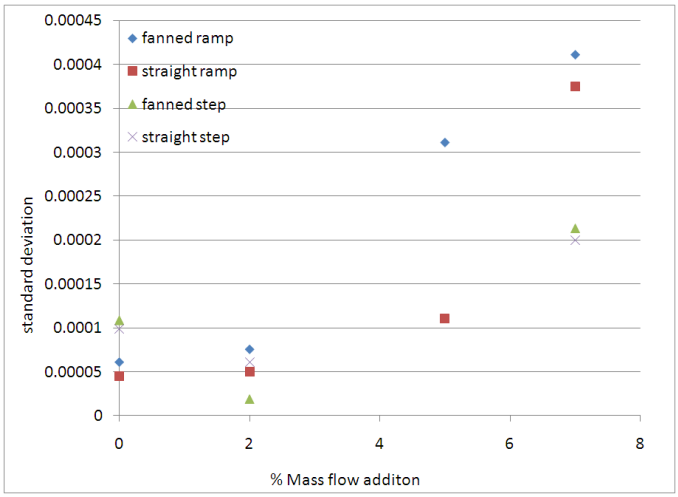

Figure 79. Standard deviation of u'v'/u^2_{av} shear stress component for each flow control design with increasing mass flow addition.

The spatial deviation of the streamwise velocity is still the best indicator of the effectiveness of the flow control method. Uniformity of the velocity interface was the focus. The u'v' standard deviation component supports the indication of the best flow control configuration, but does not define the best control method. The turbulence increases with increasing flow control. More energy means more variation. The u' and v' variation are interesting, but not necessarily the determining factor in the design.

The fluctuating components helped identify the differences in flow control. The u-component of the velocity and u'v'-component of the turbulence sufficed to observe the mixing and uniformity of the flow. The changes to the turbulence persist longer than the velocity making it more sensitive to the mass flow addition.[14] The main result of this examination is that the usage of the jets had an impact upon the inlet uniformity. The effects show in all of the measurements of the u-components as well as the v-component (linear traverses). The w-component experienced some alteration from the flow control in the fanned configurations in particular (grids). The difficulty in obtaining the w-component accurately prevented its use in quantifying the flow control performance. The u'v'-component of the turbulence particularly aided in observing the jets affect on the flow behavior location. In general, large magnitudes for u'v' indicated regions of energetic mixing. The results given by the u'v'-component show the 2% flow control cases ineffective in reaching the inlet throat. The uniformity of the u-component of the velocity improved with flow control. The standard deviation based upon the spatial data for the u-component of the velocity proved effective.

VI. Summary and Conclusions

6.1 Summary

Overall, this study of serpentine ducts and a submerged inlet encompassed several objectives. Determining the effectiveness of different pneumatic flow control methods applied to the submerged inlet geometry was the primary goal of the investigation. Laser Doppler velocimetry resulted in the velocity and turbulence profile to clarify the effect of the flow control. The process of vetting the measurement technique led to interesting results on a fundamental level. In addition to the primary goal, best characterized as applied research, the work improved general understanding of secondary flows in geometries with wall curvature.

Serpentine ducts of two different aspect ratios, each comprised of two opposing ninety degree bends, were examined by three-component LDV characterizing strong secondary fluid motion. Literature predicted strong vortical flows for the two bends system.[16],[17] The LDV system was able to capture the secondary flow along with the streamwise component. The serpentine ducts served as a platform to confirm the velocity measurement system and determine the accuracy of the components. The spanwise (w) component was found to be less accurate than the streamwise (u) and vertical (v) components but could provide information on the general trend of the secondary motions.[98],[93] Numerical simulations of the serpentine nozzles were performed and compared to the experimental results. Computational fluid dynamics results were developed and collected using Fluent v.6.2.16 in combination with a third order Reynolds stress model and a 4 million node mesh. The horizontal nozzle, in particular, matched well with the RSM results in all components examined, and the mean velocities matched well for the vertical nozzle.

A clean seeding technique combining steam and liquid nitrogen, implemented for the submerged inlet, provided the particle visibility required. Clean seeding prevented the restriction of beam access occasionally experienced in the serpentine ducts. The particle density could be readily adjusted to accommodate higher acquisition rates. No residue buildup formed in the test section, maintaining clear optical access.

Mild secondary flow patterns were captured, and the level of the streamwise flow uniformity was assessed in the submerged inlet. The curvature of the submerged inlet was less severe than the serpentine ducts, forming a less pronounced secondary flow. Literature predicted that a roll-up vortex close to each side wall could produce significant secondary flow effects like those observed in the serpentine nozzles. The free stream airspeed was lower than that of the inlet to represent takeoff conditions. Gradients in the streamwise and vertical components measured at the throat by the LDV system are mainly attributable to the effects of the boundary layer on the ramp. The expected vortical motion predicted in literature was not present. The flow progressed downward along each sidewall instead, likely due to the large velocity ratio.

The flow control was implemented at two locations on the ramp with jet orientation parallel to the freestream and with secondary flow imparted on the discrete jets. A total of four flow control geometries were examined. Assessment of the flow control on the submerged inlet determined its effectiveness for improving the inlet performance. Characterization of the velocity pattern at the throat by the LDV was used to determine the effectiveness of the flow control using discrete holes in the four different geometries. The flow control targeted the boundary layer deficit created by the ramp for elimination. The LDV data, particularly the streamwise velocity u, and the u'v' component of the Reynolds stress, displayed the effects for each flow control setting, ranging from zero to seven percent addition, and each of the four configurations. The uniformity of the streamwise component of the velocity, u, became more homogeneous with the addition of flow control to the inlet. The flow control attenuated the downward flow along the sidewalls.

6.2 Conclusions

The lessons from this work can be generalized into four main themes. The first pertains to the serpentine duct behavior. The rest are based on the submerged inlet regarding the general characteristics of the flow in the inlet, the effect of the

discrete jets used for flow control, and the method of evaluation for the flow control configurations.

The study of the two s-shaped serpentine ducts with a rectangular cross-section demonstrated the importance of aspect ratio on the flow behavior, as observed by the three-component LDV system. A single pair of streamwise vortices was present at the exit of one configuration, the horizontal duct with an aspect ratio of 1:2. The direction of the vortices were opposite to those resulting from a single 90° bend.[16] In the second configuration, the vertical duct with an aspect ratio of 2:1, weaker streamwise vortical structures were evident, despite the same cross-sectional area, mass flow rate and Dean number. The LDV data closely matched the computational predictions performed as part of this investigation. The Reynolds stress computational model was well suited to capture the anisotropic flow created within the duct under the conditions studied. The CFD results indicated that the exit flow behavior was controlled by the high flow curvature of the first bend more than the second bend.

Measurements in the submerged inlet, obtained using the novel clean seeding approach with the LDV, demonstrated consistency with the literature in that higher velocities were measured near the lip compared to the inlet ramp. The inlet to free stream velocity ratio of 3.6, used in this study, prevented the formation of the spillage vortices. The higher velocity ratios resulted in a downward flow as shown in the sign of the streamwise vorticity along the sidewall.

The LDV measurements demonstrated that the discrete flow control jets could be implemented in place of a slot without compromising the flow quality or flow control effectiveness. When placed at the inception of the ramp, the discrete flow control jets eliminated the boundary layer velocity deficit with 7% mass addition. The discrete jets were as effective as the slot at the same location with a similar mass addition of 7.5% for the slot.[25] Uniformity was achieved through attenuating the velocity gradient from the lip to inlet ramp. A straightforward analysis based on simple jet theory proved useful to predicting this outcome.

Measurements of the spatial distribution of the streamwise component of the velocity demonstrated the effectiveness of flow control from the discrete jets for the four flow control configurations. The mass flow addition required for uniformity fell from 7% to 5%, when the jets were placed in the ramp closer to the throat, according to this data. Targeting the largest velocity deficit region at the ramp-sidewall juncture typically improved the flow control performance. The analysis of the Reynolds normal stress and shear stresses proved insightful in elucidating the effect of the mass flow additions.

6.3 Recommendations

Based upon the results of this investigation, moving the flow control jets closer to the throat provides a method to decrease the amount of flow control necessary. Jet mixing theory is one method for approximating the development and understanding the amount of mixing occurring in the progression of inlet uniformity. The spreading angle of the jets based on previous examinations by Jacobsen[90] and Goss[91] worked, however, other angles are possible. Correlations with numerical simulation would permit an optimization process. Lower inlet to freestream velocity ratios provided a means of determining the angled mass additions' affect on the preexisting secondary flow. Lower velocity ratios potentially react differently than the inlet flow examined.

The computational grid for the submerged inlet would have been more complicated, due to modeling a large region of incoming flow around the inlet and the inclusion of mass addition. The CFD results of the serpentine ducts demonstrate that moderate fidelity of the submerged inlet is possible, assuming sufficient server capabilities are available. Only the flow without the addition of boundary layer control could be created with any ease. Transonic flight examination is the next step in permitting greater applicability for the submerged inlet in aircraft. In a concurrent study, large improvements in inlet uniformity with blowing at transonic speeds was obtained. Design optimization regarding jet location, orientation and implementation can be improved to the theoretical recovery limit and utilized for other curved flows.

Bibliography

[1]Mossman, E. A. and Randall, L. M., "An Experimental Investigation of the Design Variables for a NACA Submerged Duct Entrances," No. A7I30, National Advisory Committee for Aeronautics(NACA), Ames Aeronautical Laboratory, Moffett Field, California, January 1948.

[2]A.H. Sacks, J., "Theoretical Investigation of Submerged Inlets at Low Speeds," August 1951, Technical note 2323.

[3]Taylor, R., "Some Effects of the Side-Wall Modification on the Drag and Pressure Recovery of an NACA Submerged Inlet at Transonic Speeds," February 1952.

[4]J.D. Mattingly, W.H. Heiser, D. P., *Aircraft Engine Design, 2nd Edition*, American Institute of Aeronuatics and Astronautics Inc., 2002.

[5]D.G. Wilson, T. K., *The Design of High-Efficiency Turbomachinery and Gas Turbines, 2nd Edition*, Prentice Hall, 1998.

[6]Sobester, A., "Tradeoffs in Jet Inlet Design: A Historical Perspective," *Journal of Aircraft*, Vol. 44, No. 3, May-June 2007.

[7]"Gas Turbine Engine Inlet Flow Distortion Guidelines," Tech. rep., 2002, Revision B, (ARP 1420).

[8]"Inlet Total-Pressure-Distortion Considerations for Gas Turbine Engines," Tech. rep., 1999, Revision A, (AIR 1419).

[9]Williams T. Cousins, P., "History, Philosophy, Physics, and Future Directions of Aircraft Propulsion System/Inlet Integration," No. GT2004-54210, ASME Turbo Expo, Vienna Austria, June 2004.

[10]B.R. Munson, D.F. Young, T. O., *Fundementals of Fluid Mechanics, 3rd Edition*, John Wiley and Sons, Inc., 1998.

[11]Prandtl, L., *Essentials of Fluid Dynamics*, Hafner Publishing Company, New York, 1952.

[12]Schlichting, H. and Gersten, K., *Boundary Layer Theory*, Springer, eighth ed., 2001.

[13]Panton, R. L., *Incompressible Flow, 2nd Edition*, John Wiley and Sons, Inc., 1996.

[14]Wilcox, D. C., *Turbulence Modeling for CFD*, DCW Industries, 2nd ed., 1998.

[15]Sovran, G., editor, *The Applicability of Secondary Flow Analyses to the Solution of Internal Flow Problems(General Motors Research Laboratories; Warren, MI, 1965)*, New York, 1967, Elsevier Publishing Company.

[16]S.A. Berger, L. T. and Yao, L.-S., "Flow in Curved Pipes," *Fluid Mechanics*, 1983, pp. 461–512.

[17]Angie Rabe, W. N. and Burdisso, R., "Effectiveness of a Serpentine Inlet Duct Flow Control Technique at Design and Off-Design Simulated Flight Conditions," No. GT2004-53475, ASME Turbo Expo, Vienna Austria, June 2004.

[18]M.J. Zucrow, J. H., *Gas Dynamics, volume 1*, John Wiley and Sons, Inc., 1975.

[19]Axelson, J. A. and Taylor, R. A., "Preliminary Investigation of the Transonic Characteristics of an NACA Submerged Inlet," No. A50C13, National Advisory Committee for Aeronautics(NACA), Ames Aeronautical Laboratory, Moffett Field, California, June 1950.

[20]Rolls, L. S., "A Flight Comparison of a Submerged Inlet and a Scoop Inlet at Transonic Speeds," , No. A53A06, March 1953.

[21]Garrison, P., "The Scoop on the NACA Scoop," *Flying Magazine*, September 2004.

[22]R. Holman, Q. Gallas, B. C. L. C., "Interaction of Adjacent Synthetic Jets in an Airfoil Separation Control Application," No. AIAA 2003-3709, Orlando, Florida, June 2003.

[23]M. Kamishita, S. Aso, K. K. K. S., "Active Control of Aerodynamic Characteristics of Next-Generation SST Wing by Lateral Blowing," *AIAA*, , No. AIAA 2000-0516, January 2000.

[24]M.D. Zeiger, J. Gerlach, S. M. D. T., "Control of Separated Flow Over a Swept, Sharp-Edged Wing," *AIAA*, , No. AIAA 2002-0414, January 2002.

[25]Scribben, A. and Goettke, M., "Reactive Conformal Inlet Tecnology Enhancement(RECITE)," Tech. Rep. AFRL-RB-WP-TR-2008-3134, Integration and Demostration Branch, Aeronautical Science Division, July 2008.

[26]Martin, N. J. and Holzhauser, C. A., "An Experimental Investigation at Large Scale of Several Configurations of an NACA Submerged Air Intake," No. A8F21, National Advisory Committee for Aeronautics(NACA), Ames Aeronautical Laboratory, Moffett Field, California, October 1948.

[27]W.G. Vincenti, C. K. J., *Introduction to Physical Gas Dynamics*, Krieger Publishing Company, 2002.

[28]Jr., J. A., *Hypersonic and High Temperature Gas Dynamics*, American Institute of Aeronautics and Astronautics, Inc., 1989.

[29]W. Peifen, D. J., "Numerical Analysis of Three-Dimensional Flows Inside/Outside a Submerged Air Inlet Under Maneuver," No. AIAA 2003-4138, Orlando, Florida, June 2003.

[30]E.S. Taskinoglu, D. K., "Multi-Objective Shape Optimization Study for a Subsonic Submerged Inlet," *Journal of Propulsion and Power*, Vol. 20, No. 4, July-August 2004.

[31]E.S. Taskinoglu, D. K., "Numerical Analysis of Submerged Inlets," No. AIAA 2002-3147, St. Louis, Missouri, June 2002.

[32]E.S. Taskinoglu, D. K., "Design Optimization for Submerged Inlets- Part I," No. AIAA 2003-1247, Reno, Nevada, January 2003.

[33]V.J. Jovanovic, E.S. Taskinoglu, D. K., "Experimental Investigation of a Submerged Subsonic Inlet," *Journal of Propulsion and Power*, Vol. 22, No. 1, January-February 2006.

[34]S. Sun, R.-W. G. and Wu, Y.-Z., "Characterization and performance Enhancement of Submerged Inlet with Flush-Mounted Planar Side Entrance," *Journal of Aircraft*, September-October 2007, DOI: 10.2514/1.26432.

[35]R.J. Divine, J.K. Watterson, R. C. J. R., "An Investigation into Improving the Performance of Low Speed Auxiliary Air Inlets Using Vortex Generators," No. AIAA 2002-3264, St. Louis, Missouri, June 2002.

[36]Throndson, L., "Combat Survivability with Advanced Aircraft Propulsion and Development," *Journal of Propulsion and Power*, Vol. 19, No. 11, November 1982, pp. 915–920, AIAA 81-1506R.

[37]V.J. Jovanovic, E.S. Taskinoglu, D. K. G. E., "Experimental Investigation of a Submerged Subsonic Inlet-Part II," No. 2004-4842, Providence, Rhode Island, August 2004.

[38]Blazek, J., *Computational Fluid Dynamics: Principles and Applications*, Elservier Science Ltd., 2001.

[39]Mathieu, J. and Scott, J., *An Introduction to Turbulent Flow*, Cambridge University Press, 2000.

[40]Freitas, C., "Perspective: Selected Benchmarks From Commercial CFD Codes," *Journal of Fluids Engineering*, Vol. 117, June 1995, pp. 209–218.

[41]Iaccarino, G., "Predictions of a Turbulent Separated Flow Using Commercial CFD Codes," *Journal of Fluids Engineering*, Vol. 123, December 2001, pp. 819–828.

[42]K.C. Schadow, K.J. Wilson, M. L. and Gutmark, E., "Enhancement of Mixing in Reacting Fuel-Rich Plumes Issued from Elliptical Nozzles," *Journal of Propulsion and Power*, Vol. 3, No. 2, March-April 1987.

[43]V. J. Jovanovic, E. S. Taskinoglu, D. D. K., "Experimental Investigation of a Submerged Subsonic Inlet," No. 2004-2649, AIAA, Portland, Oregon, July 2004.

[44]Tsay, W. and Chen, C., "Numerical Simulation of the Submerged Inlet," , No. AIAA 90-2137, July 1990, AIAA/SAE/ASME/ASEE, 26th Joint Propulsion Conference.

[45]Abbot, J. and Slater, J., "Computational Study of the Aerodynamic Performance of Three-Dimensional Subsonic Inlets," July 2001, 37th AIAA/ASME/SAE/ASEE Joint Propulsion Conference and Exhibit.

[46]J.G. Lee, S.Y. Jung, C. A., "Numerical Simulation of Three-Dimensional Flows for Flush Inlet," No. AIAA 2004-5190, Providence, Rhode Island, August 2004.

[47]Berrier, B. and Allan, B., "Experimental and Computational Evaluation of Flush Mounted S-Duct Inlets," January 2004, AIAA 2004-764-627, 42nd AIAA Aerospace Sciences Meeting and Exhibit.

[48]Anderson, B. and Keller, D., "Robust Design Methodology For Optimal Micro-Scale Secondary Flow Control in Compact Diffusers," , No. AIAA 2002 541-192, 2002.

[49]V.J. Jovanovic, E.S. Taskinoglu, D. K. G. E., "Experimental Investigation of a Submerged Subsonic Inlet," No. 2004-2649, Portland, Oregon, June-July 2004.

[50]M. Shur, M. Strelets, A. T. P. S., "Turbulence Modeling in Rotating and Curved Channels: Assessment of the Spalart-Shur Correction Term," *AIAA*, , No. AIAA 98-0325, 1998.

[51]Piomelli, U., "Large-eddy Simulation - Present State Future Perspectives," , No. AIAA 1998-534, January 1998.

[52]S. Heinzen, C. Hall, N. C., "Inflight Application of Active Separation Control Using Control of Pulsed Jet Blowing," *AIAA*, , No. AIAA 2002-0416, January 2002.

[53]R. Florea, M. Haas, L. H. C. L. and Stucky, M., "Optimization of Bleed Flow Control for Agressive Serpentine Duct," , No. AIAA 2005-1205, January 2005, 43rd AIAA Aerospace Sciences Meeting and Exhibit.

[54]Y. Utturkar, R. Holman, R. M. B. C. M. S. L. C., "A Jet Formation Criterion for Synthetic Jet Actuators," No. AIAA 2003-0636, Reno, Nevada, January 2003.

[55]M. Gordon, J.E. Cater, J. S., *Physics of Fluids*, Vol. 16, No. 3, March 2004.

[56]J. Kim, K. K. and Sung, H., "Wall Pressure Fluctuations in a Turbulent Boundary Layer After Blowing or Suction," *AIAA Journal*, Vol. 41, No. 9, September 2003.

[57]Quinn, W. R., "Development of a Large-Aspect-Ratio Rectangular Turbulent Free Jet," *AIAA Journal*, Vol. 32, No. 3, March 1994, pp. 547.

[58]K. C. Cheng, R.-C. L. and Ou, J.-W., "Fully Developed Laminar Flow in Curved Rectangular Channels," *Journal of Fluids Engineering*, March 1976, pp. 41–48.

[59]Whitelaw, J. and Yu, S., "Velocity Measurements in an S-shaped Diffusing Duct," *Experiments in Fluids*, Vol. 15, 1993, pp. 364–367.

[60]Cavicchi, R. H., "A Three-Dimensional CFD Investigation of Secondary Flow in an Accelerating, 90 Degree Elbow," *NASA/TM*, , No. 2001-211219, 2001.

[61]T.Reynolds, M.F. Reeder, E. S. R. M. and Crafton, J., "Parametric Study of Jets Emanating from Serpentine Nozzles of Varied Cross-Section," January 2006, AIAA 2006-1280.

[62]S. Jakirlic, K. H. and Tropea, C., "Modeling Rotating and Swirling Turbulent Flows: A Perpetual Challenge," *AIAA*, Vol. 40, No. 10, October 2002, pp. 1984–1996.

[63]B. Song, R.S. Amano, G. R. L., "On Computations of Complex Turbulent Flow By Using Nonlinear k-ω Model," *Numerical Heat Transfer, Part B*, Vol. 39, 2001, pp. 421–434.

[64]B. Song, R. A., "Application of a Non-Linear k-ω Model to a Turbulent Flow Inside Sharp U-Bend," *Computational Mechanics*, Vol. 26, 2000, pp. 344–351.

[65]P.R. Spalart, M. S., "On the Sensitization of Turbulence Models to Rotation and Curvature," *Aerospace Science and Technology*, , No. 5, 1997, pp. 297–302.

[66]G. Gauthier, P.Gondret, H. T. and Rabaud, M., "Centrifugal Instabilities in a Curved Rectangular Duct of Small Aspect Ratio," *Physics of Fluids*, Vol. 13, No. 10, October 2001.

[67]Boswell, B. and Dutton, J., "Velocity Measurements in a Pressure-Driven Three-Dimensional Compressible Turbulent Boundary Layer," *AIAA Journal*, Vol. 40, No. 7, July 2002.

[68]T. Kouchi, T. M. and Masuya, G., "Numerical Simulations in Scramjet Combustion with Boundary-Layer Bleeding," *Journal of Propulsion and Power*, Vol. 21, No. 4, July-August 2005.

[69]Sovran, G., editor, *Aspects of Internal Flow (General Motors Research Laboratories; Warren, MI, 1965)*, New York, 1967, Elsevier Publishing Company.

[70]P. Petitjeans, J.-E. W., "Spatial Evolution of Gortler Instability in a Curved Duct of High Curvature," *AIAA Journal*, Vol. 34, No. 9, September 1996, AIAA-13309-205.

[71]L.F. Souza, M. M., "Gortler Vortices Control with Localized Suction and Blowing," *31st AIAA Fluid Dynamics Conference and Exhibit*, , No. AIAA-2001-2992 (A01-31320), June 2001.

[72]A. Ajakh, M. Kestoras, H. P., "Growth of Forced Perturbations in Gortler Instability," , No. AIAA-97-1778, (AIAA-1997-1778-872), 1997.

[73]Michael J. Brear, Zachary Warfield, J. F. M. C. S. B. J. D. P. and Philhower, J. S., "Engine Inlet of an Uninhabited Combat Air Vehicle(UCAV)," *Jounal of Fluid Engineering*, Vol. 126, March 2004, pp. 266.

[74]Steven R. Wellborn, B. A. R. and Okiishi, T. H., "Study of the Compressible Flow in a Diffusing S-Duct," *Journal of Propulsion and Power*, Vol. 10, No. 5, September-October 1994.

[75]White, F. M., *Viscous Fluid Flow, 2nd Edition*, McGraw-Hill, 1991.

[76]B.H. Anderson, D.R. Reddy, K. K., "Study on Computing Separating Flows Within a Diffusing Inlet S-Duct," *Journal of Propulsion and Power*, Vol. 10, No. 5, September-October 1994.

[77]Ghanshyam Singh, T. S. and Bhaskaran, K. A., "Mixing and Entrainment Characteristics of Circular and Noncircular Confined Jets," Vol. 125, September 2003, pp. 835–842.

[78]E. Ferdman, M. V. O. and Kim, S., "Effect of Initial Velocity Profile on the Development of Round Jets," *Journal of Propulsion and Power*, Vol. 16, No. 4, July-August 2000, pp. 676–686.

[79]C.-M. Ho, E. G., "Vortex Induction and Mass Entrainment in a Small-Aspect-Ratio Elliptic Jet," *Journal of Fluid Mechanics*, Vol. 179, 1987, pp. 383–405.

[80]Quinn, W. R., "Near-Field Measurements in an Equilateral Triangular Turbulent Freejet," *AIAA Journal*, Vol. 43, No. 12, December 2005, pp. 2574–2585.

[81]S. Tomiaka, L. J. and Schetz, J., "Sonic Injector from Diamond-Shaped Orifices into Supersonic Crossflow," *Journal of Propulsion and Power*, Vol. 19, No. 1, January-February 2003.

[82]L.J.S. Bradbury, A. K., "The Distortion of Jets by Tabs," *Journal of Fluid Mechanics*, Vol. 70, 1975, pp. 801.

[83]K.B.M.Q. Zaman, M. R. and Samimy, M., "Control of an Axisymmetric Jet Using Vortex Generators," *Phys. Fluids*, Vol. 6, No. 2, February 1994.

[84]D.D. Glawe, M. Samimy, A. N. and Chen, T., "Effects of Nozzle Geometry on Parallel Injection into a Supersonic Flow," *Journal of Propulsion and Power*, Vol. 12, No. 6, November-December 1996.

[85]Peterson, S. D. and Plesniak, M., "Evolution of Jets Emanating from Short Holes into Crossflow," *Journal of Fluid Mechanics*, Vol. 503, 2004, pp. 57–91.

[86]Goldstein, R. and Stone, L., "Row-of-Holes Film Cooling of Curved Walls at Low Injection Angles," *Journal of Turbomachinery*, Vol. 119, No. 3, 1997, pp. 574–579.

[87]C.S. Yang, C. L. and Gau, C., "Film Cooling Performance and Heat Transfer Over an Inclined Film-Cooled Surface at Different Convergent Angles with Respect to Highly Turbulent Mainstream," *Applied Thermal Engineering*, Vol. 29, February 2008.

[88]Margason, R., "Fifty Years of Jet in Cross Flow Research"," Vol. CP-534, 1993.

[89]R.J. Hartfield Jr., S.D. Hollo, J. M., "Experimental Investigation of a Supersonic Swept Ramp Injector Using Laser Induced Iodine Flourescence," *Journal of Propulsion and Power*, Vol. 10, No. 1, January-February 1994.

[90]L.S. Jacobsen, J. S. and Ng, W., "Flowfield Near a Mulitiport Injector Array in a Supersonic Flow," *Journal of Propulsion and Power*, Vol. 16, No. 2, March-April 2000.

[91]L.S. Jacobsen, S.D. Gallimore, J. S. W. O. and Goss, L., "Improved Aerodynamic-Ramp Injector in Supersonic Flow," *Journal of Propulsion and Power*, Vol. 19, No. 4, July-August 2003.

[92]E. Gutmark, K. S. and Wilson, K., "Subsonic and Supersonic Combustion Using Noncircular Injectors," *Journal of Propulsion and Power*, Vol. 7, No. 2, March-April 1991.

[93]G.D. Byrne, S.W. James, R. T., "A Single-head Fibre Optic Laser Doppler Anemometer Probe for the Measurement of Flow Angles," *Measurement Sciences and Technology*, , No. 15, 2004.

[94]*Users Guide FMA 2600A-FVL-2600A Series Mass and Volume flow Controlers*.

[95]http://www.dantecdynamics.com/Default.aspx?ID=712, August 12 2008, particle information.

[96]J.C. Tannehill, D. A. and Pletcher, R., *Computational Fluid Mechanic and Heat Transfer 2nd Ed.*, Taylor and Francis, 1984.

[97]Mossman, E. A., "Summary of NACA Submerged-Inlet Investigations," National Advisory Committee for Aeronautics(NACA), Ames Aeronautical Laboratory, Moffett Field, California, 1953.

[98]*Three-Color, Five-Beam, Three Component Laser Doppler Anemometer System*, August 1986.

[99]*Six Jet Atomizer Model 9306 Instructional Manual*, September 2000, PIN 19990143 Revision H.

[100]http://engineeringtoolbox.com/particle-sizes-d_934.html, August 12 2008, search particle sizes.

[101]Y.-L. Lin, T.I.-P. Shih, K. C. D. R. A. A., "Nonlinear vs. Linear k-ω Model for Predicting Flow and Heat Transfer in a Smooth U-Duct," *AIAA*, , No. AIAA 1998-3560, July 1998.

[102]Humphrey, J. A. C. and Whitelaw, J. H., "Measurements in Curved Flows," *Turbulence in Internal Flows*, edited by S. N. B. Murthy, Hemisphere Publishing Corporation, Washington, 1976, pp. 407–437.

[103]Reeder, M. and Samimy, M., "The Evolution of a Jet with Vortex-generating Tabs: Real Time vs. Quantitative Measurements," *Journal of Fluid Mechanics*, Vol. 311, 1996.

[104]B.J. Lee, C. Kim, O.-H. R., "Optimal Shape Design of the S-Shaped Subsonic Intake Using NURBS," No. AIAA 2005-0455, Reno, Nevada, January 2005.

REPORT DOCUMENTATION PAGE

Form Approved
OMB No. 074-0188

1. REPORT DATE *(DD-MM-YYYY)*	**2. REPORT TYPE**	**3. DATES COVERED** *(From – To)*
17-12-2010	**Doctoral Dissertation**	Oct 2006-Dec 2010

4. TITLE AND SUBTITLE

Flow Control Application on a Submerged Inlet Characterized by Three-Component LDV

5a. CONTRACT NUMBER

5b. GRANT NUMBER

5c. PROGRAM ELEMENT NUMBER

6. AUTHOR(S)

Tina Reynolds

5d. PROJECT NUMBER

5e. TASK NUMBER

5f. WORK UNIT NUMBER

7. PERFORMING ORGANIZATION NAMES(S) AND ADDRESS(S)
Air Force Institute of Technology, Graduate School of Engineering and Management (AFIT/EN)
2950 Hobson way, WPAFB, 45433-7765

8. PERFORMING ORGANIZATION REPORT NUMBER

AFIT/DS/ENY10-D03

9. SPONSORING/MONITORING AGENCY NAME(S) AND ADDRESS(ES)
AFRL/RBAI
2145 5th Street, WPAFB, OH 45433

10. SPONSOR/MONITOR'S ACRONYM(S)

11. SPONSOR/MONITOR'S REPORT NUMBER(S)

12. DISTRIBUTION/AVAILABILITY STATEMENT
APPROVED FOR PUBLIC RELEASE, DISTRIBUTION UNLIMITED

13. SUPPLEMENTARY NOTES
This material is declared a work of the US Government and is not subject to the copyright protection in the United States.

14. ABSTRACT

A submerged inlet investigation, using flow control in the form of discrete blowing, examined proximity and jet directionality to improve compressor face uniformity. The flow control locations were at the head of the ramp and part way down the ramp, providing four configurations under examination. Laser Doppler velocimetry (LDV)measurements at the throat determined the effect of the flow control based on the statistical velocity measurements. Blowing at closer proximity to the throat and targeting the largest velocity deficit region provided the best results. The airspeed and inlet velocity simulated takeoff and landing conditions; velocities ranged from Mach 0.1-0.3 at the throat. Secondary components and turbulence measurements proved useful in determining the effect of the flow control configurations. In a complimentary study, two serpentine ducts of rectangular cross-section evaluated the LDV capability before the inlet examination. The s-shaped serpentine ducts had features comparable to those expected in the submerged inlet. The flow through two serpentine ducts, of identical hydraulic diameters but different aspect ratios, demonstrated different behaviors despite all other features being the same. Two strong counter-rotating streamwise vortices formed for the 2:1 aspect ratio while four weaker vortices formed in the 1:2 aspect ratio duct. Computational simulations, performed on the serpentine ducts using a Reynolds shear stress model on a 4 million cell grid, agreed with the results of the experimental examination. The agreement between the exit profiles provided confidence in the LDV system to make the inlet measurements possible.

15. SUBJECT TERMS
Flow Control injection, Submerged Inlets, Serpentine Ducts, Liquid Nitrogen Steam Clean Seeding

16. SECURITY CLASSIFICATION OF: Unclassified			**17. LIMITATION OF ABSTRACT**	**18. NUMBER OF PAGES**	**19a. NAME OF RESPONSIBLE PERSON**
REPORT	**ABSTRACT**	**c. THIS PAGE**			Dr. Mark F. Reeder
U	**U**	**U**	**UU**	180	**19b. TELEPHONE NUMBER** *(Include area code)* (937) 255-3636x4530

Standard Form 298 (Rev: 8-98)
Prescribed by ANSI Std. Z39-18